

INFORMATION TO USERS

This manuscript has been reproduced from the microfilm master. UMI films the text directly from the original or copy submitted. Thus, some thesis and dissertation copies are in typewriter face, while others may be from any type of computer printer.

The quality of this reproduction is dependent upon the quality of the copy submitted. Broken or indistinct print, colored or poor quality illustrations and photographs, print bleedthrough, substandard margins, and improper alignment can adversely affect reproduction.

In the unlikely event that the author did not send UMI a complete manuscript and there are missing pages, these will be noted. Also, if unauthorized copyright material had to be removed, a note will indicate the deletion.

Oversize materials (e.g., maps, drawings, charts) are reproduced by sectioning the original, beginning at the upper left-hand corner and continuing from left to right in equal sections with small overlaps. Each original is also photographed in one exposure and is included in reduced form at the back of the book.

Photographs included in the original manuscript have been reproduced xerographically in this copy. Higher quality 6" x 9" black and white photographic prints are available for any photographs or illustrations appearing in this copy for an additional charge. Contact UMI directly to order.

UMI

A Bell & Howell Information Company
300 North Zeeb Road, Ann Arbor MI 48106-1346 USA
313/761-4700 800/521-0600

**GAS PHASE LEVEL STRUCTURE OF C₆₀ BUCKYBALL
AND DERIVATIVES EXHIBITING BROKEN
ICOSAHEDRAL SYMMETRY**

**. GAS PHASE LEVEL STRUCTURE OF C₆₀ BUCKYBALL
AND DERIVATIVES EXHIBITING BROKEN
ICOSAHEDRAL SYMMETRY**

**A dissertation submitted in partial fulfillment
of the requirements for the degree of
Doctor of Philosophy**

By

**TYLE CURTIS REIMER, B.S., M.S.
Purdue University, 1987
University of Arkansas, 1985**

**May 1996
University of Arkansas**

UMI Number: 9700364

**UMI Microform 9700364
Copyright 1996, by UMI Company. All rights reserved.**

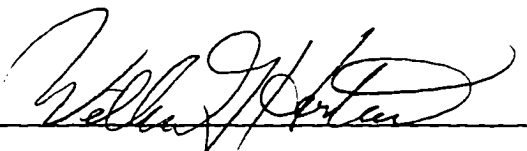
**This microform edition is protected against unauthorized
copying under Title 17, United States Code.**

UMI
300 North Zeeb Road
Ann Arbor, MI 48103

This dissertation is approved for
recommendation to the
Graduate Council

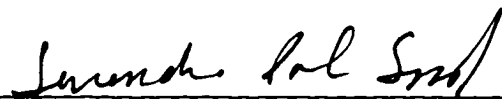
Dissertation Director:

Professor William Harter

A handwritten signature in cursive script, appearing to read "William Harter", written over a horizontal line.

Dissertation Committee:

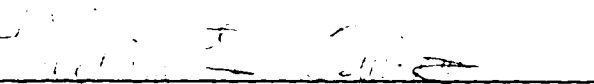
Professor Surendra Singh

A handwritten signature in cursive script, appearing to read "Surendra Singh", written over a horizontal line.

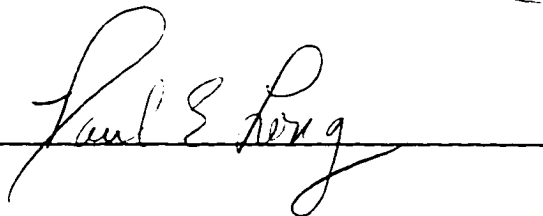
Professor Gregory Salamo

A handwritten signature in cursive script, appearing to read "Gregory Salamo", written over a horizontal line.

Professor William Oliver

A handwritten signature in cursive script, appearing to read "William Oliver", written over a horizontal line.

Professor Paul Long

A handwritten signature in cursive script, appearing to read "Paul Long", written over a horizontal line.

Acknowledgments

This work is dedicated in memory of the support, and influence provided by

ERROL C. REIMER

I would also like to thank

William Harter and David Weeks

for their guidance and freely given assistance in making this research possible.

Table of Contents

Chapter 1 Introduction

Discovery.....	1
Fullerite.....	4
Fullerene Doping	6
Doping Fullerite	8

Chapter 2 Geometric Model and Symmetry

History.....	10
Rotational Symmetry.....	11
Symmetry Analysis	13

Chapter 3 Molecular Eigenstates and Eigenvalues

Born Oppenheimer Approximation.....	18
Electronic Energy levels	20
Vibrational Eigenvalues.....	25
Rotational structure.....	26

Chapter 4 Nuclear spin weights and gas phase spectral structure of $^{12}\text{C}_{60}$ and $^{13}\text{C}_{60}$ Buckminsterfullerene

Introduction	31
Spin-Permutation Symmetry of $^{12}\text{C}_{60}$	33
Permutational Analysis	40
Spin-Permutation Symmetry of $^{13}\text{C}_{60}$	42
Superhyperfine Structure.....	47
Spontaneous Symmetry Breaking on C_5 Axis.....	49

Chapter 5 Rotation Energy Level Spectra for Half-integral Angular Momentum Icosahedral Molecules

Introduction	52
Fine Structure for Half Integral J.....	54
Symmetry Analysis of Fine and Superfine Structure	62

Chapter 6 Rotational Level Fine Structure of the buckyball isomer $^{13}\text{C}^{12}\text{C}_{59}$

XC_{59} Molecule	73
Approximating the Semi-rigid Rotational Hamiltonian	74
Rotational Energy Surface.....	75
Superfine Level Structure	82

Chapter 7 Fullerene doping on cyclic symmetry axes.....	86
Symmetry Breaking on C_5 Axis.....	88
Symmetry Breaking on C_2 Axis.....	91
Chapter 8 Conclusions.....	94
Bibliography.....	95
<i>Appendices</i>	
Appendix A $Y(d)$ Multiplication Table.....	101
Appendix B Irreducible Representations, Characters, and Correlations.....	105
Appendix C Icosahedral Cross Products.....	109
Appendix D S_{60} characters for icosahedral operators.....	110
Appendix E Y_h - S_{60} correlation frequencies.....	112

Chapter 1 Introduction

The study of matter containing the element carbon (C) has intrigued mankind since prehistoric times. From fire hardened wood to modern carbon isotope dating, this element has seen many uses. It plays a role in solar fusion and has been indirectly observed in the vast reaches of interstellar space. Life on earth depends upon this element to obtain energy and provides for its very structure. Carbon is unique in its ability to combine with numerous other elements forming literally millions of known complex compounds. Pure forms of carbon were once considered to fall in the categories of amorphous, graphite, and diamond with graphite being one of the softest solids and diamond being among the hardest. In the last decade however, new forms of carbon have joined this allotropy with their own intrinsic properties and potential applications.

Discovery

In the early 1980's, the research team of Kroto, Smalley and associates observed pronounced peaks in mass spectroscopy experiments carried out on carbon fragments obtained from laser ablated carbon rich targets. Their work was motivated to model soot formation and the chemistry of carbon stars. These fragments were predominately composed of 60 and 70 carbon aggregates.

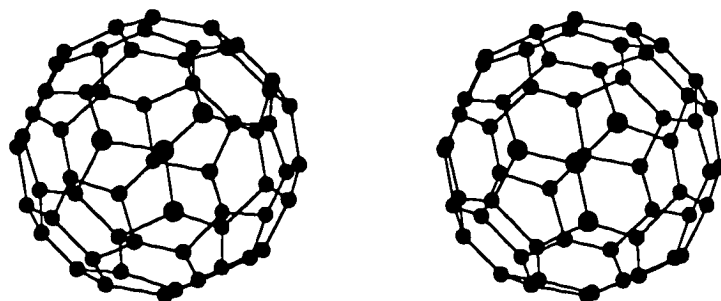


Figure 1.1 Stereoscopic view of C₆₀ Buckyball

To describe this phenomena, a molecular form of carbon composed of a hollow spheroidal arrangement of carbon was proposed.¹ These molecules were named Fullerenes in honoring Buckminster Fuller and his work with geodesic structures. The premier Fullerene to be investigated was that of C_{60} often referred to as Buckyball. The proposed structure was that of the common soccer ball with vertices of interconnected pentagons and hexagons forming the locations of the 60 carbons.

With this announcement an investigation into the feasibility and stability of such molecules ensued. The main point of contention was that with valences ranging from 2 to 4, the carbons might find other isometric arrangements more energetically favorable than the icosahedral structure above. For example, the C_{60} family of isomers also include the linear chain, a cyclic loop having D_{60} symmetry, a double loop with D_{2h} symmetry and a host of others, some having no symmetry whatsoever.

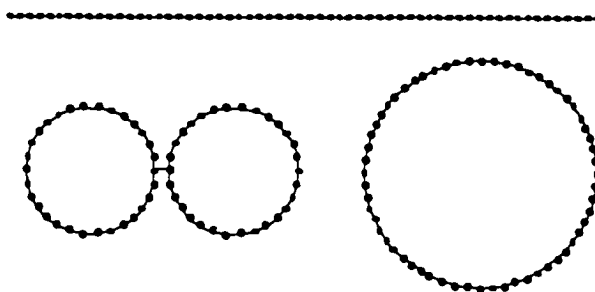


Figure 1.2 C_{60} Isomers

This often heated debate continued through 1989. In 1988 theoretical calculations for buckyball predicted only four IR active vibrational modes.^{2,3} A sparseness of structure is characteristic of high symmetry molecules such as was previously observed in vibrational spectra of octahedral SF_6 .⁴ A four peak spectrum (Figure 1.3) was first seen

in 1989 by Kraetschmer, Fostiropoulos, and Huffman using refractory carbon fragments created via electron bombardment in graphite arc experiments.⁵

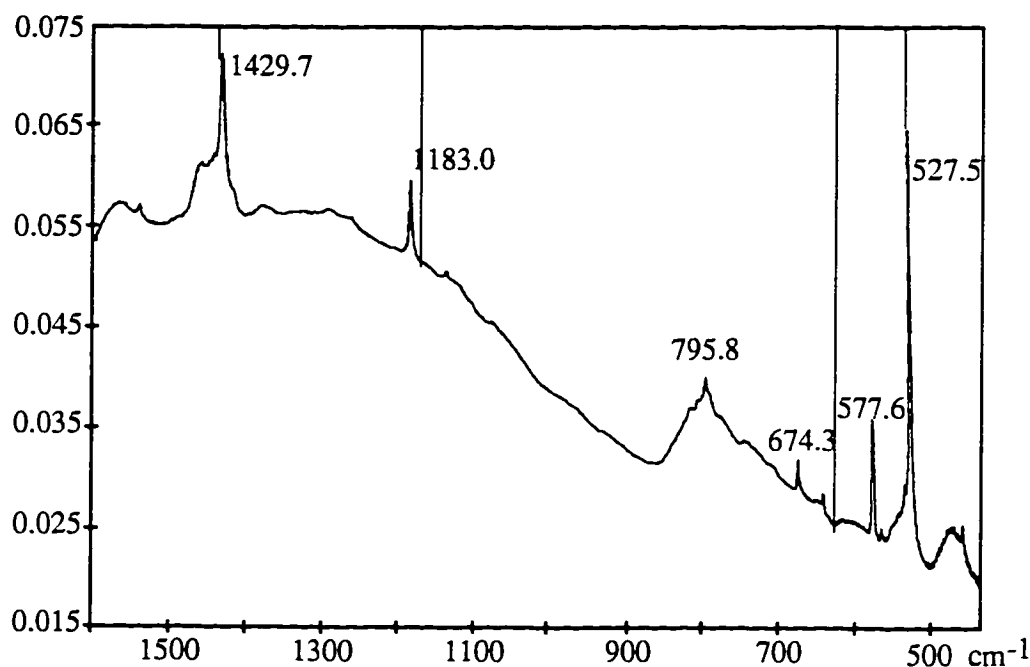


Figure 1.3 Dipole active IR spectra for C_{60} buckyball⁵. Superimposed vertical lines are T_{1u} eigenvalues to classical spring mass model.²

This led Huffman to suspect that C_{60} might be present there. Using a program written by Weeks, Huffman studied various fits to his data. He also produced spectra of refractory soot made with ^{13}C and noticed the downshifts matched the predictions perfectly.

About a year later, some of these carbon clusters were found to be soluble in benzene and toluene and were amenable to separation by column chromatography.^{6,7} With this elegant means of manufacture and separation X-ray⁸, NMR and electron scattering experiments became possible with crystal precipitate and it became abundantly clear that C_{60} existed in the form of Buckyball. Thin film STM experiments revealed hexagonal

close packing of spherical C₆₀ and spheroidal C₇₀ with spacings conducive with predictions.

It should be noted that the Fullerene family is by no means restricted to the structures listed above, but also include a myriad of complex structures, varying from the spherical Buckminsterfullerene (C₆₀) to elongated carbon "bucky-tubes"¹⁰. Mass spectroscopy even shows evidence of superfullerenes made of hundreds of carbon atoms⁹, and TEM reveals Fullerenes nesting in a fashion similar to the layers of an onion.¹⁰

Fullerite

The properties of solid phase C₆₀ (Fullerite) has received much attention in chemistry and solid state circles. Strong evidence indicates that even in solid form the rotational motion is virtually unhindered. For temperatures above 260° K a face centered cubic (fcc) lattice with T_h symmetry is preferred but disorder in the rotational orientation of the individual C₆₀ molecules makes the detailed overall crystal symmetry a dynamical one. Below 260° K the crystal structure undergoes a phase change to a simple cubic (sc) lattice symmetry due to long range ordering of rotational orientation. This may be viewed as interlocking simple cubic sublattices with electron rich 2-fold axes aligning with the electron poor 5-fold axes as in figure 1.4. This occurs with a reduction of lattice spacing.^{11,12}

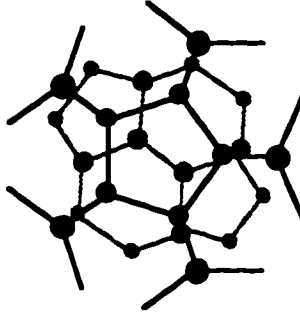


Figure 1.4 Scheme for intermolecular rotational ordering in Fullerite.

Furthermore, it is likely that at still lower temperatures a higher degree of ordering is achieved in which the molecular motion is of a librational nature. One possible scheme to achieve this is to have a simple cubic arrangement of Buckyball molecules with the 6 nearest neighboring buckyballs forming two sp_3 like bonds at the 2-fold axes. The crystal point group is reduced to T_h symmetry space group is reduced to T_h symmetry as depicted in figure 1.5 and the space group is $T_h(m3)$.

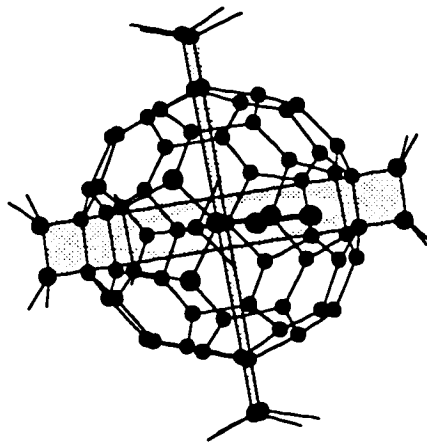


Figure 1.5 View of buckyball showing tetrahedrally placed planes containing 12 sp_3 atoms

The natural proclivity for planar aromatic hydrocarbon bonding is evident to a high degree for the spheroidal Fullerene family. The high order of symmetry in buckyball implies a higher propensity for large degeneracies in the excited molecular orbitals. Also, with a well defined interior and exterior the possibility for loose Van der Waals bonding exists above and beyond typical covalent forms. Many intriguing forms of doped Fullerenes have already been discovered.

Fullerene Doping

Doping of Fullerene molecules can be characterized by the position of the dopant (X) with respect to the closest related parent Fullerene (C_n). Endohedral doping refers to the case where the dopant is enclosed in the interior of the cage of carbon atoms and is written $X@C_n$. Initial models treated the dopant as being trapped at the center of a spherical or icosahedral potential; however, recent evidence points to a nonconcentric placement of X.^{13,14} This position may be fixed or tunnel between differing regions of the icosahedral potential, thus it is also necessary to characterize the local symmetry of the potential occupied by the dopant. The first proposed cases of endohedral doping, $La@C_{60}$,¹ happened nearly concurrently with Kroto's et. al. discovery of Buckyball, but it was not verified until years later by Fourier transform ion cyclotron resonance that it was truly situated inside the fullerene.¹⁵ Recently, an abundance of promising endohedral derivatives have been reported ranging from the $Ti@C_{28}$, $Hf@C_{28}$, $Zr@C_{28}$, $U@C_{28}$ family¹⁶, the $La@C_{82}$,¹⁷ $Y@C_{82}$, $Y_2@C_{82}$,¹⁸ $Sc_3@C_{82}$ family^{19,20} on through the enormous $La_4@C_{114}$.²¹ The study of endohedrally trapping larger numbers of atoms is at present receiving a great deal of attention. The manufacture of nanowires in which large tubular Fullerenes with a linear network of endohedral metallic atoms is currently under investigation.²² The list of periodic elements amenable to endohedral doping is growing, but remains far from complete and is currently a topic of great interest.²³

Intrahedral doping refers to the case where the dopant (X) actually is a structural component of the fullerene cage itself. This can be viewed as a substitution of one or more of the parent Fullerene's carbon atoms (X_mC_{n-m}), which often breaks the symmetry of the C_n progenitor. Reported candidates of intrahedral doping include BC_{59} ,²⁴ NC_{59} ,²⁵ BC_{58} and $C_{58}B-NH_3$.²⁶ An analogous family of metallocarbohedranes exists in the form M_8C_{12} ($M=Hf, Ti, Zr, V$)²⁷. These latter forms have T_h symmetry which is a maximal subgroup of Y_h . Also of interest to spectroscopist is the subject of isotopic intrahedral doping by ^{13}C . Typical natural abundances of ^{13}C in carbon sources used in the manufacture of Fullerenes have been on the order of 1%. This nontrivial contribution of various $^{13}C_m^{12}C_{n-m}$ members has a marked effect on high resolution spectra and will be one of the main topics of this thesis.

Lastly, exohedral doping of the Fullerenes describes the case in which additional atoms or complexes bond on the exterior of the carbon lattice. Due to the availability of the remaining valence electron left over from the sp^3 hybrid orbitals the exohedral reactivity of the fullerene family is quite profound. Many instances of exohedral bonding continue to be reported. Among these are ionic hydrogenation²⁸ and fluorination²⁹, metallic chelation³⁰, LaC_{60} ³¹ and other exotic complexes such as $(\eta^2-C_n)Ir(CO)Cl(PPh_3)_2$.³² Indeed, Osmylated C_{60} dubbed Bunnyball (Figure 1.6) was first used to determine by Xray crystallography the bond lengths joining the pentagonal and hexagonal carbons.³³

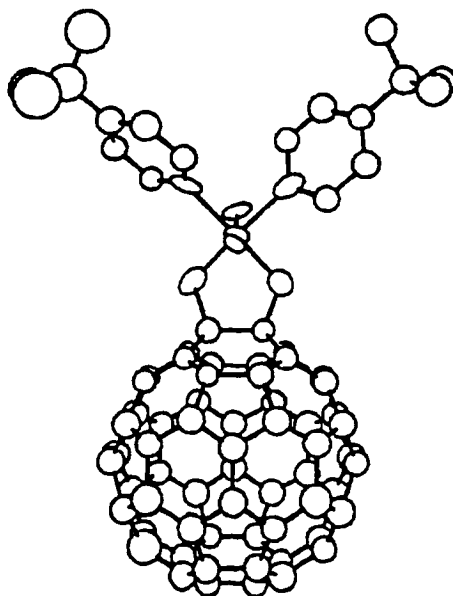


Figure 1.6 View of Osmylated C₆₀. { Reference 33 }

Doping Fullerite

The previous doping formalisms can be carried over to the solid phase Fullerites. Molecular solids are characterized by weak Van der Waals intermolecular bonding and may be viewed as exohedral doping. Doped Fullerite has shown many remarkable properties. Of particular interest is the family of Alkali doped family of Fullerite A_nC₆₀, n=1...6. This family of solids exhibit superconducting transitions with critical temperatures ranging up to 33° K.³⁴ By varying the amount and types of alkali dopants during formation, electronic transport properties may be varied from insulating (n=6) through superconducting (n=3) phases. In such a manner, critical temperatures may also be varied for a multitude of checks on superconducting models.

Also of interest to the material sciences is the extraordinary rotational motion of C₆₀ Fullerites that survives as far down as 77° K. There is evidence of several order- disorder

phase changes at various temperatures and pressures.³⁵ One of these high pressure states shows a hardness greater than that of diamond.³⁶ The rotational degrees of freedom may be an important part of the low energy lattice dynamics of Fullerenes and doped Fullerene structures. There has never been a crystal made of a molecule that is so spherical. Since the icosahedral group Y_h is the largest rotational point group in three dimensions, C_{60} may prove to be the largest most spherical molecule ever to be studied. While seeking a theory for Fullerene-alkali superconductivity one should not ignore any possible coupling mechanisms such as collective rotation-vibrations of the carbon clusters. The presence of ^{13}C isotopes may also affect the low energy Fullerene lattice dynamics if C_{60} rotations were involved. An understanding of gas phase rotational dynamics may help to better understand dynamics of these icosahedrally hindered rotors and rotational phase transitions in Fullerene solids.

With these thoughts in mind, it is the purpose of this thesis to present an analysis of the rotational dynamics and spectral level structure of C_{60} Fullerene and for various doped Fullerenes exhibiting broken icosahedral symmetry. To do this, symmetry analysis will be exploited.

Chapter 2 Geometric Model and Symmetry

History

The accepted geometrical structure for C_{60} has a history dating back over 500 years. The first rendition of this structure is attributed to Peiro della Francesca in 1492.¹ This is the same shape as the modern European football and is related to two of the Archimedean solids namely the dodecahedron and the icosahedron.

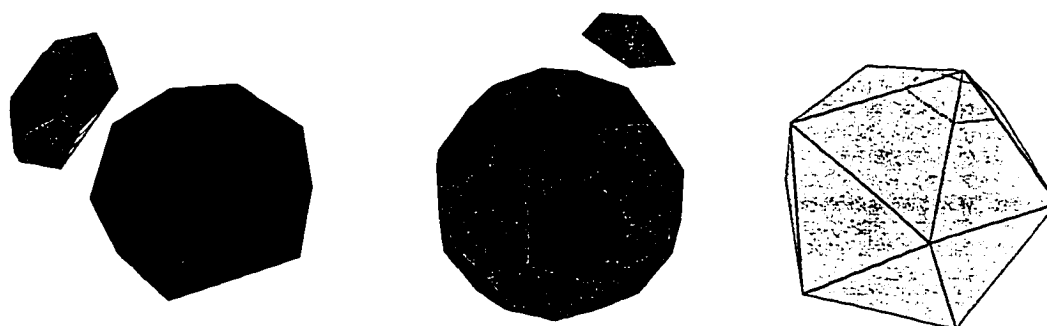


Figure 2.1 Geometric relation between the dodecahedron (left), truncated icosahedron (center), and regular icosahedron (right).

The oldest regular polyhedron, the dodecahedron, dates back to the 7th century Etruscans near Padua.¹ Truncation of either of these polyhedra so that the remaining sides are of equal length delivers the semi-regular truncated icosahedron. Indeed, the pentagram first used to tessellate the dodecahedron was used earlier as an identification of the Pythagorean secret society. Initiates were required to draw the pentagram quickly with one stroke. Plato later developed a theory in his dialog 'Timaeus' describing the four 'elements', air, earth, fire, and water as being constructed of regular polyhedra.¹

Rotational Symmetry

The aforementioned polyhedra can be seen to have the same rotational symmetry. Considering all possible rotations that bring the vertices back into alignment, 60 equivalence classes are formed. These classes are isomorphic to the icosahedral rotational group Y with composition playing the role of group operator. (Here we use the conventional notation Y for the group.)

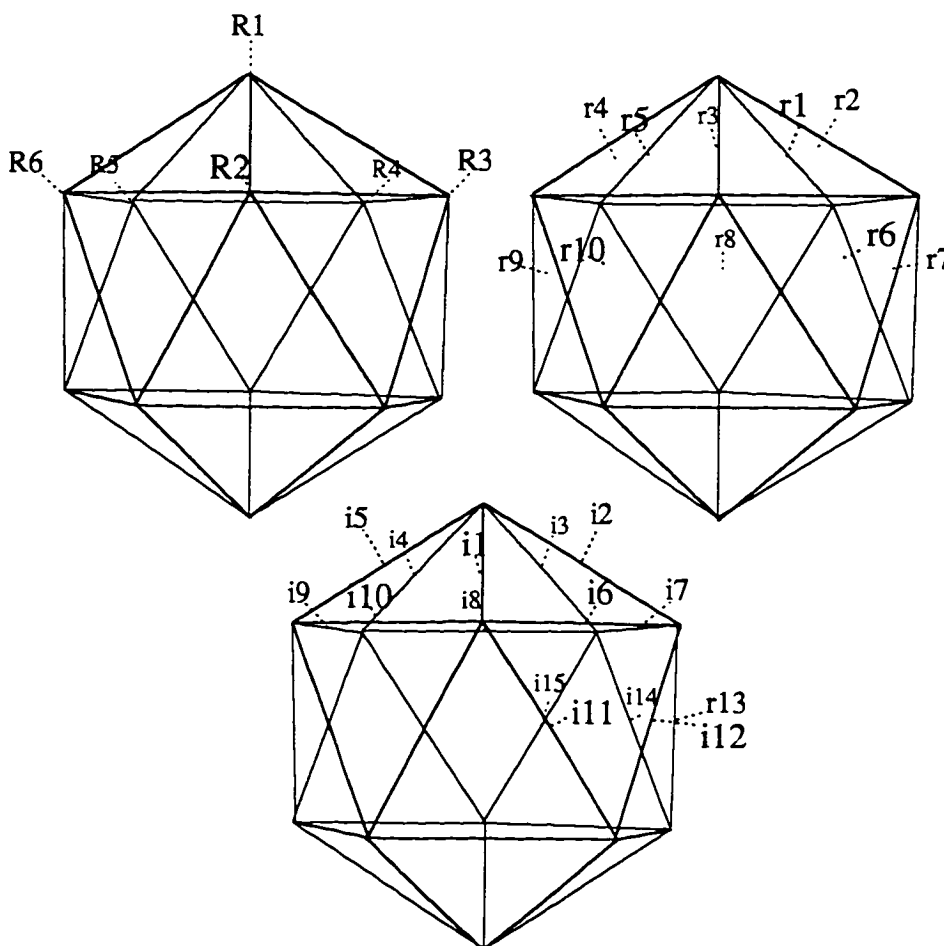


Figure 2.1 Labeling of icosahedral rotational axes.

The rotational operators will be labeled as follows. Rotations that are multiples of 72° are assigned an upper case 'R', rotations that are multiples of 120° labeled by a lower case 'r', rotations divisible by 180° are labeled 'i', and those divisible by 360° are labeled '1'. There are six two sided C_5 axes, corresponding to six rotations R_1, \dots, R_6 respectively. Similarly, the ten C_3 axes are associated with rotations r_1, \dots, r_{10} , and the fifteen C_2 axes are i_1, \dots, i_{15} . The individual operators are assigned a plus sign to denote a counter-clockwise rotation of less than 360° (a minus sign for a clockwise rotation of less than or equal to 360° will be introduced later to treat half-integral angular momenta). Figure 2.1 enumerates these axes of rotation. A final integer serves as a power or exponent to indicate the number of the fundamental rotations in each operator. For example, R_{1+3} is a rotation about the R_1 axis by $3 \times 72^\circ$ in the counter-clockwise direction. With this formalism, the inverse of R_{1+1} is R_{1+4} . The multiplication table is presented in appendix A.

As is the case with all semi-regular polyhedra, the vertices are equidistant from their neighbors and equidistant from the center. For the icosahedron, it is also interesting to note that joining two opposing segments of two-fold symmetry a rectangle is formed with the ratio of the side lengths being the golden mean or Fibonacci generator $F^+ = (1 + \sqrt{5})/2$. Two other congruent mutually perpendicular golden rectangle's can be formed containing all 12 of the vertices. Since for any given vertex there are 5 possible choices to form the original rectangle, there are 5 equivalent body defined Cartesian coordinates.

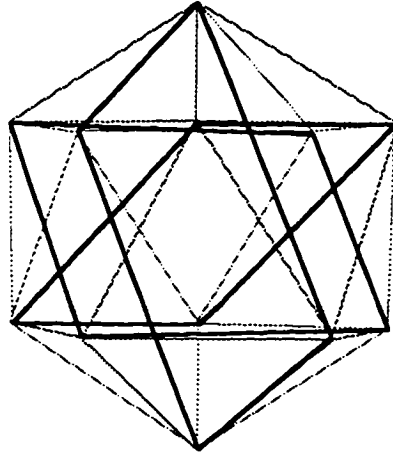


Figure 2.2 Icosahedron with 3 inscribed golden rectangles.

Symmetry Analysis

Symmetry analysis begins by determining the commutation class operators (Table 2.1), given by the relation,

$$C_h = \sum_{g \in Y} ghg^{-1} \quad (2.1)$$

Icosahedral group class structure

$\omega=0$	$\omega=72$	$\omega=144$	$\omega=120$	$\omega=180$
	$\omega=360 - 72$	$\omega=360 - 144$	$\omega=360 - 120$	
1+	R1+1	R1+2	r1+1	i1+
	R1+4	R1+3	r1+2	i2+
	R2+1	R2+2	r2+1	i3+
	R2+4	R2+3	r2+2	i4+
	R3+1	R3+2	r3+1	i5+
	R3+4	R3+3	r3+2	i6+
	R4+1	R4+2	r4+1	i7+
	R4+4	R4+3	r4+2	i8+
	R5+1	R5+2	r5+1	i9+
	R5+4	R5+3	r5+2	i10+
	R6+1	R6+2	r6+1	i11+
	R6+4	R6+3	r6+2	i12+
			r7+1	i13+
			r7+2	i14+
			r8+1	i15+
			r8+2	
			r9+1	
			r9+2	
			r10+1	
			r10+2	

Class Operators

$$C_1 = \{1\}$$

$$C_R = \{R_1 + \dots + R_6 + R_1^4 + \dots + R_6^4\}$$

$$C_{R^2} = \{R_1^2 + \dots + R_6^2 + R_1^3 + \dots + R_6^3\}$$

$$C_r = \{r_1 + \dots + r_{10} + r_1^2 + \dots + r_{10}^2\}$$

$$C_i = \{i_1 + \dots + i_{15}\}$$

Table 2.1 Class structure of the icosahedral group is shown in the highlighted boxes. Class operators are sums over corresponding class elements.

With these class operators which now commute the class multiplication table 2.2 can be constructed,

	C_1	C_R	C_{R^2}	C_T	C_i
C_1	C_1	C_R	C_{R^2}	C_T	C_i
C_R	C_R	$12C_1 + 5C_R$ $+C_{R^2} + 3C_T$	$C_R + C_{R^2}$ $+3C_T + 4C_i$	$5C_R + 5C_{R^2}$ $+3C_T + 4C_i$	$5C_{R^2} + 3C_T$ $+4C_i$
C_{R^2}	C_{R^2}	$C_R + C_{R^2}$ $+3C_T + 4C_i$	$12C_1 + C_R$ $+5C_{R^2} + 3C_T$	$5C_R + 5C_{R^2}$ $+3C_T + 4C_i$	$5C_R + 3C_T$ $+4C_i$
C_T	C_T	$5C_R + 5C_{R^2}$ $+3C_T + 4C_i$	$5C_R + 5C_{R^2}$ $+3C_T + 4C_i$	$20C_1 + 5C_R$ $+5C_{R^2} + 7C_T$ $+8C_i$	$5C_R + 5C_{R^2}$ $+6C_T + 4C_i$
C_i	C_i	$5C_{R^2} + 3C_T$ $+4C_i$	$5C_R + 3C_T$ $+4C_i$	$5C_R + 5C_{R^2}$ $+6C_T + 4C_i$	$15C_1 + 5C_R$ $+5C_{R^2} + 3C_T$ $+2C_i$

Table 2.2 Commutation class multiplication table.

The icosahedral character table (Table 2.3) can be constructed from the commutation classes as shown in the appendix.

Y	C_1	C_R	C_{R^2}	C_T	C_i
A	1	1	1	1	1
T_1	3	F^+	F^-	0	-1
T_3	3	F^-	F^+	0	-1
G	4	-1	-1	1	0
H	5	0	0	-1	1

Table 2.3 Icosahedral group character table.

Owing to the size of the group, the icosahedral symmetry species contain an extraordinary degree of degeneracy. There is only one singlet labeled *A*, two types of *T*-triple degeneracies, a *G*-four fold degeneracy, and one *H*-five fold degeneracy. Correlations with the $O(3)$ supergroup can be determined using the techniques described in the appendix. The frequency of correlations are given in table 2.4.

O(3)↓Y _h	A _g /A _u	T _{1g} /T _{1u}	T _{3g} /T _{3u}	G _g /G _u	H _g /H _u
+0/-0	1	0	0	0	0
-1/+1	0	1	0	0	0
+2/-2	0	0	0	0	1
-3/+3	0	0	1	1	0
+4/-4	0	0	0	1	1
-5/+5	0	1	1	0	1
+6/-6	1	1	0	1	1
-7/+7	0	1	1	1	1
+8/-8	0	0	1	1	2
-9/+9	0	1	1	2	1
+10/-10	1	1	1	1	2
-11/+11	0	2	1	1	2
+12/-12	1	1	1	2	2
-13/+13	0	1	2	2	2
+14/-14	0	1	1	2	3
-15/+15	1	2	2	2	2
+16/-16	1	2	1	2	3
-17/+17	0	2	2	2	3
+18/-18	1	1	2	3	3
-19/+19	0	2	2	3	3
+20/-20	1	2	2	2	4
-21/+21	1	3	2	3	3
+22/-22	1	2	2	3	4
-23/+23	0	2	3	3	4
+24/-24	1	2	2	4	4
-25/+25	1	3	3	3	4
+26/-26	1	3	2	3	5
-27/+27	1	3	3	4	4
+28/-28	1	2	3	4	5
-29/+29	0	3	3	4	5
+30/-30	2	3	3	4	5
-31/+31	1	4	3	4	5

Table 2.4 Frequency table correlating O(3) symmetry species with those of Y_h.

The all-commuting projection operators are defined by the relation,

$$P^\alpha = \frac{l^\alpha}{{}^0G} \sum_{C_g} \chi_{C_g}^{\alpha*} C_g \quad (2.2)$$

where the χ are the characters as tabulated above, $l^\alpha = \chi^{\alpha C_1}$ is the order of degeneracy for the α species, and ${}^0G = 60$ is the order of the generating group Y. All-commuting

projection operators will be instrumental in forming representations and transforming operators to a symmetry defined basis. Procedures for finding the idempotent all-commuting projection operators are given in appendix B.

Chapter 3 Molecular Eigenstates and Eigenvalues

Born-Oppenheimer Approximation

Molecular spectra typically exhibit more structure and complexity than atomic spectra. This is due to the greater degree of freedom inherent in a larger systems of constituent particles. Molecular states are determined by not only by the motion of the constituent electrons, but also on the collective motion of the nuclei and possible interactions between these types of particles. Even three body problems must be treated using approximations or by numerical computation. New techniques will be needed in the analysis of Buckyball and related doped Fullerenes.

The Schrodinger equation for quantized molecular states and their corresponding eigenvalues can be written in the form,

$$\begin{aligned} \mathbf{H}\psi(x..., X...) = \\ \left(\frac{1}{2m_e} \sum_e \mathbf{p}_e^2 + \frac{1}{2m_N} \sum_N \mathbf{P}_N^2 + V_{ee}(x...) + V_{NN}(X...) + V_{eN}(x..., X...) \right) \psi(x..., X...) = \\ E\psi(x..., X...) \end{aligned} \quad (3.1)$$

where x denotes the position of electron 'e', and X the position of nucleus 'N'. E is the energy eigenvalue and the V terms are the Coulomb potentials for the electron-electron, electron-nuclei, nuclei-nuclei interactions respectively.

Due to the small mass of an electron, one expects that the electronic eigenstates adiabatically follow the motion of the slower nuclei and thereby give arise to an effective potential for the nuclei. In this approximation, a given arrangement of nuclei are

considered rigidly fixed in space. Equation 3.1 is modified by omitting the purely nuclear terms and a complete set of electronic eigenfunctions $\xi_\epsilon = (\mathbf{x}\dots, \mathbf{X}\dots)$ can be obtained through solution of this 'electronic' Schrödinger equation (3.2),

$$\left(\frac{1}{2m_e} \sum_e \mathbf{p}_e^2 + V_{ee}(\mathbf{x}\dots) + V_{eN}(\mathbf{x}\dots, \mathbf{X}\dots) \right) \xi_\epsilon(\mathbf{x}\dots, \mathbf{X}\dots) = E_\epsilon(\mathbf{X}\dots) \xi_\epsilon(\mathbf{x}\dots, \mathbf{X}\dots) \quad (3.2)$$

where ϵ is the electronic quantum number of the solutions having energy E_ϵ . Naturally the nuclei would not be truly fixed in space. Displacements of the nuclei would relate to a change in the above electron energies E_ϵ , thereby changing their potential energy. Adding this term to the nuclear Coulomb terms gives rise to the effective potential in the 'nuclear' Schrödinger equation (3.3).

$$\left(\sum_N \frac{\mathbf{p}_N^2}{2m_N} + V_{NN}(\mathbf{X}\dots) + E_\epsilon(\mathbf{X}\dots) \right) \eta_{\epsilon,v}(\mathbf{X}\dots) = E_{\epsilon,v} \eta_{\epsilon,v}(\mathbf{X}\dots) \quad (3.3)$$

The molecular energies $E_{\epsilon,v}$ are classified by nuclear quantum number v of the nuclear state for the electronic state having quantum number ϵ . Stable nuclear eigenfunctions will exist, if the combined effect of the Coulomb potential V_{eN} and the kinetic terms $\frac{1}{2m_e} \mathbf{p}_e^2$ dominate the repulsive terms V_{NN} and V_{ee} . Adiabaticity of electronic eigenfunctions allows separate treatments of the two types of motion.

$$\Psi_{\epsilon,v}(\mathbf{x}\dots, \mathbf{X}\dots) \approx \xi_\epsilon(\mathbf{x}\dots, \mathbf{X}\dots) \eta_{\epsilon,v}(\mathbf{X}\dots) \quad (3.4)$$

Care must be taken for equation 3.4 is not a product of separable independent functions, since ξ_ϵ depends on nuclear positions \mathbf{X} as adiabatically varying parameters and η depends explicitly on the effective potential produced by the electronic state ϵ .

Many regions within molecular spectra, especially in smaller molecules, are amenable to approximations of this type. Typical transitions in molecular spectra do not manifest themselves as single lines, but are composed of many bands of less energetic transitions such as the aforementioned nuclear motions. With slower motions adiabatically following faster ones a spectral hierarchy results. Separations in electron energy levels are often of the order of 10^4 $\{\text{cm}^{-1}\}$, vibrational separations range from 10^2 - 10^3 $\{\text{cm}^{-1}\}$, and rotational splittings on the order of 10 $\{\text{cm}^{-1}\}$ or less. As spectroscopic resolution is further increased finer detail would be revealed and other interactions or motion would be involved. We could then generalize the arguments above and approximate the total molecular eigenfunctions through each mechanism.

$$\Psi_{\epsilon,v,\rho,\dots}(x_{\dots}; X_{\dots}; \alpha, \beta, \gamma; \dots) \approx \xi_{\epsilon}(x_{\dots}; X_{\dots}; \alpha, \beta, \gamma; \dots) \eta_{v(\epsilon)}(X_{\dots}; \alpha, \beta, \gamma; \dots) r_{\rho(v(\epsilon))}(\alpha, \beta, \gamma; \dots) \dots$$

(3.5)

Nuclear vibrational modes X_{\dots} and Euler angles α, β, γ serve as adiabatic parameters for electronic wavefunctions $\xi_{\epsilon}(x_{\dots})$, and Euler angles serve as parameters for nuclear wavefunctions $\eta_{v(\epsilon)}$, but are the actual coordinates for the rotational wavefunction $r_{\rho(v(\epsilon))}(\alpha, \beta, \gamma)$. However, the quantum numbers ρ of the rotational waves are functions of the vibrational state labels v which are in turn dependent upon which electronic state is in effect.

Electronic Energy levels

To illustrate the ramifications of the Buckminsterfullerene molecular structure, symmetry analysis can be used to investigate the electronic eigenvalues. The Hückel Approximation has often been used to estimate the electronic energy levels of aromatic hydrocarbon molecules. For Buckyball, this problem involves treating each of the 60 carbon atoms as having one non-bonding electron, and the other 3 valence electrons as

bonding locally and are deemed negligible. Furthermore only nearest-neighbor orbitals are considered to resonate. One possible solution would involve diagonalizing the Hückel hamiltonian \mathbf{H}_H which has a 60x60 representation in the rotational operator basis. Each row of this representation contains one Coulomb integral -H, two resonance integrals for pentagonal bonds-S, and one resonance integral-T for the C_2 symmetric hexagonal bonds.

$$\begin{array}{c|cccccccc} \mathbf{H}_H & 1 & \mathbf{R}_1 & \mathbf{R}_1^2 & \mathbf{R}_1^3 & \mathbf{R}_1^4 & \dots & i_1 & \dots \\ \hline 1 & H & S & \cdot & \cdot & S & \dots & T & \dots \end{array}$$

Figure 3.1 First row of Hückel Hamiltonian in the rotational operator basis.

Another technique¹ utilizes the full Y_h symmetry of the icosahedron and diagonalizing with respect to the C_{5i} subgroup. This reduces the problem to a block diagonalized representation composed of ten 6x6 blocks, four of which that can be obtained through complex conjugation of the other characteristic polynomials.

The approach taken here utilizes the Y all-commuting projection operators of equation 2.2 to transform \mathbf{H}_H into a Y -symmetry define basis. In order to label the symmetry species of the individual blocks, one notes that the carbon occupies a site with only C_v symmetry, or C_1 if only rotational symmetry is considered. Inducing the $0_I C_1$ species to the icosahedral group proscribes the regular representation.

$$0_I \uparrow Y = A \oplus 3T_1 \oplus 3T_3 \oplus 4G \oplus 5H \quad (3.6)$$

This indicates that upon projection there will be one 1x1 block giving the A eigenvalue, three repeated 3x3 T_1 blocks, three repeated 3x3 T_3 blocks, four repeated 4x4 G blocks, and five identical 5x5 H blocks. So by this method the largest diagonalization necessary will be that of a 5x5 block. Also, this technique requires only the first row of the Hueckel Hamiltonian and irreducible representations for the rotational operators joining neighboring sites, namely, $1, \mathbf{R}_1, \mathbf{R}_1^4, i_1$. The Hamiltonian in the symmetry defined basis then has the following form.

$$\langle \alpha_{ja} | \mathbf{H} | \alpha_{jb} \rangle = \sum_{\mathbf{g}} \langle 1 | \mathbf{H} | \mathbf{g} \rangle D_{ab}^{\alpha}(\mathbf{g}) \quad (3.7)$$

Where $D_{ab}^{\alpha}(\mathbf{g})$ is the (a,b) element of the α^{th} irreducible representation of operator \mathbf{g} . Results for the case where $H=0$; and $S, T=-1$ are tabulated in table 3.2.

T_3	$1 + F^+$	2.618034
G	$(1 + \sqrt{17})/2$	2.561553
G	2	2.000000
H	F^+	1.618034
T_3	β^+	1.438283
H	$(-1 + \sqrt{13})/2$	1.302776
T_1	$1 + F^-$	0.381966
T_1	α^+	0.138564
H	F^-	-0.618034
G, H	-1	-1.000000
G	$(1 - \sqrt{17})/2$	-1.561553
T_3	β^-	-1.820249
H	$(-1 - \sqrt{13})/2$	-2.302776
T_1	α^-	-2.756598
A	-3	-3.000000

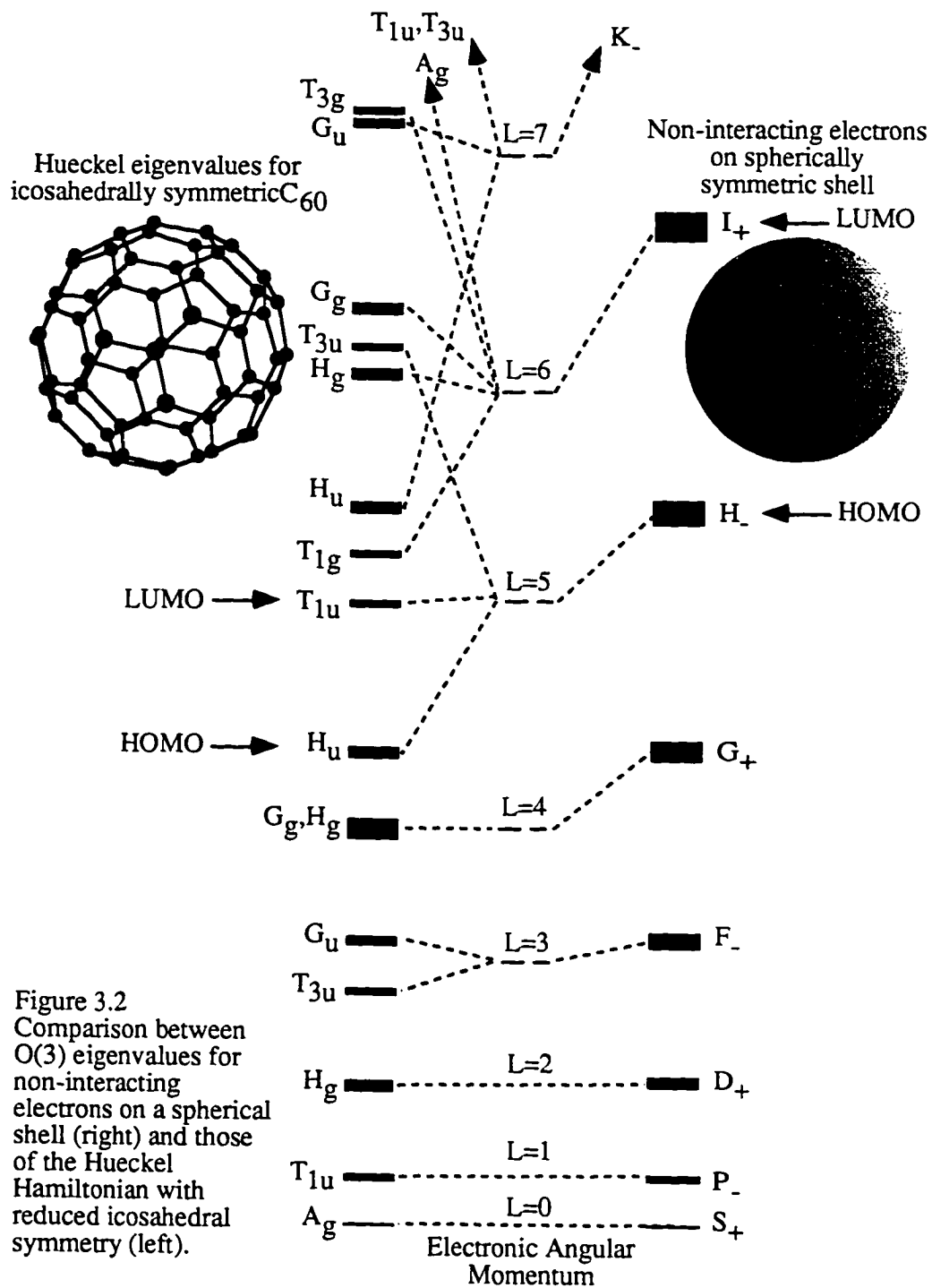
Table 3.2 Eigenvalues and Y symmetry species for Hueckel Hamiltonian

$$\alpha^{\pm} = \left(-(F^+)^2 \pm \sqrt{9 + F^-} \right) / 2, \beta^{\pm} = \left(-(F^-)^2 \pm \sqrt{9 + F^+} \right) / 2$$

Comparisons between eigenvalues of the Hückel Hamiltonian and that of a spherically symmetric shell illustrates the effects of the icosahedral lattice. Non-interacting electrons in a spherical environment have eigenvalues dependent on the electron angular momentum L .

$$\epsilon_L = \epsilon_\delta L(L+1) + \epsilon_0 \quad (3.8)$$

For $\epsilon_0 = -3$, and $\epsilon_\delta = (\alpha^- - 3)/2$, equation 3.8 is set to the scale of the Hückel problem. Figure 3.2 shows the splitting that the $O(3)$ eigenvalues undergo when lowered to icosahedral symmetry. The F_2 - $O(3)$ species is the lowest that exhibits symmetry breaking. The G_+ level though correlated with the G_g , and H_g species has an incidental degeneracy and remains unsplit. With larger angular quanta the mixing of states become more prevalent and overlap of states occurs. In the molecular ground state the sixty electrons fill the lowest available states, the HOMO H_u Y-state forms a closed shell, however the HOMO H_2 - $O(3)$ state is only partially filled and is of higher energy. This inferred stability is supported by the wide range of observed ions and ionic bonding in doped Fullerite.



Vibrational Eigenvalues

Symmetry analysis also lends itself to the study of the vibrational modes of C_{60} . In the harmonic approximation the vibrational problem is modeled by Newton's second law.

$$\mathbf{M} \frac{d^2}{dt^2} |\psi_v\rangle = -\mathbf{K} |\psi_v\rangle \quad (3.9)$$

There are three degrees of freedom for each of the 60 carbon nuclei so equation 3.9 is a system of 180 coupled differential equations. Symmetry defined Cartesian coordinates may be set up in terms of the plane of reflection containing each nuclear equilibrium position. A radial displacement has A_+ C_v and the remaining two axes can be set up to straddle the plane of symmetry so that they are reflections of each other with A_+ and A_- symmetry. Induction of these local symmetry species to Y_h forms symmetry defined modes of the following icosahedral species.

$$2A_+ \oplus A_- \uparrow 2A_g \oplus 4T_{1g} \oplus 4T_{3g} \oplus 6G_g \oplus 8H_g \oplus \\ A_u \oplus 5T_{1u} \oplus 5T_{3u} \oplus 6G_u \oplus 7H_u \quad (3.10)$$

Since the improper vibrations (translation and rotation) are handled in separate treatments, one T_{1u} , and one T_{1g} should be removed from 3.10 leaving the species of the 174 true vibrational modes.

The dipole transition operator has T_{1u} symmetry. Only those vibrational states α that contain an A_g upon cross product with T_{1u} will be dipole active, to first order.

$$\begin{aligned}\alpha \otimes T_{1u} &= A_g \\ \alpha &= T_{1u}\end{aligned}\tag{3.11}$$

Thus only the four T_{1u} modes should be observed in vibrational infra-red spectra.

Similarly, Raman transitions have the same first order selection rules as quadrupole transitions. The symmetry species of the quadrupole operator can be derived by forming the cross product of two dipole species and retaining only those products with symmetric coupling coefficients. A listing of cross products of icosahedral species is given in appendix C.

$$\begin{aligned}T_{1u} \otimes T_{1u} &= A_g \oplus H_g \oplus H_g \\ \alpha \otimes (A_g \oplus H_g) &= A_g \\ \alpha &= A_g, H_g\end{aligned}\tag{3.12}$$

Therefore, 2 A_g and 8 H_g vibrational modes are Raman active. Figure 3.3 shows an example illustrating these Raman modes.

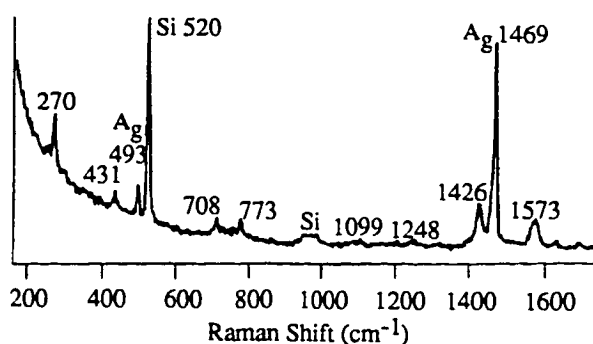


Figure 3.3 Raman spectra for C₆₀ on Si substrate.²

Rotational structure

A common type of spectral feature is the P, Q, R rotational structure. An example of a SF₆ spectrum is shown in figure 3.4.³

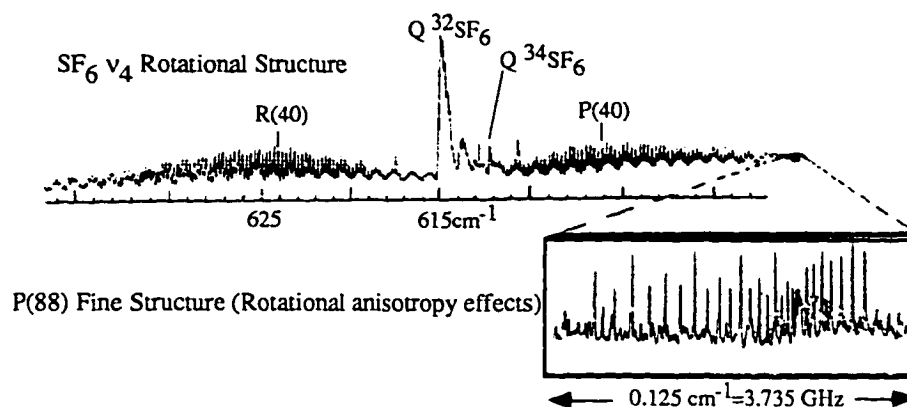


Figure 3.4 Fourier transform spectrum showing the v₄ SF₆ rovibrational structure and laser diode spectrum of the P(88) fine structure (inset).³

The rotational splittings are related to the rotational constant $B=1/2I$ (I is the moment of inertia of the spherical top molecule) and the Coriolis zeta constant ζ_v of the vibrational fundamental v . The scalar terms of the rovibrational Hamiltonian can be written as the sum of the rotational, vibrational Hamiltonians and a scalar Coriolis coupling term.

$$\mathbf{H} = \mathbf{H}_r + \mathbf{H}_v + \mathbf{H}_{rv} = \mathbf{H}_v + B\mathbf{J}^2 - 2B\zeta\mathbf{J} \cdot \boldsymbol{\ell} \quad (3.13)$$

where $\mathbf{J} = \mathbf{L}^{(e)} + \mathbf{N} + \zeta\boldsymbol{\ell}$ is the total angular momentum in terms of $\mathbf{L}^{(e)}$ the electronic angular momentum and $\boldsymbol{\ell}$ the vibrational angular momentum having integral eigenvalues. Transitions that obey the selection rules $\Delta N=0$ and $\Delta J=0, \pm 1$ give rise to the comb-like structure above with evenly spaced separations of $2B(1-\zeta)$. The Coriolis constants for the T_1 vibrational modes are given in figure 3.5. Since they are all negative this will have the effect of broadening the P and R branches.

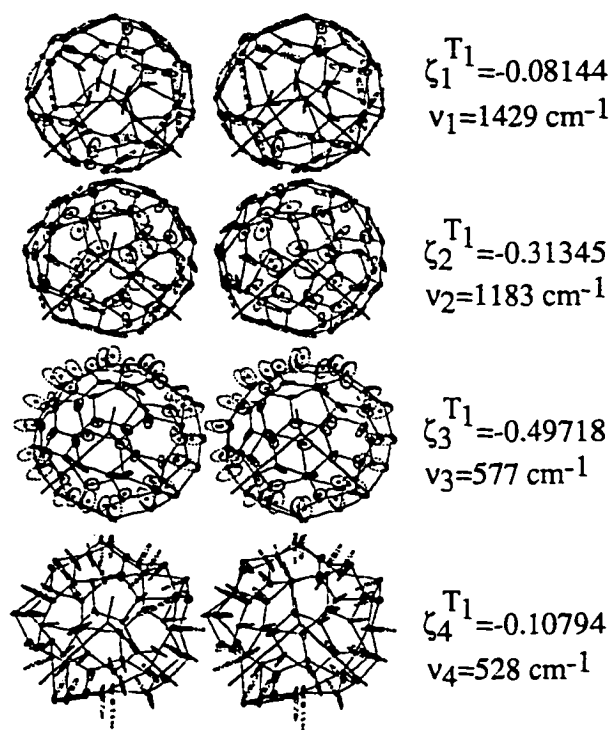
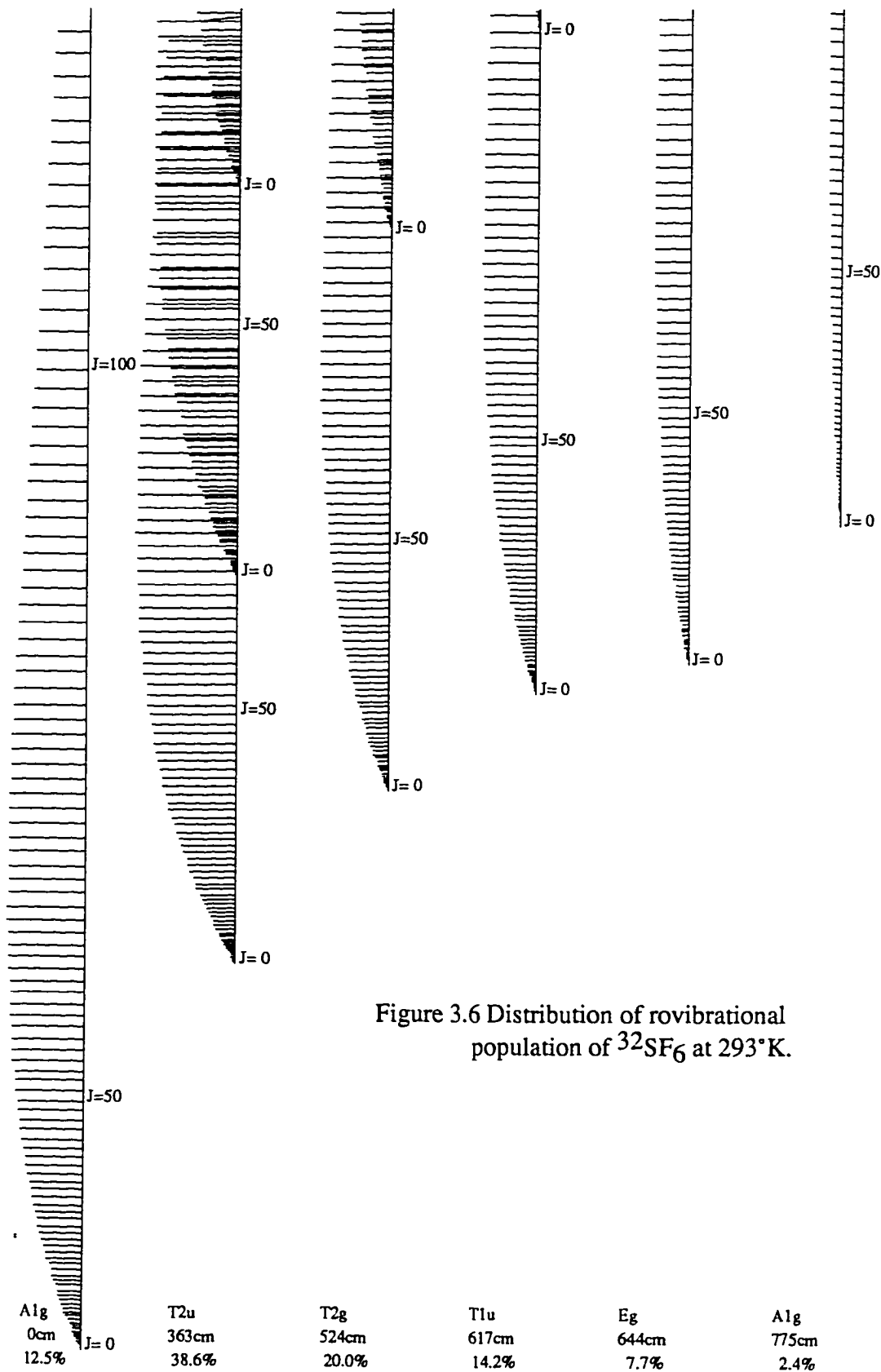
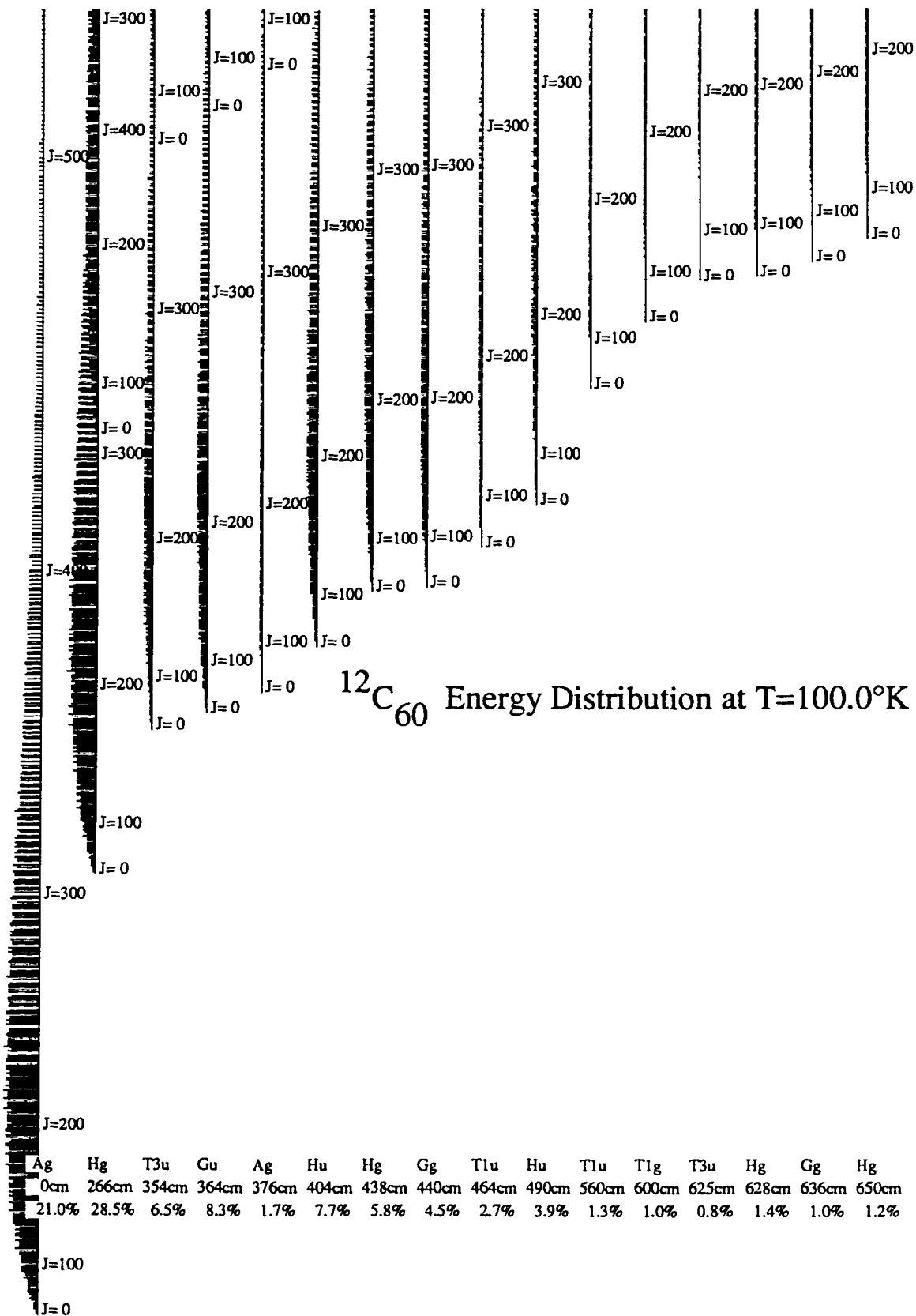


Figure 3.5 Coriolis polarized T_1 vibrational modes of C_{60} and scalar Coriolis coefficients⁴

Conversely, the rotational constant of Buckyball $B_{C_{60}} = 0.0028 \text{ cm}^{-1}$ is over an order of magnitude smaller than that of SF_6 $B_{SF_6} = 0.0912 \text{ cm}^{-1}$. This has the effect of decreasing spacings within the rotational structure as well as increasing the thermal population of higher rotational states. To illustrate this, energy distributions and percentages of population for the lowest energy rovibrational eigenstates are plotted in figure 3.6 for SF_6 at room temperature and in figure 3.7 for C_{60} cooled to 100°K .⁵





Chapter 4 Nuclear spin weights and gas phase spectral structure of $^{12}\text{C}_{60}$ and $^{13}\text{C}_{60}$ Buckminsterfullerene

Introduction

Rotational energy levels and high resolution rovibrational spectra of gas phase Buckminsterfullerene (C_{60}) is strongly effected by the Pauli exclusion principle. Very different rovibrational fine structure patterns will be seen for differing steric arrangements of ^{12}C and ^{13}C isotopes. Only the two extreme cases $^{12}\text{C}_{60}$ and $^{13}\text{C}_{60}$ actually have icosahedral symmetry. Those two cases will have relatively uncluttered spectral patterns and simpler rotational dynamics. Their analysis in turn will be a prerequisite to analyses of rotational dynamics of C_{60} with broken icosahedral symmetry due to mixed nuclear spin compositions. The Pauli principle will be incorporated in an analysis of the energy level structure possible in the pure bosonic and fermionic nuclear spin arrangements. Young tableau theory is utilized in the later case to correlate the $\text{SU}(2) \otimes \text{S}_{60}$ nuclear spin group with the $\text{Y}_h^{(d)}$ double group. Possible Superhyperfine level structure for weak and strong nuclear spin-rotation coupling will be discussed.

The natural abundance of the isotope ^{13}C is 1.108% and is 98.892% for ^{12}C . This means that only about half of resulting Buckminsterfullerene molecules are actually $^{12}\text{C}_{60}$ with full icosahedral Y symmetry. The other half contain one or more ^{13}C nuclei. The probability for C_{60} to contain m ^{13}C nuclei is

$$P_m = \binom{60}{m} (0.01108)^m (0.98892)^{60-m} \quad (4.1)$$

Even a single ^{13}C completely destroys the rotational symmetry since the atomic sites have only reflection symmetry. An extra neutron has only a small effect ($\sim 1\text{ cm}^{-1}$) on the gross vibrational spectral structure of solid C_{60} . However, the detailed rotational vibrational fine structure of gas phase C_{60} will be very sensitive to even a single replacement of a ^{12}C by ^{13}C . Also, ^{12}C has a spin-0 nucleus while ^{13}C has a spin-1/2 nucleus. Therefore the Pauli-allowed spin-rotation states of C_{60} become increasingly complicated as more of ^{12}C are replaced by ^{13}C nuclei. This affects the nuclear spin statistical weights and the hyperfine and superfine structure of high resolution spectra.

In this chapter, we will discuss and compare the possible nuclear spin rotation states and spectra for the two extreme cases of Buckminsterfullerene which still have icosahedral symmetry. The first case $^{12}\text{C}_{60}$ is entirely composed of ^{12}C and the second case $^{13}\text{C}_{60}$ is made purely of ^{13}C . We are presuming that it will be possible to obtain graphite or carbon samples that are somewhat better than 1% pure ^{12}C for the first case, and that reasonably pure ^{13}C samples will be available as well. Furthermore, we are presuming that either of these two samples can be used for synthesis of $^{12}\text{C}_{60}$ or $^{13}\text{C}_{60}$. It should be possible to obtain enough of either material to be able to carry out gas phase Fourier transform, laser diode, or saturation absorption spectroscopy, and that these samples can be cooled in nozzle or slit expansion chambers.

So far, the gas phase spectra of C_{60} even at the resolution of Fourier transform spectroscopy has been extraordinarily congested.¹ Two of the reasons for this congestion are controllable. First, low lying H_g fundamentals are excited at room temperature and this give rise to hot bands. Second, the use of carbon which has naturally abundant mixtures of ^{12}C and ^{13}C yields a panoply of complex and different spectral patterns. Fortunately, gas phase spectra has been obtained for the lower symmetry molecule SF_6 and recently SiF_4 ² down to the remarkable resolutions necessary to resolve hyperfine

structure. These findings will be used to illustrate aspects of C_{60} spectra receptive to experimental investigation.

In order to assign high resolution spectra of C_{60} it will help greatly to begin with $^{12}C_{60}$ which, as we will show, has a very simple rotational and fine structure patterns because of the Bose exclusion principle. The material must be isotopically pure enough that its simple spectral patterns are not obscured by the more complicated patterns arising from molecules which contain ^{13}C . Equation 4.1 predicts that if 99.5% pure ^{12}C samples are used then 74% of the molecules are $^{12}C_{60}$. ^{12}C purity of 99.9% yields 94% pure $^{12}C_{60}$. More complicated spectral patterns will arise from mixed isotopic $^{13}C_m^{12}C_{60-m}$ molecules even for small number ($m = 1, 2, \dots$) of ^{13}C nuclei which occur in natural populations. Furthermore, mixed isotopic species with a fixed value of m will not be easy to produce, and for $m \geq 2$ the steric placement of ^{13}C nuclei will be even less under experimental control.

Therefore, the next step in C_{60} high resolution spectroscopy (after assigning $^{12}C_{60}$ bands) should involve the isotopically purified $^{13}C_{60}$. The degree of purification of $^{13}C_{60}$ may not have to be as high as that of $^{12}C_{60}$ which has most of its rotational spectral structure removed by Bose exclusion. By contrast the $^{13}C_{60}$ molecule has astronomically high spin statistical weights, as will be shown. However, it will be necessary to avoid having a majority of spectral contributions from mixed species $^{13}C_m^{12}C_{60-m}$. Successful assignment of spectra for the latter may be difficult unless one has molecular constants obtained from spectra of $^{12}C_{60}$ and $^{13}C_{60}$.

Spin-Permutation Symmetry of $^{12}C_{60}$

^{12}C nuclei are spin zero bosons and are restricted by the Bose exclusion principle to have only totally symmetric A_g -type spin states and corresponding A -type rotational wavefunctions. Correlation frequencies were calculated using the character analysis shown in appendix B.

Table 2.4 contains a listing of the correlation frequencies through $j=31$ where cycling starts to occur, $f^{\alpha,j+30} = f^{\alpha,30} + f^{\alpha,j}$. The rotational angular momentum J -quantum values which are correlated with A_g for $J < 30$ are $J = 1, 6, 10, 12, 15, 16, 18, 20, 21, 22,$ and 24 through 28 . The others are excluded. Spectral lines based upon the excluded levels would be absent.

With the above knowledge about the state densities ρ_j , thermal distributions can be calculated where each J level has its Boltzmann population factor $\rho_J e^{-\beta E_J} / Z$. Figure 4.1 shows Boltzmann distributions for $^{12}\text{C}_{60}$, $^{13}\text{C}_{60}$, CF_4 and SF_6 . For C_{60} at room temperature the most populated levels have hundreds of rotational quanta which in turn correspond to many thousands of angular momentum sublevels. The detailed quantum mechanics of high J rotational levels and their $(2J + 1)$ -dimensional manifold of sublevels can be simplified using semi-classical models^{3,4}. For the purely bosonic fullerene $^{12}\text{C}_{60}$ the Bose exclusion principle leads to a further simplification of the quantum states and levels. Only one out of sixty rotational substates survives the symmetry exclusion.

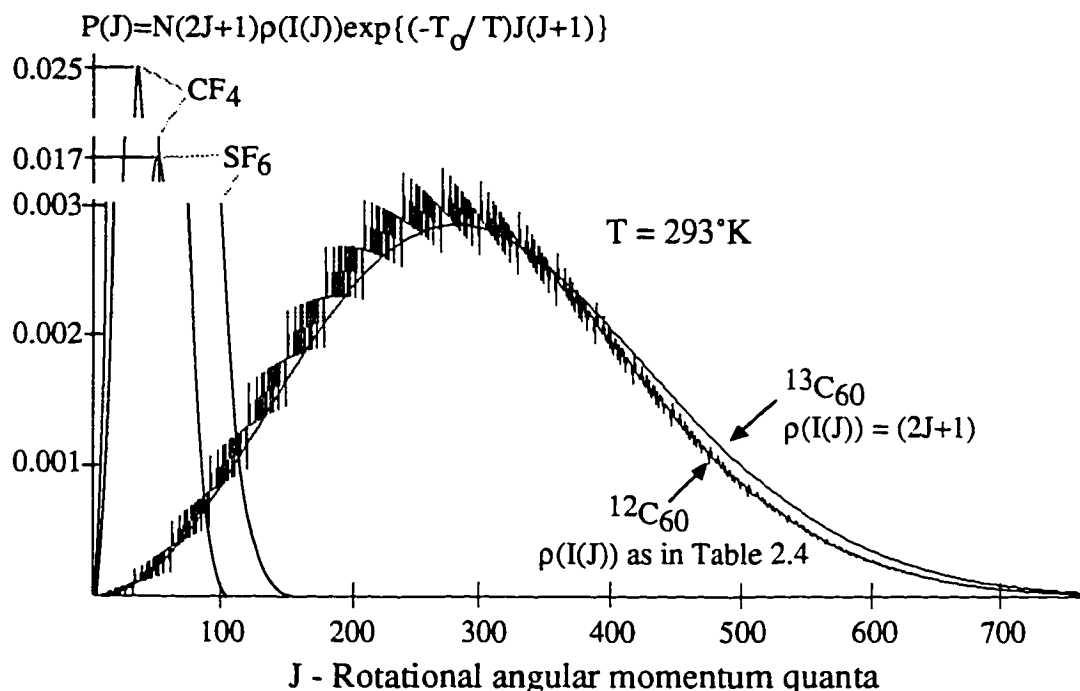


Figure 4.1 Boltzmann distribution for $^{12}\text{C}_{60}$ and $^{13}\text{C}_{60}$ at 293°K .

The Boltzmann distribution for C_{60} at 293°K has a much smaller ground rovibronic population. The fundamental $A_g \rightarrow T_{1u}$ absorption spectra become saturated or turn into emission lines. The first excited states beginning with the H_g (273 cm^{-1}) fundamental have considerable population at 293°K and give rise to infrared-active “hot-band” transitions and a complicated spectrum. To get a spectrum of C_{60} comparable to what is shown for SF_6 one must cool the population to around 150°K . It is not too surprising then that the first high temperature scans of gas phase natural abundance C_{60} were complex and beyond easy assignment of rotational structure. An example of an Fourier transform scan by Frum et. al.⁵ is shown in Figure 4.2, where the band widths found around the T_{1u} fundamentals at 530 , 570 , 1170 , and 1410 cm^{-1} are seen to be consistent with predicted scalar coriolis constants.⁶ This provides encouragement for

future experiments at higher resolution using gas having greater isotopic purity and putting the molecules through expansion to get lower temperatures.

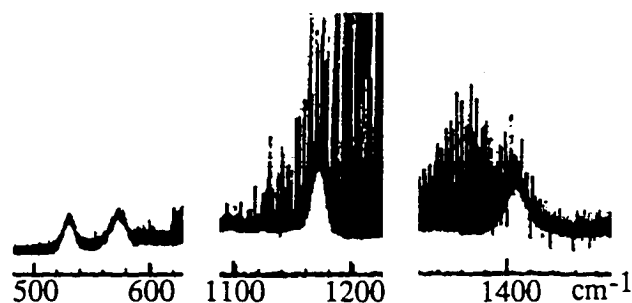


Figure 4.2 Fourier transform emission spectra of the four T_{1u} vibrational modes of C_{60} .⁵

Sketches of hypothetical infrared rovibrational spectra for a fundamental ($0 \rightarrow 1$) transition for one of the four T_1 -type modes are given in figure 4.3. The P and R branches of the $^{12}C_{60}$ spectrum around the Q branch show the gaps that result from the Pauli exclusion principle. Only lines R(0), R(6), R(10), R(12), R(15), , R(28) (or P(6), P(10), P(12), P(15), , P(28)) can appear. The notation R(J) means rotational momentum is raised from J to J + 1 in the transition while P(J) means reduces from J to J - 1. So each R(J) and P(J) line reflects the ground state J population. The Boltzmann factor is shown rising as it would near room temperature (300° K). However, if the molecules were cooled sufficiently ($\sim 10^\circ K$) the population could be concentrated into just the lowest allowed J values of 0, 6, 10, 12,.... Even a moderate cooling would also reduce hot band transitions arising from thermally excited vibrations and return population from these levels to the purely rotational levels.

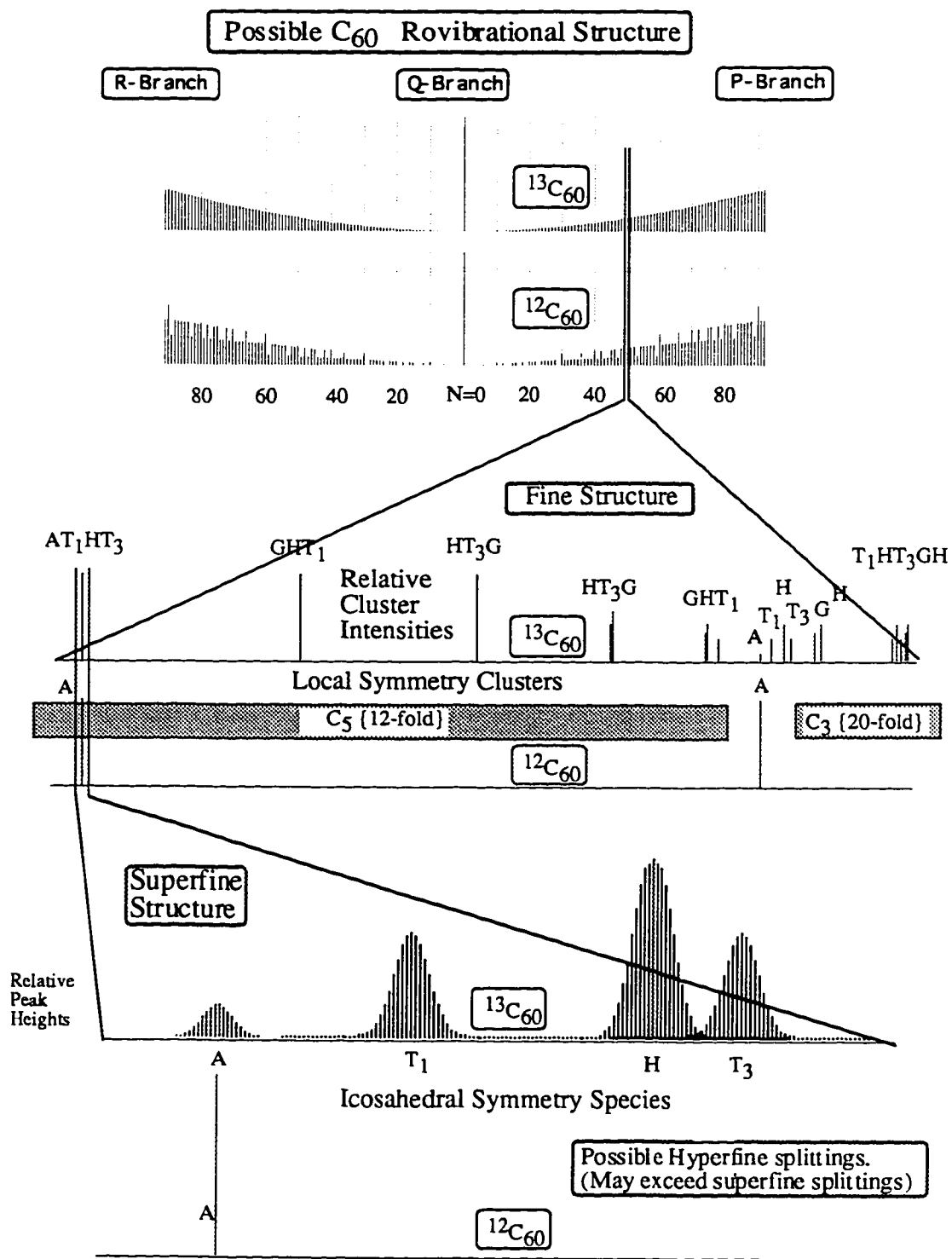


Figure 4.3 Theoretical spectra at various levels of resolution for $^{12}C_{60}$ and $^{13}C_{60}$.

An example of a hypothetical $J = 50$ level splitting for $C_{60} P(50)$ is sketched in Figure 4.3. The icosahedral rotational Hamiltonian can once more be modeled by expanding in terms of irreducible multipole tensors and omit all terms greater than sixth rank. Symmetry eliminates those on non-zero rank less than six.

$$H = B|J|^2 + t_{066} \left(\frac{\sqrt{11}}{5} T_0^6 + \frac{\sqrt{7}}{5} (T_5^6 - T_{-5}^6) \right) \quad (4.4)$$

Based on this lowest order model one predicts spectral structure such as is displayed in the lower half of Figure 4.3. At the extreme left hand side of Figure 4.3 there is a magnified view of a 0_5 cluster of icosahedral species A, T_1, H, T_3 which together would contain twelve ($1 + 3 + 5 + 3 = 12$) rotational sublevels if they were Bose or Pauli-allowed as they are in $^{13}C_{60}$.

Each cluster in figure 4.3 is labeled by an approximate quantum number k_5 or k_3 . This is related to the azimuthal component of the angular momentum quantized with respect to body axes of five-fold (C_5) or three-fold (C_3) local symmetry respectively. The leftmost cluster correspond to states with rotational quanta of $K = 50$ around one of the twelve C_5 symmetry axes and are labeled 0_5 since $50 \bmod 5 = 0$. The neighboring 4_5 cluster corresponds to twelve nearly degenerate states of $K=49 \bmod 5=4_5$ and similarly for $1_5, 2_5,$ and 3_5 . At the extreme right hand side is a cluster of states with $K=50 \bmod 3=2_3$ which is better described by C_3 symmetry. It corresponds to an angular momentum of $K=50$ around C_3 axes, and is labeled 2_3 since $50 \bmod 3=2_3$. It contains twenty rotational sublevels, exactly the number of C_3 axes in C_{60} , distributed amongst the Y-species $T_1, H, T_3, G,$ and H . The qualitative species ordering and clustering of levels and clusters may be found using figure 4.4. However, 2_3 ($K = 50$) and 1_3 ($K = 49$) clusters in the $J = 50$ manifold are Bose-excluded for $^{12}C_{60}$.

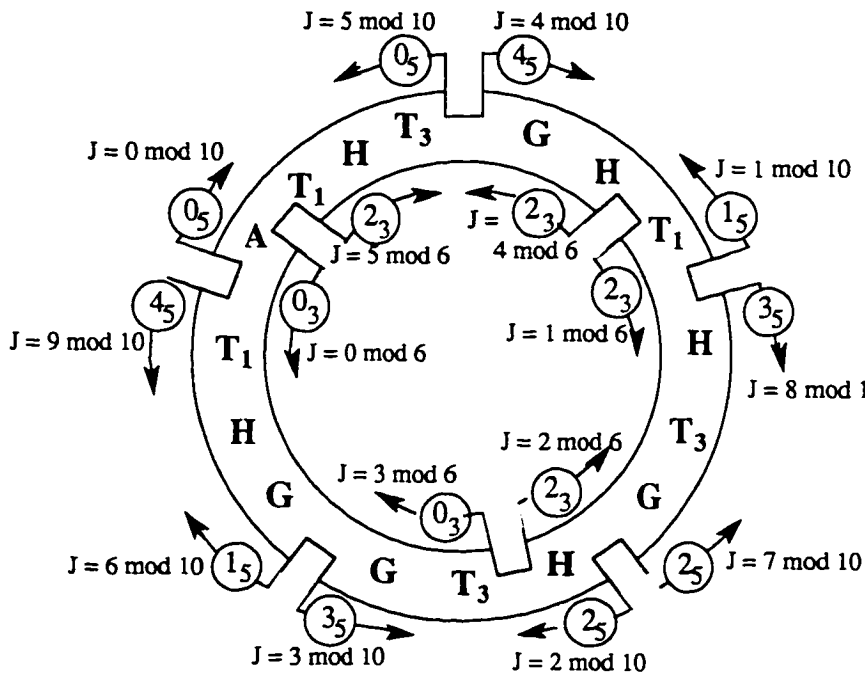


Figure 4.4
Sequencing ring for icosahedral symmetry species in sixth-rank tensor spectrum for integral angular momentum J .

For $^{12}\text{C}_{60}$ only the A sublevel is allowed. The next cluster to the right is labeled 4_5 and also has twelve levels but different symmetry species G , H , and T_1 . However, all of these are Pauli-excluded in a $^{12}\text{C}_{60}$ spectrum.

For $^{12}\text{C}_{60}$ all clusters are empty except those of 0_3 or 0_5 symmetry which contain a single A -line. The A -line sits where it would have been if all the other species were present. The $J = 50$ example has only two such lines. The other ninety-nine substates are excluded. The second A species line lies in the separatrix region between the C_5 and C_3 cluster ladders. This peak is indicated in the lower center portion on the right hand side of figure 4.3. Directly above it is an A -line in the corresponding spectrum of $^{13}\text{C}_{60}$ which is discussed later. Each A -line in the $^{12}\text{C}_{60}$ spectrum has sixty times the intensity it would have had if all species were Bose-allowed.

Indeed it may seem futile to discuss level clusters for $^{12}\text{C}_{60}$ in which practically all the states are missing. However, the physical properties of the rotational wavefunctions for the allowed states in $^{12}\text{C}_{60}$ would be identical to the corresponding ones in $^{13}\text{C}_{60}$. The difference is that the $^{13}\text{C}_{60}$ spectrum has all the species needed to make a complete superfine structure and this gives a direct measurement of the localization of the corresponding rotational states. For example, the small A-line for $^{13}\text{C}_{60}$ is one of several lines between the C_5 and C_3 bands and lies directly above an isolated A-line for $^{12}\text{C}_{60}$ in figure 4.3. The $^{13}\text{C}_{60}$ A-line clearly falls in a region where lines are not clustering. It is clearly distinguished from the first A-line in $^{13}\text{C}_{60}$ which is clustered with eleven other states. By contrast the $^{12}\text{C}_{60}$ spectrum has just two A-lines and no obvious way to distinguish them.

Each A-line in the $^{12}\text{C}_{60}$ spectrum belongs to a totally symmetric nuclear spin-0 state which is the only state sixty spinless nuclei can make. All the nuclear angular momentum in $^{12}\text{C}_{60}$ comes from rotational or vibrational motion of the nuclei. It should be noted that fluorine has no long lived spin zero isotopes, therefore no comparisons will be drawn between $^{12}\text{C}_{60}$ and SF_6 . SF_6 is more like $^{13}\text{C}_{60}$ in this respect since it has spin 1/2 nuclei, albeit, $^{13}\text{C}_{60}$ has 10 times as many .

Permutational Analysis

Sixty spin-1/2 nuclei yield an enormous number ($2^{60} \cong 1.2 \times 10^{18}$) of spin states. By comparison, the analogous SF_6 molecule has only $2^6 = 64$ spin states, and SiF_4 has only 16. Each $^{13}\text{C}_{60}$ nuclear spin state can have one of thirty-one different values of total nuclear spin quanta ranging from $I = 0$ to $I = 30$. The $^{13}\text{C}_{60}$ molecule may therefore have remarkably large nuclear spin I as well as large rotor momentum R . A given spin state is associated with an orbital or rotational state of definite icosahedral symmetry

species A , T_1 , T_3 , G , or H if and only if the resulting product makes a Pauli-allowed state that is totally antisymmetric to permutations of the sixty ^{13}C nuclei. While icosahedral symmetry Y is formidable compared to most molecular point groups it is tiny compared to the overlying permutational symmetry S_{60} of C_{60} which has $60!$ elements, or approximately 8.32×10^{81} permutations.

Fortunately, the mathematics of permutation symmetry and the related unitary groups contains some powerful computational methods. Various formulas based upon Young frames or tableaux make it relatively easy to compute characters and irreducible representations of large symmetric and unitary groups^{7,8,9}. These techniques originally applied to molecular electronic orbitals were later applied to molecular nuclear spin states and statistical weight computations.¹⁰ Here Coleman's character formula is used to compute S_{60} characters for icosahedral classes in order to deduce the $S_{60} \supset Y$ correlation table. This is analogous to the S_6 permutational analysis of SF_6 given in references 7b and 7c.

Young tableaux provide a powerful symbolic technique for labeling the class structure for the spin space of a fixed number of identical nuclei having a given intrinsic nuclear spin. Tableaux arranged in horizontal rows correspond to symmetric combinations, and columns represent antisymmetrized combinations. A specific S_n species or tableau is characterized by the size of the rows when ordered from largest to smallest. For example, the totally symmetric species of S_3 is labeled $\begin{array}{|c|c|c|} \hline \square & \square & \square \\ \hline \end{array}$ or $[3]$ and the antisymmetric species is $\begin{array}{|c|} \hline \square \\ \hline \end{array}$ or $[1,1,1]=[1^3]$. In the preceding, the tableaux are also represented by brackets which contain the number in each of the partitioned rows. The Pauli principle is incorporated for $I = 1/2$ nuclei by restricting the number of rows to $2I+1$. For example, NH_3 is a system of three spin- $1/2$ nuclei in a C_{3v} orbital configuration. S_3 is isomorphic to C_{3v} therefore the orbital states correlate with the S_3

orbital tableaus in a simple one to one fashion, $A_1 \sim \square\square\square$, $A_2 \sim \begin{matrix} \square \\ \square \\ \square \end{matrix}$, and $E \sim \begin{matrix} \square & \square \\ \square & \square \end{matrix}$. When considered as spin-tableaus $\square\square\square$ relates to $I_{\text{total}}=3/2$ spin species, $\begin{matrix} \square \\ \square \\ \square \end{matrix}$ exceeds the $2(1/2)+1 = 2$ limit on columns and is not allowed, and $\begin{matrix} \square & \square \\ \square & \square \end{matrix}$ relates to the $I_{\text{total}} = 1/2$ spin species. Summing the correlation frequencies over the degeneracies l^α of C_{3v} species and the degeneracies $f^{[n_1, n_2, n_3]}$ of the allowed S_3 species all 2^3 of the spin states are represented.

$$2^3 = \sum_{\alpha \in \{A_1, E\}} \left(\sum_{[n_1, n_2] \in \{[3], [2, 1]\}} l^\alpha f^{[n_1, n_2]} \right)$$

This provides a way to check the counting.

Spin-Permutation Symmetry of $^{13}\text{C}_{60}$

An allowed $^{13}\text{C}_{60}$ spin-1/2 tableau $[\mu_1, \mu_2]$ will have sixty boxes each containing spin up or spin down according to the value of each individual nuclear spin. Each tableau has μ_1 -boxes in its first row and μ_2 -boxes in its second which is always less than or equal to the length of the first row ($\mu_1 \geq \mu_2$). The sum of the row lengths is the number of boxes or the number of nuclei which is sixty ($\mu_1 + \mu_2 = 60$). Each box in the second row corresponds to an antisymmetrized pair involving itself and the one above so there are μ_2 scalar pairs in a $[\mu_1, \mu_2]$ tableau state. The remaining $(\mu_1 - \mu_2)$ boxes represent unpaired nuclei that can each contribute 1/2 to the total nuclear spin I of the $[\mu_1, \mu_2]$ -tableau state.

$$I = (\mu_1 - \mu_2)/2 > 0, \text{ where } \mu_1 + \mu_2 = 60 \quad (4.5)$$

The preceding equations determine which total nuclear spin quanta $I = 0, 1, \dots, 29, 30$ belong to each of 31 allowed tableaus.

Standard group character analysis is used to relate the Y_h species to those of S_{60} . The characters of both groups are tabulated for representative operators of each of the 10 Y_h all commuting classes.

$$\begin{aligned}
 C_1 &= \{\mathbf{1}\} \\
 C_R &= \{\mathbf{R}_1 + \dots + \mathbf{R}_6 + \mathbf{R}_1^4 + \dots + \mathbf{R}_6^4\} \\
 C_{R^2} &= \{\mathbf{R}_1^2 + \dots + \mathbf{R}_6^2 + \mathbf{R}_1^3 + \dots + \mathbf{R}_6^3\} \\
 C_r &= \{\mathbf{r}_1 + \dots + \mathbf{r}_{10} + \mathbf{r}_1^2 + \dots + \mathbf{r}_{10}^2\} \\
 C_i &= \{\mathbf{i}_1 + \dots + \mathbf{i}_{15}\} \\
 C_I &= \mathbf{I}C_1 \\
 C_{IR} &= \mathbf{I}C_R \\
 C_{IR^2} &= \mathbf{I}C_{R^2} \\
 C_{Ir} &= \mathbf{I}C_r \\
 C_{Ii} &= \mathbf{I}C_i
 \end{aligned} \tag{4.6}$$

In equations 4.6, $\mathbf{1}$ is the identity, \mathbf{R}_m^n represents an n times 72° rotation about the m^{th} axis, \mathbf{r}_m^n stands for an n times 120° rotation about the m^{th} axis, \mathbf{i}_m is a 180° operation about the m^{th} axis, and \mathbf{I} is the inversion operator. The S_{60} permutational cycle structure $\{\alpha_1 \alpha_2 \dots\}$ of these icosahedral classes depends upon how a C_{60} symmetry operation permutes the nuclei. α_1 is the number of nuclei that are unchanged. α_2 is the number of pairs of nuclei transposed into each others' locations, and so forth. For example, a 120° rotation of C_{60} has twenty 3-cycles. The cycle structure for representatives of the above classes are given in 4.7.

$$\begin{aligned}
\mathbf{1} &\approx \{1^{60}\} \\
\mathbf{R}, \mathbf{R}^2, \mathbf{R}^3, \mathbf{R}^4 &\approx \{5^{12}\} \\
\mathbf{r}, \mathbf{r}^2 &\approx \{3^{20}\} \\
\mathbf{i}, \mathbf{I} &\approx \{2^{30}\} \\
\mathbf{IR}, \mathbf{IR}^2, \mathbf{IR}^3, \mathbf{IR}^4 &\approx \{10^6\} \\
\mathbf{Ir}, \mathbf{Ir}^2 &\approx \{6^{10}\} \\
\mathbf{Ii} &\approx \{1^4, 2^{28}\}
\end{aligned} \tag{4.7}$$

The Coleman formula is then used to compute characters for these operations. Appendix D lists the S_{60} characters for Y operations in the same order as the Y_h classes in equations 4.6. The correlation frequencies $f^{\rho}[\mu_1, \mu_2]$ of each icosahedral species ρ for a given tableau $[\mu_1, \mu_2]$ representation of S_{60} is calculated using the characters in tables 2.3 and appendix D with the frequency relation 4.8.

$$f^{\rho}[\mu_1, \mu_2] = \frac{1}{\chi(Y_h)} \sum_{\alpha} \chi_{\alpha}^{\rho} \chi_{\alpha_1, \alpha_2, \dots}^{[\mu_1, \mu_2]} \tag{4.8}$$

α_i is the cycle structure in equation 4.7 and α is the equivalent rotational operation. The Y_h frequencies are given in appendix E in terms S_{60} species labeled by total nuclear spin I.

Each column of appendix E gives the number of allowed spin species belonging to a particular icosahedral orbital symmetry species ρ . Note that in this format antisymmetric products result in a parity change. For example, $\rho = A$ correlates with just one $[60,0]$ permutation species of positive parity, therefore switching parity gives A_u as the sole antisymmetric orbital species. Neither A_g nor A_u has an (I = 29) multiplet but

they have 14 and 22 ($I = 28$) multiplets, respectively. The other icosahedral species fail to produce any ($I = 30$)-multiplets but have several belonging to $I = 29$ and several hundred belonging to $I = 28$.

For nuclear spin values below $I = 27$ or 28 the number of possible spin states belonging to each icosahedral orbital species increases exponentially. It exceeds ten trillion states for each of the species with $I = 10$. Then the numbers of states begin to level off and attain a maximum value of about seven hundred and fifty trillion for H_u or H_g species having nuclear spin $I = 3$ and 4 . The number of H_u or H_g states with $I = 2, 1,$ and 0 are, respectively, about six hundred and fifty trillion, four hundred and fifty trillion, and one hundred and fifty trillion. By comparison, there are only a handful (a few hundred billion) of states with $I = 16$ or greater. They probably will be difficult to see if all states are evenly populated.

The spectral profile belonging to a given species consists of a nearly binomial distribution of hyperfine lines as those sketched in figure 4.3. Hyperfine states having a given I value will contribute $2I + 1$ spectral components split more or less evenly around the center of each distribution. The lowest I values ($I < 10$) account for the bulk of the total line intensity. Greater I values correspond to hyperfine components split across a wider range, but there are fewer of them. In figure 4.3 we are assuming the simplest case in which the superfine splitting is large enough to resolve features belonging to individual icosahedral rotor species $A, T_1, T_3, G,$ or H . (This is called hyperfine case (1) in Reference 18a.) The hyperfine components are grouped into equally spaced lines as they would appear if split by the scalar spin rotation interaction.

$$\mathbf{H}_{\text{srs}} = \sigma \bar{\mathbf{I}} \cdot \bar{\mathbf{J}} \quad (4.9)$$

The height of a line located I spaces from the center of the bell shaped A -pattern is proportional to the sum of numbers in the A -column of appendix E belonging to all spins less than or equal to I . The center line height is the sum of the entire column. The T_1 , T_3 , G , or H hyperfine patterns are plotted in a like fashion.

If individual icosahedral multiplet patterns can be resolved they will have an identifiable set of relative intensities as indicated in figure 4.3. Each spin component and the sums thereof will contribute intensity in approximately the ratio 1:3:3:4:5 for species A , T_1 , T_3 , G , and H , respectively. This is true for either parity g or u . This ratio is closely followed by numbers in the rows of appendix E below $I = 24$ or 25 . This approximation becomes better as I decreases but breaks down completely for the highest values of $I = 30, 29$, or 28 . However, the latter only account for a few hundred states.

Indeed, it is extraordinary to have nuclear spin weights that mirror the rotational degeneracies of the molecular symmetry. This is not the case in most other high symmetry molecules such as SF_6 . The extraordinary weights occur because most of the allowed C_{60} nuclear spin states belong to a regular representation of icosahedral symmetry for which the repetition number of each irreducible representation is equal to its dimension. A regular representation is the primitive induced representation induced by the unit subgroup C_1 . It describes the symmetry of most of the primitive spin states since each nucleus sits on a site of C_1 symmetry. The rare spin arrangements which have higher symmetry and belong to a smaller induced representation give differing ratios for species A , T_1 , T_3 , G , and H . However, from appendix E it is evident that these special spin states represent less than one in a hundred thousand. Such small discrepancies are probably well below the error of experimental intensity measurements. They would require the very highest resolution studies of individual components of hyperfine structure in the wings of the distributions.

Since most of the nuclear spin multiplets $I = 0, 1, 2, \dots$ contain icosahedral species $\{A, T_1, T_3, G, H\}$ according to the regular ratio of 1:3:3:4:5 it follows that any sum over I does also. The total nuclear spin weights according to Y_h species are tabulated below.

A_g	9.607679885269312000e+15
T_{1g}	2.882303697092649600e+16
T_{3g}	2.882303697092649600e+16
G_g	3.843071685619372800e+16
H_g	4.803839674093824000e+16
A_u	9.607678793631424000e+15
T_{1u}	2.882303799098121600e+16
T_{3u}	2.882303799098121600e+16
G_u	3.843071678461062400e+16
H_u	4.803839557771827200e+16

Table 4.2 Statistical weights for Y_h species of $^{13}\text{C}_{60}$.

It is interesting to note that the often asserted claim that all species occur in parity pairs is supported only in the leading 8 digits, but as evinced in the absent resonance peaks in the high resolution spectra of SF_6 ^{11,12}, the claim proves erroneous for C_{60} as well. Also, it is interesting to note that the T_1 and T_3 statistical weights of like parity are equal. This is a consequence of the irrational conjugant nature $\{\pm(1 \pm \sqrt{5})/2\}$ of the Y_h characters (Table 2.3) for the n times 72° operations. Since all S_{60} characters in appendix D are integers, any correlation with one of the T species must include the other three fold degenerate partner as well.

Heretofore the simplest case (case 1) has been assumed in which each icosahedral species $\{A, T_1, T_3, G, H\}$ is a good quantum label of the rotational fine structure and total nuclear spin $\{I = 0, 1, \dots, 30\}$ is a good quantum for hyperfine structure. This neglects the inevitable level structure that arises when the rotational quantum number R or N is high. Then the superfine splitting becomes much smaller than the hyperfine splitting and

allows different species and I-states in a cluster to mix strongly through scalar and tensor spin-rotation interactions which otherwise would have lesser effects.

Superhyperfine Structure

The case in which nuclear spin and rotational states mix will be referred to as case 2. The transition between case 1 and case 2 is analogous in some ways to the transition between LS coupling and jj coupling in shell theory. Breakdown of superfine and hyperfine structure into superhyperfine patterns has been identified in the very highest resolution spectra of SF₆¹² and recently for T_d symmetric ²⁸SiF₄¹³. Figure 4.5 illustrates the evolution to case 2 clusters as the tunneling parameter S becomes negligible.

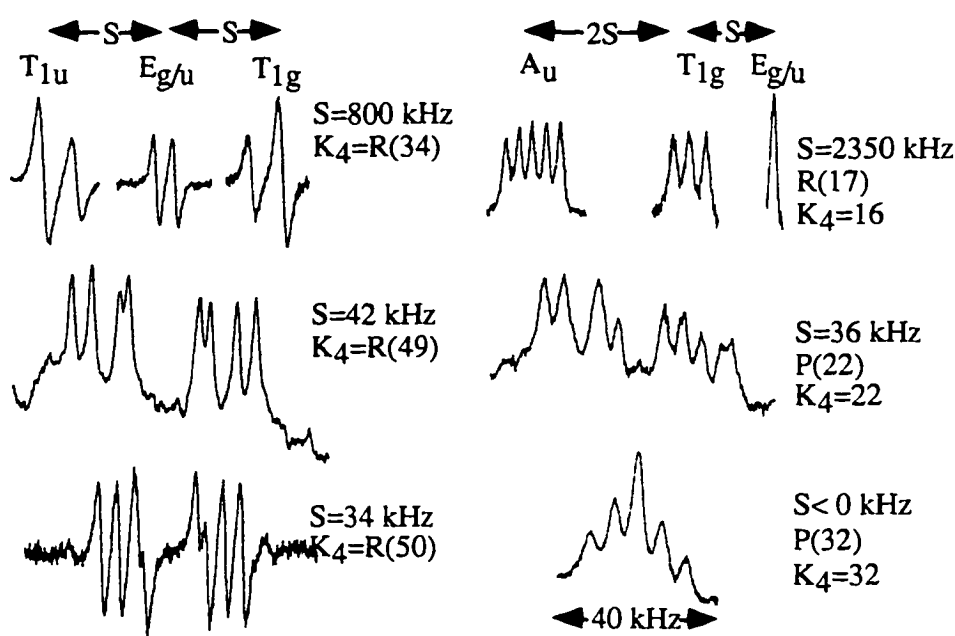


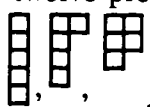
Figure 4.5 ²⁸SiF₆ Superhyperfine clusters. ±₁₃ at left and 0₄ and 2₄ clusters at right.

In the left hand cases, the C_3 symmetry axes becomes a permanent axis of rotation and the T_d global symmetry reduces to C_{3v} . For the right hand cases, the C_2 symmetry axes becomes a permanent axis of rotation and the global symmetry reduces to C_{2s} . These are two examples of spontaneous symmetry breaking.

When rotational symmetry is broken the effective or "feasible" permutational symmetry is reduced, as well. Previously equivalent nuclear positions become distinguished by their positions relative to the rotational axis. Rotationally induced "chemical shifts" split the hyperfine spectra into patterns that are analogous to NMR patterns. As the spin rotation interaction becomes dominant the bell distributions of the intracluster Y species widen to the point where they stack superimposed to form one nearly Binomial distribution.

Spontaneous Symmetry Breaking on C_5 Axis

For $^{13}C_{60}$ there are three types of cyclic axes that may become preferred, namely the C_2 , C_3 and the C_5 axes. As an example of C_{5v} spontaneous symmetry breaking, figure 4.6 illustrates a case $2 O_5$ superhyperfine cluster. At the bottom of this figure is an isometric projection of Buckyball with the locally restricted axis of rotation centered vertically through the 5-fold axis. The original 60 indistinguishable nuclei are now identifiable with respect to their distance from the axis of rotation. The broken permutation symmetry would then belong to the direct product of twelve S_5 groups (abbreviated $^{12} \otimes S_5$). In figure 4.8 equivalent nuclei are shaded and associated with a given term in the above product space. Each of the twelve product groups will have

species chosen from the Pauli allowed orbital tableau . Since the O_5 clusters are the only twelve fold containing A type orbital species they will be the only ones with

$I_z = \pm 30$ peaks. Similarly, only the O_2 and O_3 clusters will have $I_z = \pm 30$ component in the other broken symmetry cases.

The Hamiltonian may be expanded in terms of interactions involving nuclear spin.

$$\mathbf{H} = \mathbf{H}_{so}^{ne} + \mathbf{H}_{sr}^{nn} + \mathbf{H}_{sv}^{nn} + \mathbf{H}_{ss}^{nn} \quad (4.10)$$

The principle terms being the interactions acting on a given nuclei due to the motion of the electrons, the rotation of the molecule, the vibration motion of the nuclei and lastly the interactions with the spin of the other nuclei.

$$\begin{aligned} \mathbf{H}_{so}^{ne} &= - \sum_{k,e} \bar{\mu}_k \cdot \bar{B}_e(\bar{r}_k) \\ \mathbf{H}_{sr}^{nn} &= - \sum_{k \neq j} \bar{\mu}_k \cdot \bar{B}_j(\bar{r}_k) \\ \mathbf{H}_{sv}^{nn} &= h\omega \bar{I} \cdot \bar{\ell} \\ \mathbf{H}_{ss}^{nn} &= \frac{\mu_o \mu_n^2}{4\pi} \sum_{k < j} \frac{g_k g_j}{r_{jk}^3} \left[\bar{I}_j \cdot \bar{I}_k - 3(\bar{I}_j \cdot \hat{r}_{jk})(\bar{I}_k \cdot \hat{r}_{jk}) \right] \end{aligned} \quad (4.11)$$

In figure 4.6, the vibrational ground state is assumed and the interaction strengths from highest to lowest are scalar spin-rotation, tensor spin-rotation and spin-spin. The spin-rotation splitting is determined by the magnetic field local to each nuclei. Therefore the nuclei furthest from the axis of rotation would tend to be perturbed to a greater extent than those that are closer. For negligible spin exchange effects, spontaneous symmetry breaking about a C_5 axis partitions the nuclei into four distinct local environments. Therefore, a single down spin would have four possible locations and the $I_z = 29$ cluster in figure 4.6 would be split into 4 components. The two down spins in the $I_z = 28$ cluster would have 10 distinct components and so on until all sites of a given environment are filled.

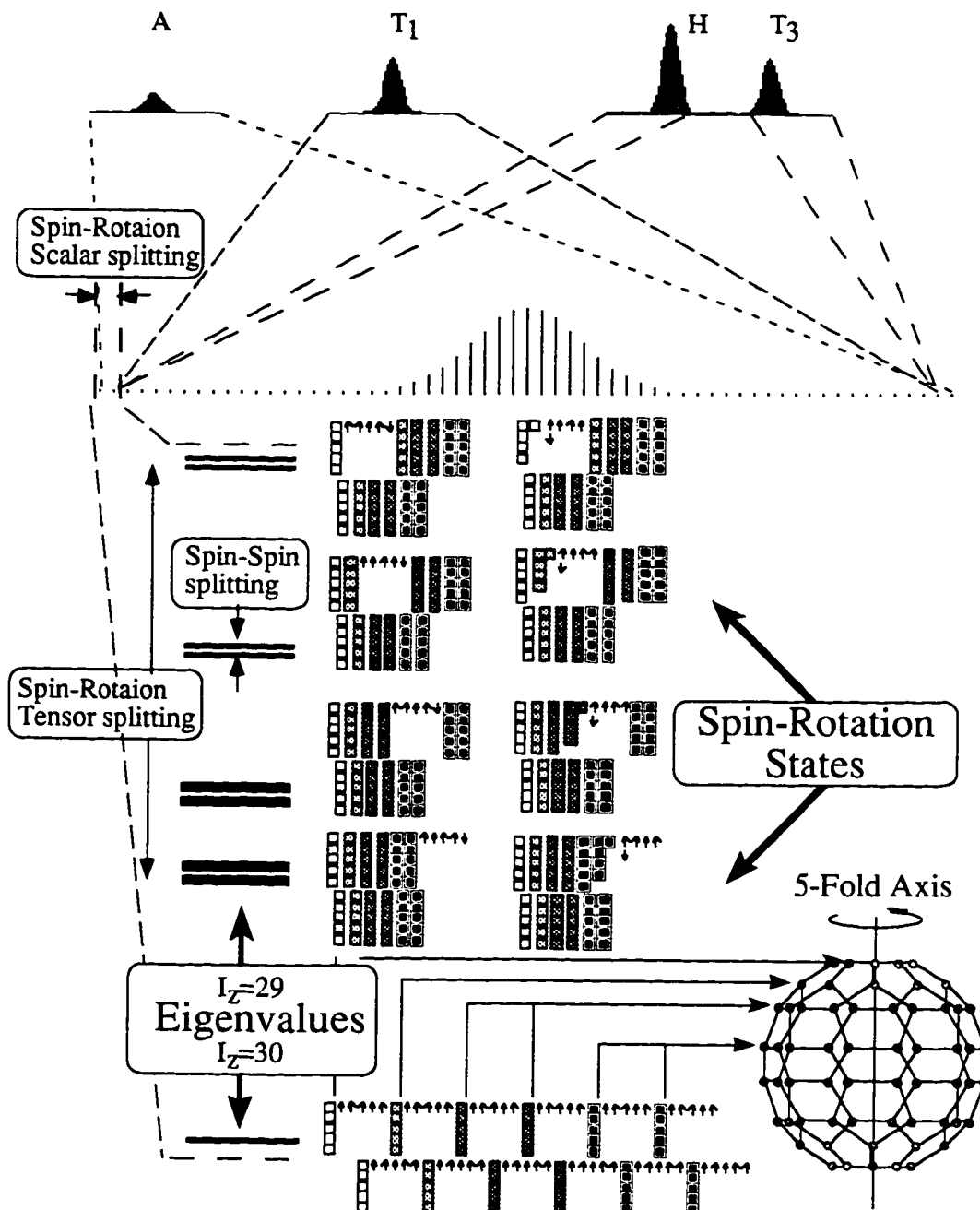


Figure 4.6 Hypothetical level structure for of a $^{13}\text{C}_{60} \text{O}_5$ superfine cluster (Case 1 at top and case 2 at bottom). The interaction strengths $H_{\text{SSR}} > H_{\text{ISR}} > H_{\text{SS}}$ are assumed for case two. Note only spin tableaux with down spins are labeled.

This pattern, namely the fourth diagonal in Pascal's triangle, would give the partitioning of the $O_5 I_z$ clusters up to $I_z=20$. Table 4.3 tabulates this partitioning of the I_z clusters for O_5 , O_3 , and O_2 case 2 clusters.

$\pm I_z$	C ₅ Axis			C ₃ Axis			C ₂ Axis		
30	1	1	1	1	1	1	1	1	1
29	1	2	3	4	5	6	7	8	9
28	1	3	6	10	15	21	28	36	45
27	1	4	10	20	35	56	84	120	165
26	1	5	15	35	70	126	210	330	495
25	1	6	21	56	126	252	462	792	1287
24	1	7	28	84	210	462	924	1716	3003
23	1	8	36	120	330	792	1716	3432	6435
22	1	9	45	165	495	1287	3003	6435	12870
21	1	10	55	220	715	2002	5005	11440	24310
20	1	11	66	286	1001	3003	8008	19448	43758

Table 4.3 Pascal's 'triangle' predicting partitioning of I_z clusters for tensor spin-rotation splitting with negligible spin-spin interaction.

Chapter 5 Rotation Energy Level Spectra for Half-integral Angular Momentum Icosahedral Molecules

Introduction

Mass spectroscopy observations by Curl and Smalley¹ and Kroto² of ionic C₆₀ clusters has stimulated considerable interest in icosahedrally symmetric "Buckminsterfullerene" structures. There is the related possibility that such highly symmetric ions and molecules occur in carbon-rich stellar nebulae and in some soot producing combustion processes. Also, the potential exists for spectroscopic studies of other icosahedrally symmetric structures such as C₂₀H₂₀, which was synthesized by Pacquete et. al.³, the borohydride ion B₁₂H₁₂⁻⁴ and a C₈₀ structure proposed by Chapman⁵.

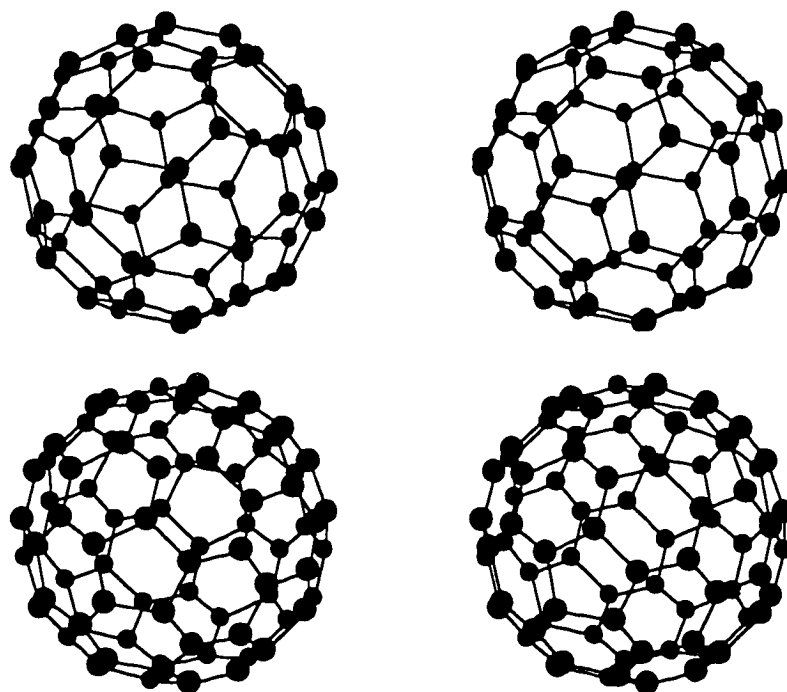


Figure 5.1 Stereoscopic views of C₆₀ (top) and C₈₀.

All this has increased our need to understand the spectroscopic consequences of this extraordinary symmetry, Y and its representations. The C_{80} structure is particularly intriguing since it is closely related to that of C_{60} ; as seen in figure 5.1 both are composed of interlocking pentagons and hexagons. Each carbon in the C_{60} structure sits in an identical environment of C_v symmetry while C_{80} contains twenty "extra" carbon atoms which sit at points of C_{3v} local symmetry.

It is possible that detailed spectroscopic investigation of these highly symmetric cage molecules will first be done using their positive or negative ions, which have lost or gained, respectively, a single electron. The mass spectroscopy⁶ which indicates the existence of C_{60}^+ , involves the positive ionic state, and it is well known that many large molecules form stable negative ions. Recent developments in ion trap technology and ion spectroscopy raises the possibility for identifying and investigating high resolution ionic spectra of these structures. However, the symmetry analysis of singly charged, ions is quite different from that of the molecules, which was treated in earlier studies.^{7,8} One must deal with half-integer angular momentum which has very different symmetry properties. For example, the uncoupled half-integer spin of the electron changes phase by a factor of -1 under a rotation of 2π . This necessitates the use of multiplier or ray representations of the symmetry algebra. Conventional treatments of finite symmetry and crystal field splitting use the faithful representations of the point double groups in the case of half integral J -values. For larger groups, such as the icosahedral group, it helps to reduce computational labor by using a ray algebra^{9,10}, in which the operations addition and subtraction are allowed. This has the effect of halving the size of the class algebra rather than doubling it. This symmetry analysis will be useful in analyzing combined spin-orbit-rotation and Jahn-Teller effects in icosahedral molecules with an odd number

of electrons. A recent paper by Ceulemans and Fowler¹¹ carried out an analysis of Jahn-Teller distortion for the fivefold degenerate state of a neutral icosahedral molecule.

Nevertheless, there are quite a number of similarities between the symmetry and spectral analysis of half-integral J values and that of integral J values, particularly for the high J limit. In the classical limit the distinction the two types is diminished. As will be shown here, many of the approximate semiclassical techniques developed to treat integral angular momentum fine structure in tensor spectra can also be applied to half-integral J.

In the past the analysis of ionic nonlinear molecular fundamentals has been well approximated by Hund's Case (a) in which the (integral) rotor momenta N or R were good quantum numbers for nearly-degenerate spin multiplets. It is not yet known if this applies to C₆₀ fundamentals. However, high resolution C₆₀ spectroscopy above 50° K is likely to require examination of rovibrational overtone structure which may have large N mixing. In any case one should be prepared to handle other Hund's cases and their intermediates which involve half-integral J labeling.

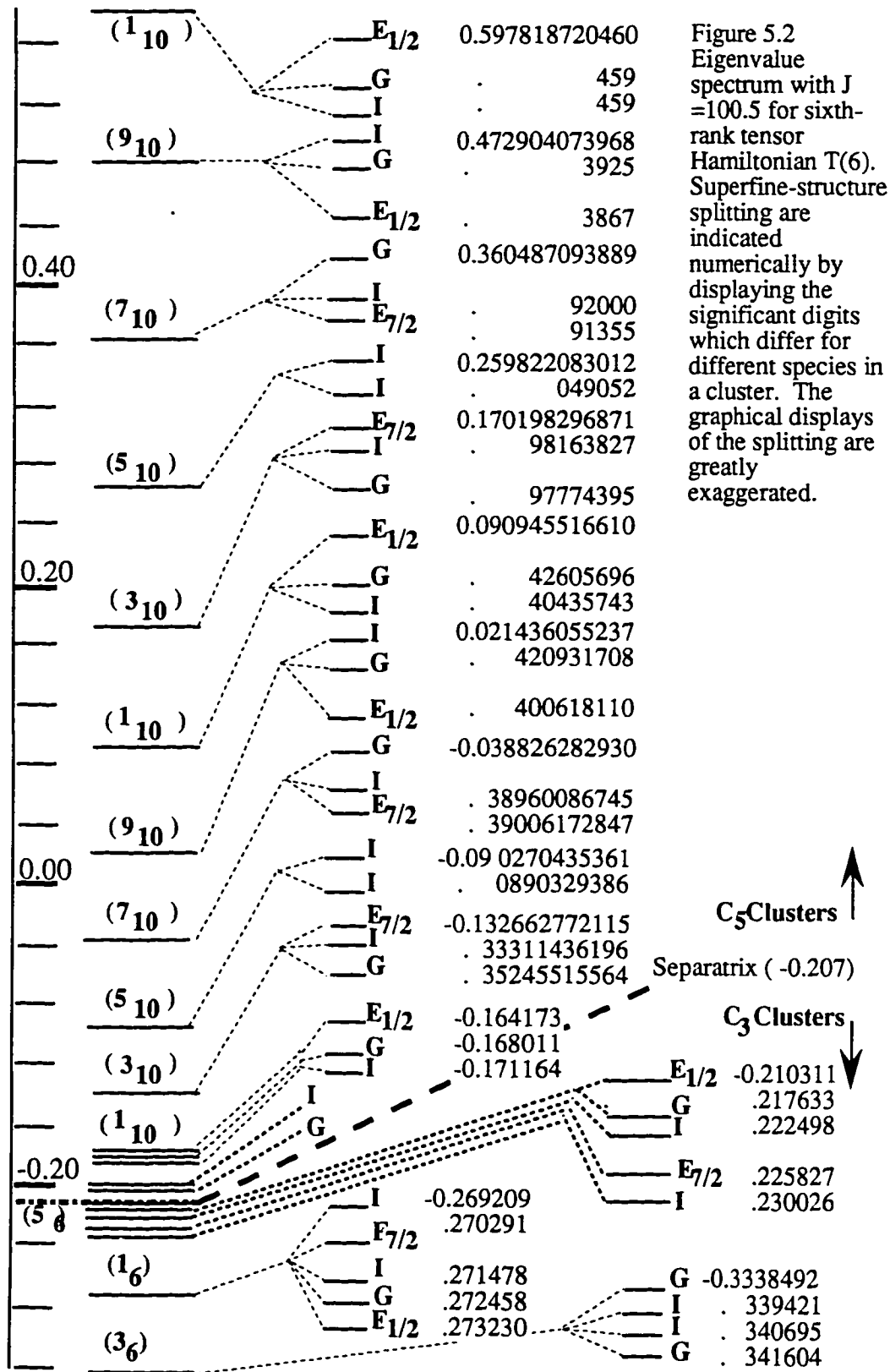
Fine Structure for Half Integral J

The icosahedral spectral patterns and analysis are similar but more complex than those seen in laser spectra of octahedral SF₆¹². Rotational fine structure is modeled by the eigenvalue spectrum of a symmetric tensor operator represented in a 2J+1 dimensional angular momentum basis. This tensor operator chosen to approximate the icosahedral rotational Hamiltonian is the same as equation 4.4.

$$\mathbf{H} = B|J|^2 + t_{066} \left(\frac{\sqrt{11}}{5} T_0^6 + \frac{\sqrt{7}}{5} (T_5^6 - T_{-5}^6) \right) \quad (5.1)$$

This operator will play the same role as Hecht's Hamiltonian did in the octahedral analysis.

To obtain numerical eigenlevels the sixth rank tensor is first represented by a $(2J+1 \times 2J+1)$ matrix in the total angular momentum basis, then numerically diagonalized. The algorithm used to find these eigenvalues is similar to that used in references [7,8] with modifications to allow half-integral J , index sorting, and a more precise diagonalization algorithm.^{13,14} High computational precision is needed to resolve the extraordinary level clustering which these high symmetry tensors yield. The $J = 100.5$ case is illustrated in figure 5.2. The bold letters following each level are icosahedral symmetry species labels for ray representations. *E* labels 2-fold degeneracies (There are two kinds labeled by correlations with the $SU(2)$ supergroup, $E_{1/2}$ and $E_{7/2}$), *G* labels 4-fold degeneracies, and *I* labels 6-fold degeneracies. None of these should be confused with any of the standard representations *A* (1-fold), T_1 or T_3 (3-fold), *G* (4-fold), or *H* (5-fold) discussed in chapters 3 and 4.



It is instructive to view the resultant energy level spectrum with the use of a rotational energy (RE) surface. This surface is a radial plot of the Hamiltonian in terms of the polar, and azimuthal coordinates of the classical J vector as viewed from the body frame of reference. For simplicity, the classical J vector is used to define the lab-fixed z-axis. The rotational energy is given by,

$$RE(\theta, \phi) = B|J|^2 + t_{066}T^{(6)}(\theta, \phi) \quad (5.2a)$$

where,

$$T^{(6)}(\theta, \phi) = \frac{\sqrt{11}}{80}|J|^6 \left(\begin{array}{l} (231 \cos^6(\theta) - 315 \cos^4(\theta) + 105 \cos^2(\theta) - 5) \\ -42 \cos(\theta) \sin^5(\theta) \cos(\phi) (16 \cos^4(\phi) - 20 \cos^2(\phi) + 5) \end{array} \right) \quad (5.2b)$$

The scalar rotational constant is taken to be unity, and the tensor coefficient is chosen as follows to give a clear graphical representation in figure 5.3.

$$B|J|^2 = 1$$

$$t_{066}|J|^6 = 0.2$$

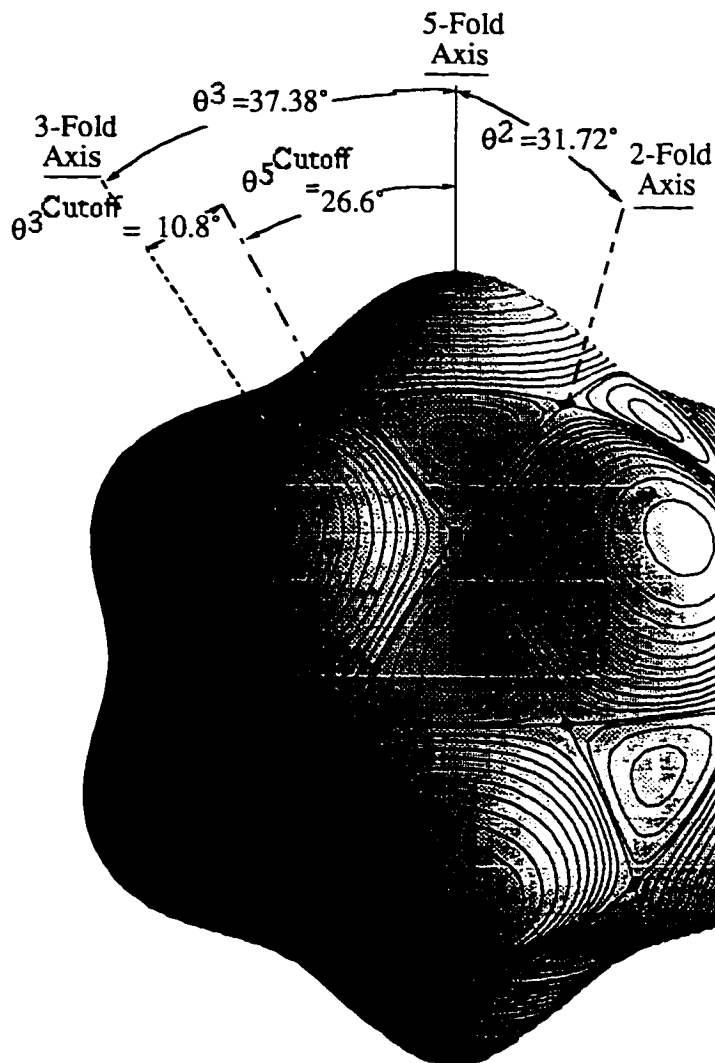


Figure 5.3 Rotational energy (RE) surface for the sixth-rank icosahedral tensor Hamiltonian. Trajectories or contours on the 12 fivefold symmetric hills correspond to clusters of 12 levels in figure 5.1, and the contours on the 20 threefold symmetry valleys correspond to the clusters of 20 levels below the separatrix. Angles between key symmetry axes can be used to compute limiting energy values for the two types of clustering. Constants are arbitrarily set to B , $|J| = 1.0$, and $t_{066} = 0.2$.

This surface is similar to the integral case except that quantizing level curves are shifted slightly to approximate half-integer J values. The level curves represent equal-energy level curves or classical trajectories of the precessing J vector. As seen, the trajectories become more circular in the neighborhood of the stable extrema of the RE surface. The bending of the circular trajectories arises from anisotropic centrifugal distortions the molecule undergoes while rotating. The eigenlevels in figure 5.2 can be related to quantizing level curves on the RE surface. Each set of twelve level curves for a given energy found on the twelve C_5 symmetric peaks corresponds to a 12-fold quasi-degenerate clusters. Similarly, each set of twenty levels in the C_3 symmetric valleys correspond to one of the 20-fold clusters. The separatrix in figure 5.3 consists of great arcs joining the C_2 symmetric saddle points on the RE surface. The polar angles for the C_2 , C_3 , C_5 axes can be substituted into (5.2) to determine bounds for the two types of quasi-degenerate clusters. These polar angles were determined to be $\theta_2=31.72^\circ$, $\phi_2=180^\circ$, $\theta_3=37.38^\circ$, $\phi_3=0^\circ$, $\theta_5=0^\circ$, $\phi_5=0^\circ$ where the subscript denotes the local symmetry for that axis. Using equation 5.2, the critical angles have the associated energies,

$$\begin{aligned}
 RE(\theta_2, \phi_2) &= -0.207 \\
 RE(\theta_3, \phi_3) &= -0.36 \\
 RE(\theta_5, \phi_5) &= 0.66
 \end{aligned}
 \tag{5.3}$$

These extreme values do indeed bracket all of the energies in figure 5.1, and as J increases in magnitude the highest cluster approaches the 0.66 limit while the lowest approaches the -0.36 limit. (Table 5.1) Also, the separatrix value accurately locates the energy region in which the 20-fold clusters blend into the higher energy 12-fold clusters.

There are several methods that can be used to approximate clusters centroids within each of the bracketed regions. The crudest utilizes a semi-classical approximation,

which is an approximation to the first order perturbation correction. The large- J asymptotic limit of the Wigner- Eckart coupling coefficient is used as follows,

$$\left\langle \frac{J}{K} \left| T_{\frac{K}{K}}^J \right| \frac{J}{K} \right\rangle \approx D_{00}^r(\theta_K^J) |J|^r = P_r(\cos(\theta_K^J)) |J|^r \quad J \gg 1 \quad (5.4)$$

where θ_K^J is the polar angle of the classical angular momentum J with J_z quantized by K and r is the rank of the tensor operator T . These approximate centroid values and the exact diagonalization values agree to within three significant places for the $J = K = 200.5$ case (Table 5.1), with a steady decrease in accuracy for lower K . The first order perturbation, containing only the diagonal terms of the Hamiltonian matrix, can be written in terms of Clebsh-Gordon coefficients.

$$H^{(1)}(K) \approx \frac{\sqrt{11}}{5} t_{066} \left\langle \frac{J}{K} \left| T_0^6 \right| \frac{J}{K} \right\rangle = \frac{\sqrt{11}}{5} t_{066} C_{0KK}^{6JJ} \quad (5.5)$$

In equation 5.5, as in the entirety of this discussion, the reduced matrix element has been set to unity. This is seen to agree with the exact values to seven significant digits for the $J = K = 200.5$ case. The second order terms containing the Hamiltonian matrix elements that lie five steps off the diagonal give a second order approximation.

$$H^{(2)}(K) \approx H^{(1)}(K) + \frac{|V_5(-K)|^2}{H^{(1)}(K) - H^{(1)}(K+5)} + \frac{|V_5(K)|^2}{H^{(1)}(K) - H^{(1)}(K-5)} \quad (5.6)$$

$H^{(1)}$ is given in equation 5.5, and the V_5 terms are given by the following.

$$V_5(K) = \frac{\sqrt{7}}{5} t_{066} \left\langle \frac{J}{K-5} \left| T_{-5}^6 \right| \frac{J}{K} \right\rangle = \frac{\sqrt{7}}{5} t_{066} C_{-5 \ K \ K-5}^{6 \ J \ J} \quad (5.7)$$

J=200.5				
<u>K</u>	<u>Exact values</u>	<u>Cone values</u>	<u>First order</u>	<u>Second order</u>
200.5	0.629561772569	0.629144432233	0.629561744701	0.629561772569
199.5	0.563622781797	0.563232090350	0.563622609345	0.563622781793
198.5	0.500981053974	0.500615644188	0.500980430758	0.500981053947
197.5	0.441537770448	0.441195965437	0.441536052344	0.441537770322
196.5	0.385196187831	0.384875793810	0.385192186037	0.385196187350
195.5	0.331861660933	0.331559716344	0.331853391592	0.331861659355
J=150.5				
150.5	0.618763657744	0.618031954648	0.618763567641	0.618763657742
149.5	0.532425029442	0.531755226480	0.532424465179	0.532425029407
148.5	0.451843368808	0.451231150772	0.451841302882	0.451843368565
147.5	0.376788850427	0.376228836722	0.376783073117	0.376788849207
146.5	0.307038251391	0.306523204709	0.307024582202	0.307038246440
145.5	0.242375110328	0.241894900198	0.242346364274	0.242375093002
J=100.5				
100.5	0.5978187205	0.5962171055	0.5978182423	0.5978187204
99.5	0.4729040739	0.4715029465	0.4729009976	0.4729040731
98.5	0.3604870925	0.3592645113	0.3604754774	0.3604870860
97.5	0.2598220660	0.2587493827	0.2597884119	0.2598220287
96.5	0.1701980562	0.1692336460	0.1701150641	0.1701978778
95.5	0.0909420059	0.0900212525	0.0907585929	0.0909412463
J=50.5				
50.5	0.5398333605	0.5339224224	0.5398244031	0.5398333446
49.5	0.3154076597	0.3109017588	0.3153429681	0.3154072912
48.5	0.1360451200	0.1325496207	0.1357578202	0.1360398296
47.5	-0.0033251007	-0.0065517157	-0.0043730150	-0.0033632177
46.5	-0.1067465342	-0.1114052380	-0.1100750339	-0.1066062392
45.5	-0.2003904126	-0.1866180124	-0.1859761472	-0.1712930784

Table 5.1 Comparison of exact cluster centroids and approximations for C_5 clusters for various half-integral J .

This approximates the exact values for the centroid of the clusters to within 12 significant digits for the case: $J = 200.5$ and $K = 200.5$. The clusters have the same 12 and 20-fold order of quasi-degeneracy that occurred for integer- J levels.^{7,8} However, the underlying superfine structure must be different since the ray-representations have degeneracies of order 2, 4, or 6 instead of 1, 3, 4, or 5.

Symmetry Analysis of Fine and Superfine Structure

The conventional double group treatment of half integral J would involve double the number of rotational operators in Y and this effectively quadruples the computational labor. Much of this labor can be eliminated by using a group algebra of $Y^{9,10}$ over the complex field as opposed to the $Y^{(d)}$ -double group. The algebra permits the use of plus and minus operators ($\pm g$) without increasing the dimension of the operator space. The operators will be labeled similar to that used in chapter 2. Rotations that are multiples of 72° are assigned an upper case 'R', rotations that are multiples of 120° labeled by a lower case 'r', rotations divisible by 180° are labeled 'i', and those divisible by 360° are labeled '1'. There are six two sided C_5 axes, corresponding to six rotations R_1, \dots, R_6 respectively. Similarly, the ten C_3 axes are associated with rotations r_1, \dots, r_{10} , and the fifteen C_2 axial rotations are i_1, \dots, i_{15} . However, the individual operators are now assigned a plus sign to denote a counter-clockwise rotation of less than 360° , and a minus sign for a clockwise rotation of less than or equal to 360° . A final integer again serves as a power or exponent to indicate the number of the fundamental rotations in each operator. For example, R_{1+3} is a rotation about the R_1 axis by $3 \times 72^\circ$ in the counter-clockwise direction. With this formalism, a R_{1+1} and its $360+72^\circ$ counterpart R_{1-1} , differ only by a -1 phase factor ($R_{1-1} = - (R_{1+1})$). Note that the inverse in $Y^{(d)}$ of R_{1+1} is R_{1-4} . The class structure for $Y^{(d)}$ is given in table 5.2.

Icosahedral algebra class structure

w=0	w=72	w=144	w=120	w=180
1+	w=720 - 72	w=720 -144	w=720 - 120	w=720 -180
	R1+1	R1+2	r1+1	i1+
	R1-4	R1-3	r1-2	i1-
	R2+1	R2+2	r2+1	i2+
	R2-4	R2-3	r2-2	i2-
	R3+1	R3+2	r3+1	i3+
	R3-4	R3-3	r3-2	i3-
	R4+1	R4+2	r4+1	i4+
	R4-4	R4-3	r4-2	i4-
	R5+1	R5+2	r5+1	i5+
	R5-4	R5-3	r5-2	i5-
	R6+1	R6+2	r6+1	i6+
	R6-4	R6-3	r6-2	i6-
			r7+1	i7+
			r7-2	i7-
			r8+1	i8+
			r8-2	i8-
			r9+1	i9+
			r9-2	i9-
			r10+1	i10+
			r10-2	i10-
				i11+
				i11-
				i12+
				i12-
				i13+
				i14+
				i15+
				i15-

Class Operators

$$C_1 = \{1\}$$

$$C_R = \{R_1 + \dots + R_6 - R_1^3 - \dots - R_6^3\}$$

$$C_{R^2} = \{R_1^2 + \dots + R_6^2 - R_1^4 - \dots - R_6^4\}$$

$$C_r = \{r_1 + \dots + r_{10} - r_1^2 - \dots - r_{10}^2\}$$

$$C_i = \{i_1 + \dots + i_{15}\}$$

Table 5.2 Class structure of the icosahedral algebra is shown in the highlighted boxes. Class operators are sums over corresponding class elements.

With these class operators, character tables 5.3 can be constructed.

$Y^{(d)}$	C_1	C_R	C_{R^2}	C_r	$T^{(d)}$	C_1	C_r	C_{r^2}	$C_3^{(d)}$	C_1	C_r	C_{r^2}
$E_{1/2}$	2	F^+	$-F^-$	1	E_1	2	1	1	A_{16}	1	ζ_6^*	$-\zeta_6$
$E_{7/2}$	2	F^-	$-F^+$	1	E_2	2	$-\zeta_6$	ζ_6^*	A_{36}	1	-1	1
G	4	1	-1	-1	E_3	2	$-\zeta_6^*$	ζ_6	A_{56}	1	ζ_6	$-\zeta_6^*$
I	6	-1	1	0								

$D_5^{(d)}$	C_1	C_R	C_{R^2}	C_ρ	$C_5^{(d)}$	C_1	C_R	C_{R^2}	C_{R^3}	C_{R^4}
A_1	1	-1	1	$-5i$	A_{110}	1	ζ_1	$-\zeta_3$	ζ_3^*	$-\zeta_1^*$
A_2	1	-1	1	$5i$	A_{310}	1	ζ_3	$-\zeta_1^*$	ζ_1	$-\zeta_3^*$
E_2	2	F^+	$-F^-$	-1	A_{510}	1	-1	1	-1	1
E_2	2	F^-	$-F^+$	0	A_{710}	1	ζ_3^*	$-\zeta_1$	ζ_1^*	$-\zeta_3$
					A_{910}	1	ζ_1^*	$-\zeta_3^*$	ζ_3	$-\zeta_1$

Table 5.3 $Y^{(d)}$, $T^{(d)}$, $C_3^{(d)}$, $D_5^{(d)}$, $C_5^{(d)}$ ray representation characters

$$\{ \zeta_1 = \exp(\pi i/5), \zeta_3 = \exp(3\pi i/5), \zeta_6 = \exp(\pi i/3) \}$$

The all-commuting projection operators are defined by the relation,

$$P^\alpha = \frac{l^\alpha}{{}^0G} \sum_{C_g} \chi_{C_g}^{\alpha^*} C_g \quad (5.9)$$

where the χ are the characters as tabulated, $l^\alpha = \chi_{C_1}^\alpha$ is order of degeneracy for α species, and ${}^0G = 60$ is the order of the algebra's generating group Y . The characters may be used to find correlations of representations for the subgroup chain $SU(2) \supset Y^{(d)}$ and the symmetry species of their proper subgroups (See Tables 5.4 and 5.5). The procedures for this analysis are given in appendix B.

$SU(2) \leftrightarrow Y^{(d)}$	$E_{1/2}$	$E_{7/2}$	G	I
$J=1/2$	1	.	.	.
$3/2$.	.	1	.
$5/2$.	.	.	1
$7/2$.	1	.	1
$9/2$.	.	1	1
$11/2$	1	.	1	1
$13/2$	1	1	1	1
$15/2$.	.	1	2
$17/2$.	1	1	2
$19/2$	1	1	1	2
$21/2$	1	.	2	2
$23/2$	1	1	2	2
$25/2$	1	1	1	3
$27/2$.	1	2	3
$29/2$	1	1	2	3

Table 5.4 Correlations between $SU(2)$ angular momentum J states ($J < 31/2$) and icosahedral double group species

$Y^{(d)} \leftrightarrow C_5^{(d)}$	A_{110}	A_{310}	A_{510}	A_{710}	A_{910}	$Y^{(d)} \leftrightarrow C_3^{(d)}$	A_{16}	A_{36}	A_{56}
$E_{1/2}$	1	.	.	.	1	$E_{1/2}$	1	.	1
$E_{7/2}$.	1	.	1	.	$E_{7/2}$	1	.	1
G	1	1	.	1	1	G	1	2	1
I	1	1	2	1	1	I	2	2	2

Table 5.5 Correlations between global $Y^{(d)}$ symmetry reps. and the local $C_5^{(d)}$ and $C_3^{(d)}$ cyclic rotational subgroups.

The correlations for subgroup chains $Y^{(d)} \supset C_5^{(d)}$ and $Y^{(d)} \supset C_3^{(d)}$ (Tables 5.5) may be read by columns to indicate which $Y^{(d)}$ symmetry species are contained in a given quasi-degenerate cluster of the C_5 and C_3 type. For the $J=100.5$ levels shown in figure

5.2, the lowest cluster corresponds to $2K \bmod 6 = 201 \bmod 6 = 3_6$ and the 3_6 column of table 5.5b which consists of two G and two I species, and these levels appear in the lowest cluster. In the separatrix region the C_3 and C_5 clusters merge and some levels appear to belong to either (or neither) type. However, the ordering remains consistent throughout the entire J manifold as discussed below. The last valid 12-fold degenerate cluster has a minimum or cutoff value which for K can be approximated with use of the angles between the separatrix plane and the C_5 or C_3 axes shown in figure 5.2. The angular momentum cone with this angle corresponds to a cutoff value for the K quantum number.

$$\frac{K_{\text{cutoff}}^{(5)}}{|J|} = \text{Cos}(\theta_{\text{cutoff}}^{(5)}) \quad (5.10)$$

This gives the cutoff values $K^{(5)} = 90.5$ for $J=100.5$. Similarly, the cutoff angle for the C_3 induced clusters give a cutoff value of $K^{(3)} = 99.5$ for the same total J value.

Level ordering and cluster structure seen in figure 5.2 can be predicted for any half-integral J using equation (5.10) and the wheels shown in figure 5.4. To get the qualitative ordering one need only determine which wheel corresponds to a particular choice of J . This is done by determining which relation $(2J-1) \bmod 4 = 0_4$ or $(2J-1) \bmod 4 = 2_4$ is satisfied. Next one calculates $2J \bmod 20$ and $2J \bmod 12$ and locates those numbers on the outside and inside of the correct wheel. The level ordering is then found by starting with the correct J value following the arrows around the wheel until you reach the K -cutoff values calculated by (5.10). Taking the $J = 100.5$ case for example, the bottom wheel applies since J satisfies that wheel's equation $(201-1) \bmod 4 = 0_4$. The most extreme 12-fold cluster is determined by satisfying $2(100.5) = 1 \bmod 20$. So the highest cluster is a $(E_{1/2}GI)_{10}$ cluster followed by a $(IGE_{1/2})_{9_{10}}$ cluster, on down to the last

complete 12-fold cluster at $K^{(5)}=90.5$, which satisfies the relation $2(90.5) = 1 \bmod 20$ and corresponds to a 3_{10} cluster ($E_{1/2}GI$). Similarly, the 20-fold clusters indicated by the inside of the wheel are read off in the opposite direction. These begin with the lowest cluster a 3_6 ($GIIG$) followed by the cutoff cluster 1_6 ($E_{1/2}GIE_{7/2}$) cluster at $K^{(3)}=99.5$. The remaining species symbols trapped between these cutoff clusters are those in the neighborhood of the separatrix.

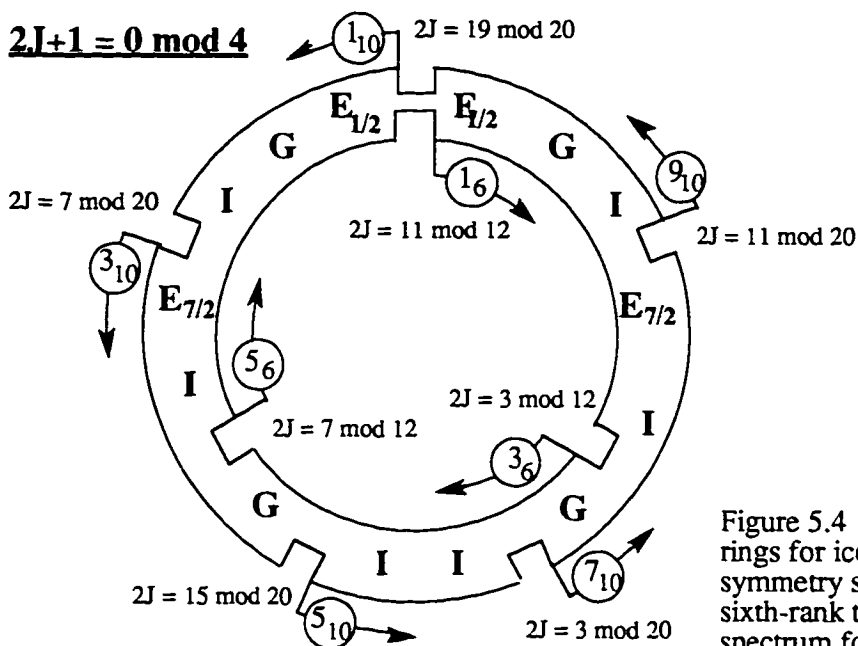
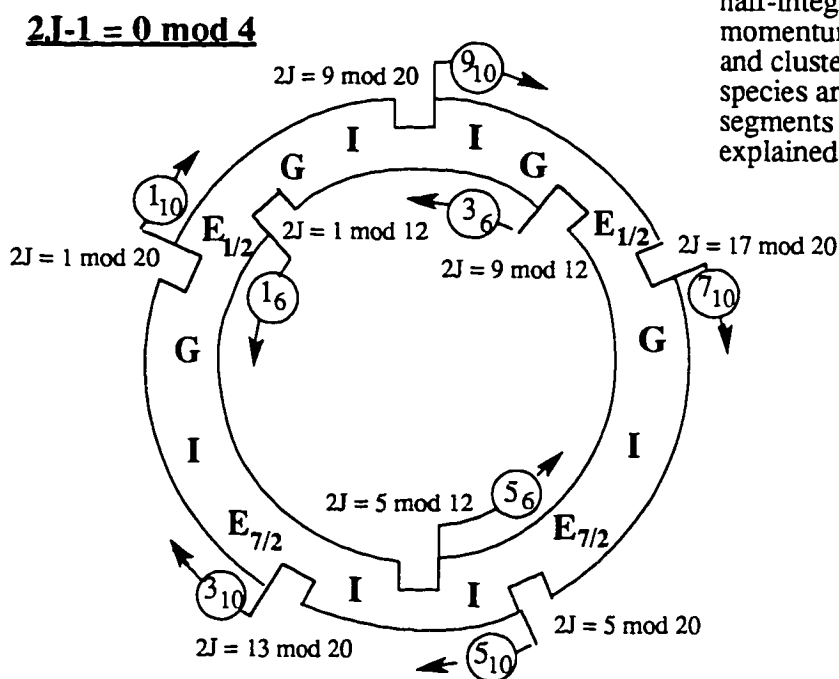


Figure 5.4 Sequencing rings for icosahedral symmetry species in sixth-rank tensor spectrum for arbitrary half-integral angular momentum J . Ordering and clustering of species are indicated by segments of the rings as explained in the text



The quantitative spacing of energy levels involves tunneling, one may take the following route used to find the relative intra-cluster spacing of 12-fold clusters. The tunneling Hamiltonian is parameterized in terms of the tunneling coefficients S between nearest-neighbors, T between next-nearest-neighbors, O between furthest-neighbor, and

the diagonal cluster centroid H discussed previously. The states will be labeled in terms of $Y^{(d)}$ rotational operators. These operators are those which take a wave packet of a given local C_5 symmetry and transform this packet over to an equivalent C_5 symmetric neighborhood of the rotational energy surface. The body's z-axis is chosen to coincide with the initial state ($|1\rangle$). The remaining basis states can be identified with left cosets of the C_5 subgroup coincident with the z-axis (body). These cosets partition the icosahedral double group into 12 sets, and the action of every operator in a given coset will carry $|1\rangle$ to an equivalent wave packet at the resultant position within a certain phase factor. The induced basis states are taken to be those coset elements (leaders) that maintain similar phase differences between the two local wave packet states. Figure 5.5 shows the representation of the tunneling Hamiltonian in a basis consisting of coset leaders that are 180° rotations.

		Basis states														
$[\mathbf{H}] =$	{	H	S	S	S	S	S	T	T	T	T	T	O	$ 1\rangle$	$ i1_+\rangle$	Figure 5.5 Representation of the C_5 induced tunneling Hamiltonian for a particular choice of coset leaders. The tunneling coefficients H, S, T, and O contain $(-1)^{1/2}$ phase terms introduced by this choice of coset leaders.
		S	H	S	T	T	S	S	T	O	T	S	T	$ 2\rangle$	$ i1_+\rangle$	
		S	S	H	S	T	T	S	S	T	O	T	T	$ 3\rangle$	$ i2_+\rangle$	
		S	T	S	H	S	T	T	S	S	T	O	T	$ 4\rangle$	$ i3_+\rangle$	
		S	T	T	S	H	S	O	T	S	S	T	T	$ 5\rangle$	$ i4_+\rangle$	
		S	S	T	T	S	H	T	O	T	S	S	T	$ 6\rangle$	$ i5_+\rangle$	
		T	S	S	T	O	T	H	S	T	T	S	S	$ 7\rangle$	$ i6_+\rangle$	
		T	T	S	S	T	O	S	H	S	T	T	S	$ 8\rangle$	$ i7_+\rangle$	
		T	O	T	S	S	T	T	S	H	S	T	S	$ 9\rangle$	$ i8_+\rangle$	
		T	T	O	T	S	S	T	T	S	H	S	S	$ 10\rangle$	$ i9_+\rangle$	
		T	S	T	O	T	S	S	T	T	S	H	S	$ 11\rangle$	$ i10_+\rangle$	
		O	T	T	T	T	T	S	S	S	S	S	H	$ 12\rangle$	$ i11_+\rangle$	

This choice of leaders introduce a phase factor of $\sqrt{-1} = i$ in the S, T, and O tunneling parameters. The reduced tunneling matrix elements may then be found using symmetry projection algebra,

$$\begin{aligned}
\langle \alpha_{mn} | \mathbf{H} | \alpha_{pq} \rangle &= \langle 1 | \mathbf{P}_{mn}^\alpha \mathbf{H} \mathbf{P}_{pq}^\alpha | 1 \rangle / N^\alpha = \langle 1 | \mathbf{H} \mathbf{P}_{nq}^\alpha | 1 \rangle \delta_{mp} / N^\alpha \\
&= \frac{1}{|G|} \sum_{g \in Y} \langle 1 | \mathbf{H} | \mathbf{g} | 1 \rangle D_{nq}^{\alpha*} \delta_{mp} / N^\alpha \\
&= \frac{1}{|G|} \sum_{h \in C_h} \langle 1 | \mathbf{H} | h \rangle D_{nq}^{\alpha*} \delta_{mp} / N^\alpha \\
&= \sum_{h \in C_h} \langle 1 | \mathbf{H} | h \rangle D_{nq}^{\alpha*} \delta_{mp}
\end{aligned} \tag{5.11}$$

Here the summation is over the coset leaders. Only the first row of the original tunneling Hamiltonian matrix is needed. The results for the case where the T and O are assumed to be negligible (T=O=0) are shown in figure 5.6(a). The 20-fold clusters determined in the same manner are shown in figure 5.6(c). One notices that the 1_{10} and the 9_{10} clusters are additive inverses of each other, and the same holds for the 3_{10} and 7_{10} , as well as the 1_6 and 5_6 clusters.

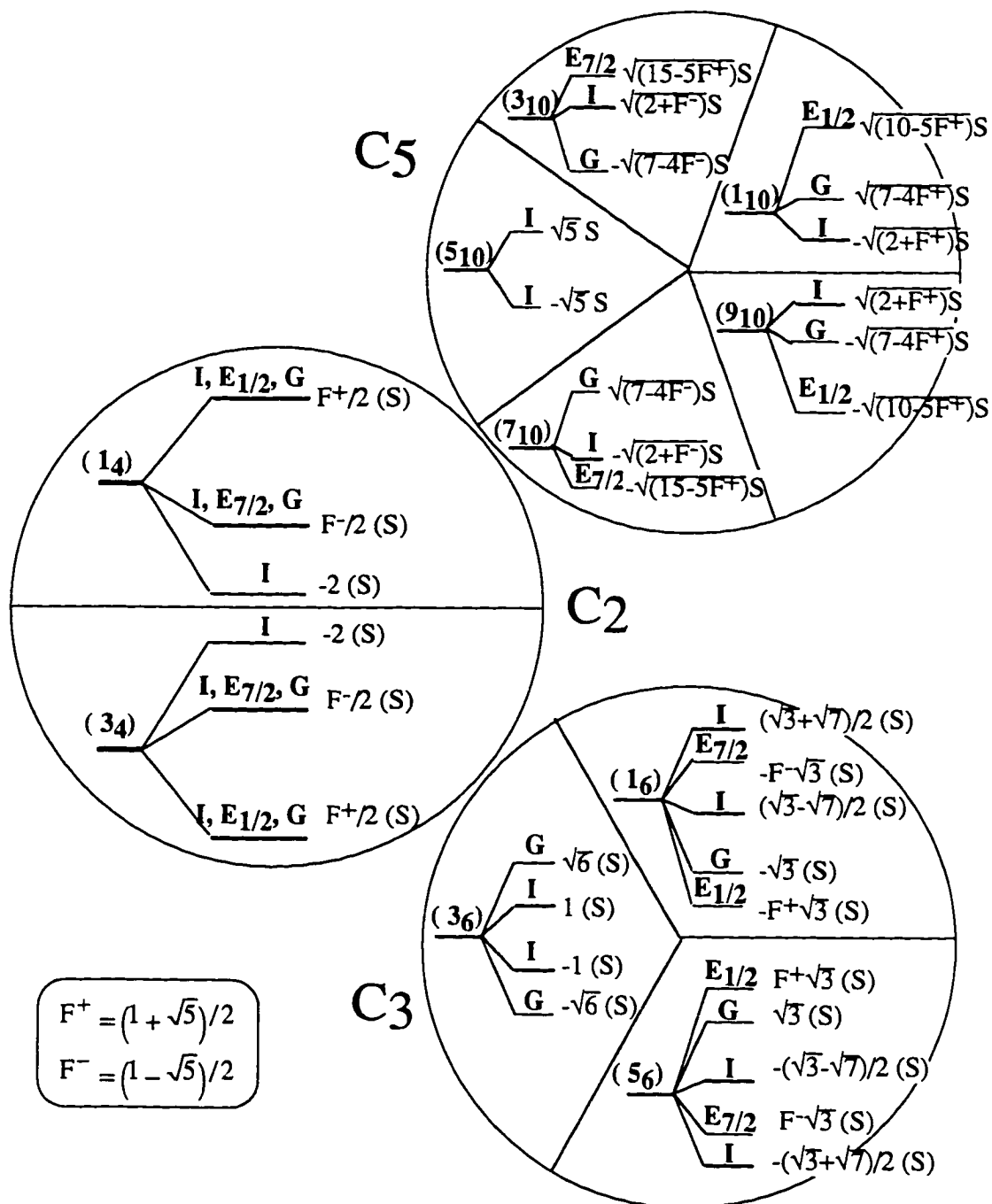


Figure 5.6 Detailed form of superfine structure for clusters associated with three types of local symmetry. Level splittings for each of the symmetry species are given relative to the cluster centroid in terms of its nearest-neighbor tunneling amplitude (S).

It is instructive to compare the ratios of adjacent energy spacings of the exact values with those found by induced representations. These ratios are tabulated in table 5.6 for several J values and both the 12-fold and 20-fold clusters. The comparison improves with increasing J, since the more isolated wave packet is influenced predominantly by its nearest tunneling opportunity. The same holds for 12-fold clusters which can become even more isolated than their 20-fold counterparts as seen in figure 5.3, because of the larger phase space angle separating the axes of the C_5 symmetric peaks.

Ratios $C_5^{(d)}$	Induced Representation	Exact numerical values				Cluster
		J = 50.5	100.5	150.5	200.5	
$\frac{E_{7/2}-I}{I-G}$	0.341641	0.332...	0.341638	0.341642	0.341641	$7_{10}, 3_{10}$
$\frac{E_{1/2}-G}{G-I}$	1.341642	1.341563	1.341635	1.341641	1.341641	$1_{10}, 9_{10}$
$C_3^{(d)}$		J = 48.5	100.5	150.5	200.5	
$\frac{G^+-I^+}{I^+-G^-}$	0.72474	1.034... ⁽¹⁾	0.729537	0.729537 ⁽²⁾	0.724870	3_6
$\frac{I^+-E_{7/2}}{E_{7/2}-I^-}$	0.73229	1.149...	0.912585	0.732668	0.73229 ⁽³⁾	$1_6, 5_6$
$\frac{E_{7/2}-I^-}{I^- - G}$	1.19771	1.222...	1.210003	1.197907	1.19769 ⁽³⁾	$1_6, 5_6$
$\frac{I^- - G}{G - E_{1/2}}$	1.19127	1.337...	1.269764	1.191560	1.19125 ⁽³⁾	$1_6, 5_6$

Table 5.6 Comparison of exact cluster centroids and approximations for C_5 clusters for various half-integral J. Approximation techniques that are used are explained in text. (Note - Superscript implies different J value: (1): J=49.5 , (2): J=148.5 , and (3) via reciprocal cluster)

Chapter 6 Rotational Level Fine Structure of the buckyball isomer $^{13}\text{C}^{12}\text{C}_{59}$

XC_{59} Molecule

Rotational fine and superfine structure for the Buckyball isomer $^{13}\text{C}^{12}\text{C}_{59}$ will be investigated and compared with that of $^{12}\text{C}_{60}$ spectra using quantum mechanical and semi-classical theory. Rotational spectra of $^{13}\text{C}^{12}\text{C}_{59}$ differs markedly from that of Buckyball because the presence of a single additional neutron completely breaks the rotational symmetry. While C_{60} has the highest point group symmetry Y_h , $^{13}\text{C}^{12}\text{C}_{59}$ has only a single C_v reflection plane. Predictions will be made for the different spectroscopic structure of this broken icosahedral symmetry, as would also be encountered in single site *intrahedral* doping XC_{59} . Semi-classical techniques help to label the spectra of molecules undergoing such extreme symmetry breaking.

The possible point symmetries of the various doped Fullerene and "metcar" structures range from Y_h (icosahedral-inversion), the highest point symmetry in 3-space, through a multitude of lower point symmetries including (most often) no symmetry at all. Many of these symmetries can be obtained by replacing carbon ^{12}C atoms by the next most abundant isotope ^{13}C . Indeed, a single ^{13}C in C_{60} reduces Y_h symmetry to only bilateral reflection or C_v symmetry, and two ^{13}C isotopes may for some steric placements leave the Buckyball cage with no symmetry at all. For Buckyball composed of both ^{12}C and ^{13}C atoms there are a vast number of substructures can be formed each with their own inherent symmetries and probabilities of formation. For a fractional natural abundance of p for ^{13}C , the probability $P(p,n)$ for a 60 carbon molecule composed of n ^{13}C atoms is given by equation 6.1.

$$P(p,n) = \frac{60!}{n!(60-n)!} p^n (1-p)^{60-n} \quad (6.1)$$

The most likely isomer (>35% for natural abundances usual in manufacture) to be formed from current production methods is that of $^{13}\text{C}^{12}\text{C}_{59}$. Some possible features of the rotational level structure this molecule will be considered in this chapter. These features are likely to appear in high resolution rotation-vibration spectra of a gas containing Fullerenes produced without isotopic selection. Similar features can be expected from spectra obtained from XC_{59} .

Approximating the Semi-rigid Rotational Hamiltonian

An analysis of the symmetry of $^{13}\text{C}^{12}\text{C}_{59}$ finds that the exceptional icosahedral symmetry has been broken. Since the ^{13}C atom occupies a site with C_v local symmetry the rotational symmetry is reduced to the C_1 identity group. This implies that many of the degeneracies due to higher symmetry have been lifted. To illustrate this the rotational Hamiltonian is modeled by equation 6.2.

$$\begin{aligned} \mathbf{H} &= \mathbf{B}\mathbf{J}^2 + t_{066} \left(\frac{\sqrt{11}}{5} \mathbf{T}_0^6 + \frac{\sqrt{7}}{5} (\mathbf{T}_5^6 + \mathbf{T}_{-5}^6) \right) + \mathbf{H}_{\text{sym}} \\ \mathbf{H}_{\text{sym}} &= \tilde{\mathbf{R}}^{-1}(\cdot, \beta', \cdot) \left\{ \mathbf{D}\mathbf{J}^2 + \mathbf{E}\mathbf{T}_0^2 \right\} \mathbf{R}(\cdot, \beta', \cdot) \end{aligned} \quad (6.2)$$

The first two terms of \mathbf{H} model a rotating semi-rigid icosahedrally symmetric molecule¹, where the second term models the lowest order icosahedrally anisotropic centrifugal coriolis distortion. The third term \mathbf{H}_{sym} is the Hamiltonian of a rigid symmetric top rotated by β' to align with the ^{13}C site. Such transformations can be characterized as linear combinations of the irreducible tensors with Wigner D-function coefficients. Other isotropic or symmetric-top distortion operators such as \mathbf{T}_0^4 are

ignored in this model. The remaining terms vary like $|J|^2$ or $|J|^6$, and the sixth rank tensor terms would tend to be dominant for high J. For lower J values and up to some critical J the symmetric top terms would be most influential.

In the usual angular momentum basis, the quantum-mechanical Hamiltonian has the following representation,

$$H_{KK'} = (B + D)|J|^2 + t_{066}\langle J||6||J \rangle \left(\frac{\sqrt{11}}{5} C_{0KK}^{6JJ} + \frac{\sqrt{7}}{5} (C_{5KK+5}^{6JJ} + C_{-5KK-5}^{6JJ}) \right) + E\langle J||2||J \rangle \sum_{n=-2}^2 D_{0n}^2(\cdot, \beta', \cdot) C_{nKK+n}^{2JJ} \quad (6.3)$$

To aid in viewing and analysis the zero rank term is set to unity and a parameter τ is introduced which will contain all coefficients and reduced matrix elements. The higher ranked terms are then rescaled to 2/10's of the scalar term.

$$H_{KK'} = 1 + \frac{2}{10} \left(\tau \sum_{n=-2}^2 D_{0n}^2(\cdot, \beta', \cdot) C_{nKK+n}^{2JJ} + (1 - \tau) \left(\frac{\sqrt{11}}{5} C_{0KK}^{6JJ} + \frac{\sqrt{7}}{5} (C_{5KK+5}^{6JJ} + C_{-5KK-5}^{6JJ}) \right) \right) \quad (6.4)$$

Note that τ represents the relative amounts of second rank terms with respect to the sixth rank terms and would be J dependent for fixed molecular constants t_{066} and E. The spectra for XC_{59} single site doping will differ from that of $^{13}C^{12}C_{59}$ by the value of E and t_{066} and hence of τ . Furthermore, certain types of doping at sites with other than C_v local symmetry may be treated as above with an appropriate choice of β' and will be analyzed in the next chapter.

Rotational Energy Surface

In order to view the eigensolutions of equation 6.2 in a semi-classical manner, a rotational energy (RE) surface is constructed using the asymptotic expectation values of the tensor operators T_q^r ,

$$T_q^r \rightarrow D_{0q}^r(\cdot, -\beta, -\gamma)|J|^r = C_q^r(\theta, \phi)|J|^r \quad (6.5a)$$

The asymptotic values involve Wigner D-functions D_{0q}^r , and multipole functions C_q^r . The polar and azimuthal angles in the body frame. These are related to the Euler angles by

$$\theta = -\beta, \phi = -\gamma \quad (6.5b)$$

and are used to plot the trajectories associated with the evolution of classical angular momentum vectors for fixed magnitude $|J|$ and constant energy. The classical Hamiltonian derived from (6.2) has the following polynomial form upon replacement of each rank-r tensor operator T_q^r with a corresponding r-th degree multipole function C_q^r .

$$\begin{aligned} H = 1 + & \\ & \frac{2}{10} \tau \left(\frac{3}{4} \sin^2(\beta') \sin^2(\theta) \cos(2\phi) + \frac{3}{4} \sin(2\beta') \sin(2\theta) \cos(\phi) + \frac{1}{4} (3 \cos^2(\beta') - 1) (3 \cos^2(\theta) - 1) \right) + \\ & \frac{2}{10} (1 - \tau) \left(\frac{1}{16} (231 \cos^6(\theta) - 315 \cos^4(\theta) + 105 \cos^2(\theta) - 5 - 42 \sin^5(\theta) \cos(\phi) (5 - 20\phi^2 + 16\phi^4)) \right) \end{aligned} \quad (6.6a)$$

From the geometry of the fullerene structure we find that the polar angle β' subtending to the C^{13} site has the following value.

$$\beta' = \arctan\left(\frac{2 - 8F^-}{19}\right) = 0.35040541\dots$$

$$F^- = \frac{1 - \sqrt{5}}{2} \tag{6.6b}$$

As in the case of equation 6.4 the τ coefficients contain all coefficients and are then scaled to 2/10's of the scalar term.

The RE surfaces for $J = 50$ are plotted in figure 6.1a for six values of $\tau = [0, 1/5, 2/5, 3/5, 4/5, 1]$. Figure 6.1a reveals a variety of classical RE surface shapes. Below them in figure 6.1b are the exact energy levels which are obtained by diagonalizing the $2J+1$ by $2J+1$ Hamiltonian matrix given by equation 6.4 for $J = 50$. The classical J trajectories are topography lines (constant energy) and the certain "quantizing" classical levels correspond to certain parts of the quantum energy plots figure 6.1b shown directly below each shape.

The RE surface plots may be viewed as rotational phase space portraits. Each quantizing phase path corresponds to an eigenfunction or set of eigenfunctions belonging to a given level or cluster of levels. Multiply congruent paths belong to a multiplet of levels, which would have degenerate classical energies, but are split by tunneling in the quantum system. Tunneling would occur, for example, between regions of similar local symmetry. Consider the RE surface on the left side of figure 6.1a. The 12 peaks contain higher energy pentagonal trajectories that have C_5 local symmetry and correspond to a 12-fold nearly-degenerate multiplet. Similarly, the 20 equivalent valleys have C_3 symmetry and correspond to a 20-fold nearly degenerate cluster at the extreme lower left half side of figure 6.1b. There is only room for one C_3 cluster because its eigenfunctions occupy a smaller percentage of the available rotational phase space. Also the C_3 cluster is split more than the C_5 clusters because the tunneling is greater.

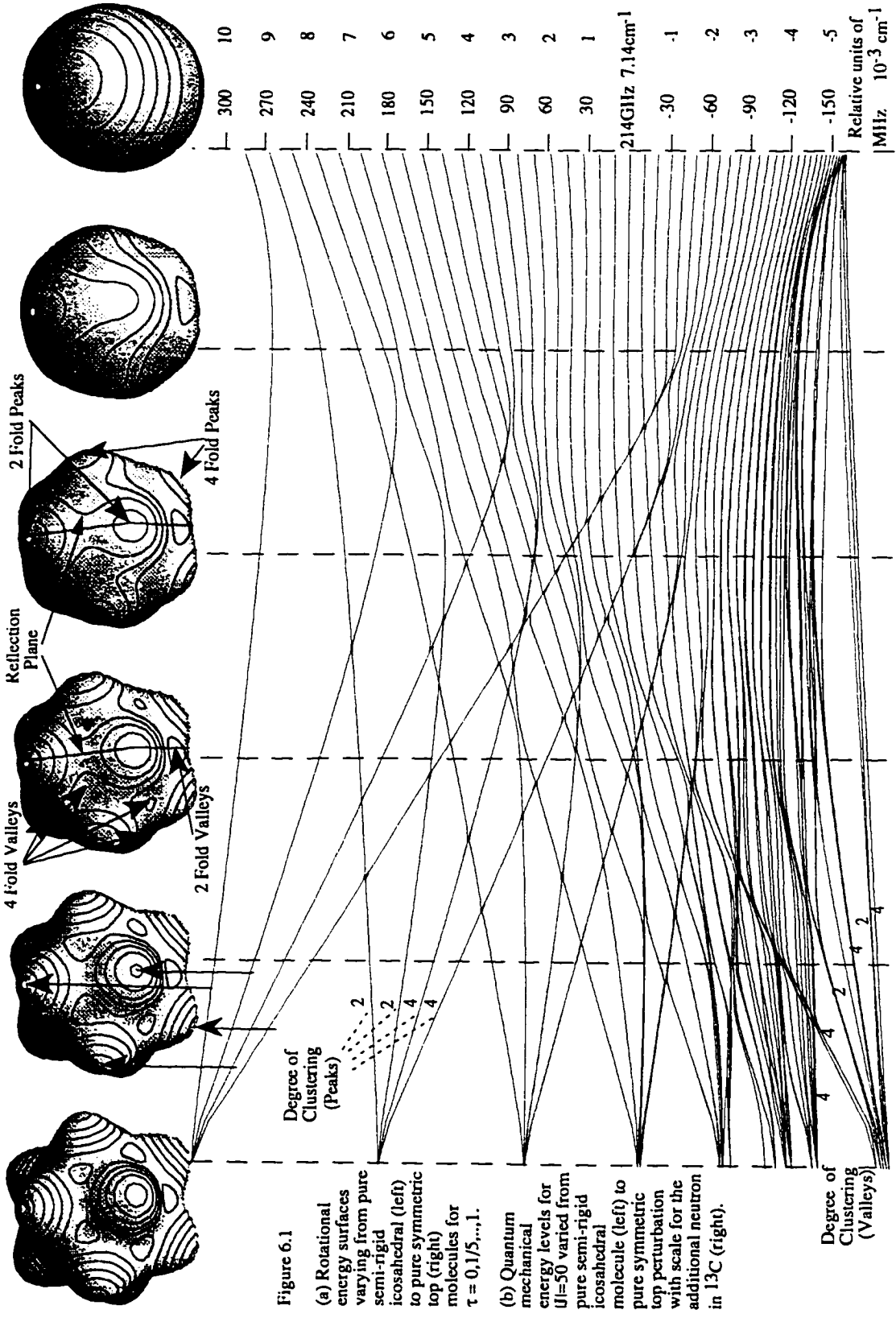


Figure 6.1
 (a) Rotational energy surfaces varying from pure icosahedral (left) to pure symmetric top (right) molecules for $\tau = 0, 1/5, \dots, 1$.
 (b) Quantum mechanical energy levels for $J=50$ varied from pure semi-rigid icosahedral molecule (left) to pure symmetric top perturbation with scale for the additional neutron in ^{13}C (right).

Dividing these well defined regions of non-zero curvature is the separatrix which contains the points of inflection. This region is in close proximity to both the 5-fold and 3-fold regions and corresponds to delocalized and unclustered states that are very sensitive to changes in the parameter τ . They would also be highly susceptible to other perturbations of the Hamiltonian.

The extreme left of figure 6.1 is the limiting case for $\tau \rightarrow 0$ and would correspond more nearly to the spectrum one expects for high J where high ranking coriolis and centrifugal effects are dominant. The limit $\tau = 0$ belongs to the pure icosahedrally symmetric energy levels and RE surface. The extreme clustering for the high and low energy values is indicative of the spectra obtained from highly symmetric molecules. This clustering is the rotational analog to the band structure exhibited in solids with translational symmetries. Within these clusters of 12 and 20 nearly degenerate levels there are the standard symmetry degeneracies of the order 1, 3, 3, 4, and 5 corresponding to the dimension of icosahedral symmetry species A , T_1 , T_2 , G , and H respectively. The clusters are all in groups of 12 for the higher energies or 20 for the few lower energy clusters with a set of unclustered levels separating the bands of clusters. The unclustered region is referred to as the separatrix region. All these structures can be associated with the leftmost RE surface directly above. White dots at the tops of the RE surfaces show the body's azimuthal axis chosen to be a 5-fold rotational axis. The visible portions of 12 rotationally equivalent peaks containing the C_5 symmetric trajectories of the classical angular momentum vectors are indicated by the dark loops (or level curves). The trajectories for the single 20-fold cluster can be seen in the low energy triangular valleys. For each surface in figure 6.1b six evenly spaced level curves are plotted, which correspond to states of equally spaced energy. These trajectories may be envisioned as expectation trajectories for the angular momentum vectors in coherent states composed of the quantum-mechanical states belonging to the corresponding clusters.

For low angular momentum, (or equivalently $\tau \rightarrow 1$) the second order tensor terms in equation 6.2 play the dominant role and in the extreme case ($\tau=1$) the pure symmetric top Hamiltonian is obtained. Along the right hand edge of figure 6.1b, the energy levels are plotted for a rotating symmetric top with the same $J=50$. The high energy values occur in 2-fold clusters comprised of rotationally degenerate doublets labeled by symmetric top R_2 symmetry species (Π, Δ, Φ, \dots). The lowest eigenvalue corresponds to the only singlet and is of the Σ species. In the accompanying RE surface above the closest of the two equivalent peaks is seen with six of the 50 trajectories drawn. The waist of the surface contains the trajectory of singlet state and would be referred to as the separatrix if in actuality it separated differing types of clusters. A more comprehensive analysis of the rotational spectra of these symmetric molecules has been published.¹

It is the values of τ that lie between 0 and 1 that would have physical meaning for $^{12}\text{C}_59\ ^{13}\text{C}$. As viewed from right to left the RE surfaces in figure 6.1a describe the deformation that the symmetric top angular momentum trajectories would undergo as $|J|$ increases thereby emphasizing more of the molecule's icosahedral nature. The maxima of symmetric top RE surface splits into three pairs of maxima, and five minima. One pair of maxima lie in the plane of reflection symmetry and the other two pair straddle this plane. The pentad of minima are joined by another pentad of minima evolving from the separatrix region. The same process occurs on the other side of the RE surface providing the 20 equidistant C_3 symmetric minima and the 12 C_5 symmetric maxima of the pure icosahedral surface.

The mixed RE surfaces provide information about the quantum-mechanical spectra for $^{13}\text{C}^{12}\text{C}_59$. The RE extrema found on the reflection plane appear in equivalent pairs, while those off plane fall into groups of four. The radial placement on the surface gives the

ordering of these two and four fold clusters that correspond to the pure icosahedral 12 and 20-fold clusters. The 12-fold clusters split into subclusters of order 2, 2, 4, and 4 and the 20-fold clusters break into subclusters of order 4, 4, 2, 4, 2, and 4. This ordering is visible near the separatrix region in figure 6.1b. The clusters nearest the separatrix lose their icosahedral clustering characteristics sooner than the more isolated extreme energy clusters. Those energy levels not belonging to any well defined cluster are perturbed almost immediately upon making τ non zero, and this is evident by the prominent mixing of levels. Similarly, as τ becomes less than 1 the Symmetric top Σ singlet and low lying doublets are first to mix.

The symmetry labeling of the 2 and 4 fold subclusters can be determined by relating the local symmetry of the corresponding trajectories to the global symmetry of the RE surface. Noting that the RE surface must be invariant to angular momentum inversion or time reversal the global rotational symmetry is $C_{2h} = C_v \times C_i$. The 2-fold trajectories lie on the plane of symmetry and therefore the 2-fold subclusters correspond to A_+ , and A_- . C_v symmetry species induced to C_{2h} , namely $A_+ \uparrow C_{2h} = 0_{2g} \oplus I_{2u}$ and $A_- \uparrow C_{2h} = 0_{2u} \oplus I_{2g}$. The 4-fold trajectories have only trivial C_1 local symmetry and therefore the 4-fold subclusters correspond to the lone O_1 symmetry species induced to C_{2h} , $O_1 \uparrow C_{2h} = 0_{2g} \oplus I_{2g} \oplus 0_{2u} \oplus I_{2u}$ which is the C_{2h} regular representation. This implies that in all subclusters no true degeneracies exist, only singly degenerate lines will occur for $0 < \tau < 1$. However, nearly degenerate 2-fold and 4-fold clusters are prevalent.

As in the $\tau = 0$ and 1 extremes, clusters of a given type appear to emerge from the separatrix in an exponential manner. The number of contiguous clusters that appear is determined by the amount of phase space available to those trajectories. An approximation using angular momentum cone geometry² can be used to estimate the number of clusters allowed before mixing into the separatrix region. This involves finding a minimum or

cutoff value K_{cutoff} for the azimuthal quantum number. Clusters can then be labeled by azimuthal quantum number $K= 50, \dots, K_{\text{cutoff}}$. Critical angles θ_{critical} separating dissimilar regions on the RE surface are then used to find the cutoffs. θ_{critical} is the angle between a local symmetry axis of quantization or classically stable fixed point and the nearest (unstable) separatrix point. From this angle we derive the cutoff value.

$$K_{\text{cutoff}} = \sqrt{J(J+1)} \cos(\theta_{\text{critical}}) \quad (6.7)$$

In the symmetric top case ($\tau=1$) an angle of 90° separates the 2-fold maxima from the separatrix giving a cutoff of $K_{\text{cutoff}} = 0$ for all J . The critical angle in the pure icosahedral case ($\tau=0$) for the 12-fold clusters is $\theta_{\text{critical}} = 26.6^\circ$ giving a ($J = 50$) cutoff of $K_{\text{cutoff}} = 45$, which is observed in figure 6.1b. Similarly, the 20-fold critical angle of 10.8° gives a ($J = 50$) cutoff of $K_{\text{cutoff}} = 50$ allowing only the lone 20-fold cluster observed at the bottom of figure 6.1b. Cutoffs for the broken symmetry cases between these extremes may be approximated in a similar fashion. Those clusters that dominate in the RE surfaces have lower cutoff points and persist through the widest range of τ values. The highest 2-folds and lowest 2 and 4-fold clusters span the majority of τ values.

Superfine Level Structure

The superfine structure of the clusters determines the intra-subcluster level spacing. Splitting of the 2-fold clusters arises from tunneling between two equivalent C_v symmetric regions on the RE surface. Each pair of C_v symmetric regions would have a tunneling amplitude S that is related to their locations along the plane of symmetry. The 2-fold tunneling Hamiltonian then has the form,

$$[H_{2\text{-fold}}] = \begin{pmatrix} H & S \\ S & H \end{pmatrix} \quad (6.8)$$

with eigenvalues $\{\lambda_{2\text{-fold}}\} = H \pm S$. Figure 6.2a illustrates the A_+ and A_- 2-fold clusters labeled by C_{2h} symmetry species for $S \in [0, 0.5]$. Note that the uppermost 2-fold peak of figure 6.1a is situated nearest the H_{sym} deformation and being more isolated would have less splitting than clusters arising from the remaining C_v regions. Also as $\tau \rightarrow 1$, the 2-fold trajectories become more isolated, S goes to zero and true 2-fold degeneracies are recovered for the symmetric top ($\tau=1$).

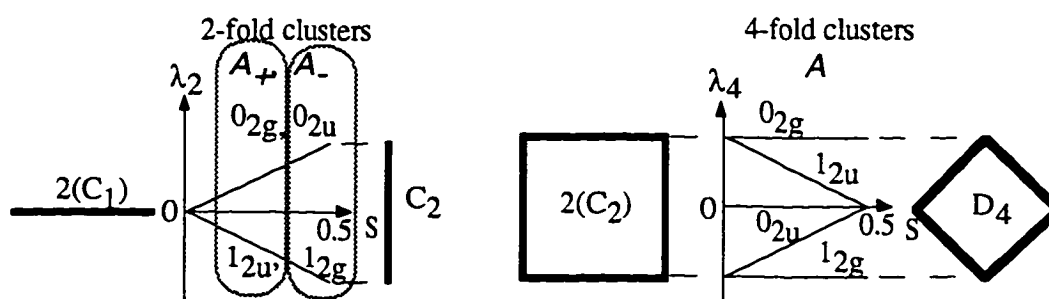


Figure 6.2 Superfine structure of 2-fold and 4-fold subclusters. in terms of relative tunneling parameter S

The intra-cluster level spacing for the 4-fold sub-clusters can be determined in a similar manner. Tunneling occurs between a set of four equivalent regions on the RE surface, and each set would have tunneling amplitudes determined by their relative locations on the RE surface. This may be modeled by varying the relative amount of nearest-neighbor $(1-S)$ and next-nearest-neighbor (S) tunneling amplitudes for $S \in [0, 0.5]$ and setting the furthest-neighbor tunneling amplitude to zero. This 4-fold tunneling Hamiltonian would have the form.

$$[H_{4\text{-fold}}] = \begin{pmatrix} H & (1-S) & S & 0 \\ (1-S) & H & 0 & S \\ S & 0 & H & (1-S) \\ 0 & S & (1-S) & H \end{pmatrix} \quad (6.9)$$

The eigenvalues are $\{\lambda_{4\text{-fold}}\} = H \pm 1, H \pm (1-S)$. Figure 6.2b illustrates 4-fold level spacing labeled by C_{2h} symmetry species for $S \in [0, 0.5]$. $S=0$ gives two pair of widely spaced doublets of two independent 2-fold systems $\{2(C_2)\}$. The $S=0.5$ case corresponds to a D_4 like system with equal nearest-neighbor and next-nearest-neighbor tunneling amplitudes. For the values $0 < S < 0.5$, the 4-fold level structure contains the species of the C_{2h} regular representation. The level patterns for the extreme values of S can be related to the vertical spacing of the vertices of a square on edge ($S=0$) and on the point ($S=0.5$). For ($0 < S < 0.5$) the 4-fold clusters and can be related to the vertices of a square tilted between the aforementioned extremes.

Chapter 7 Fullerene doping on cyclic symmetry axes

Recently, there has been evidence of preferential bonding at sites having other than C_v local symmetry. Doping and bonding may also take place at sites of the various icosahedral symmetry axes. These symmetric sites again fall in the categories of having C_2 , C_3 and C_5 local symmetries. Indeed, multiply doped complexes could reduce the icosahedral symmetry to that of any subgroup of Y_h . As with the C_v sites, there exists the possibility of exohedral, intrahedral, and endohedral inclusion.

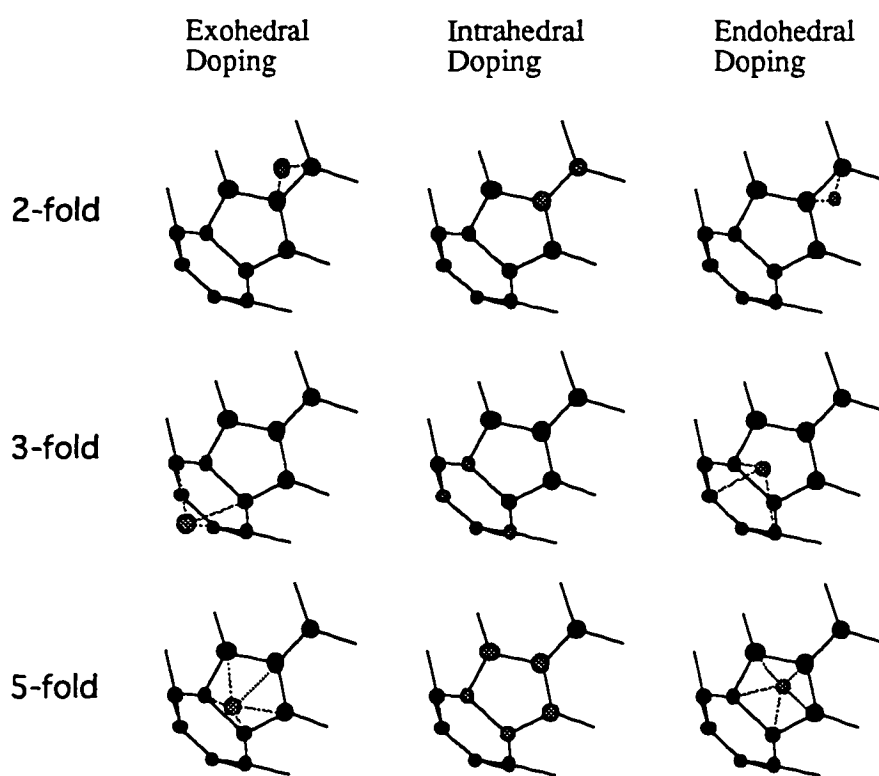


Figure 7.1 Various forms of doping that reduce rotational symmetry to icosahedral subgroups C_2 (top), C_3 , and C_5 (bottom).

For example, $C_{60}H_2$ ¹ appears to prefer exohedral 2-fold bonds, $C_{60}O_2$ units in $C_{60}(OsO_4)$ form two bonds straddling a 2-fold site², and metallic dopants seem to accommodate both endo- and exohedral bonding at both 2-fold and 5-fold sites³.

To carry out a rotational analysis, an approximation similar to that used in chapter 6 may be employed to any such configurations leaving n-fold local symmetry. Again a rigid symmetric top perturbation H_{sym} is added to the semi-rigid icosahedral Hamiltonian as in equation 6.2. However, now H_{sym} is rotated to align with one of the n-fold symmetry axes above. Since the icosahedral terms have been quantized along the 5-fold axis, polar angles β_n joining the 5-fold axis to the n-fold axes will be employed to bring H_{sym} into proper alignment. Naturally, no rotation is necessary for the 5-fold axis and $\beta_5 = 0$. The remaining polar angles are given in closed form in figure 7.2

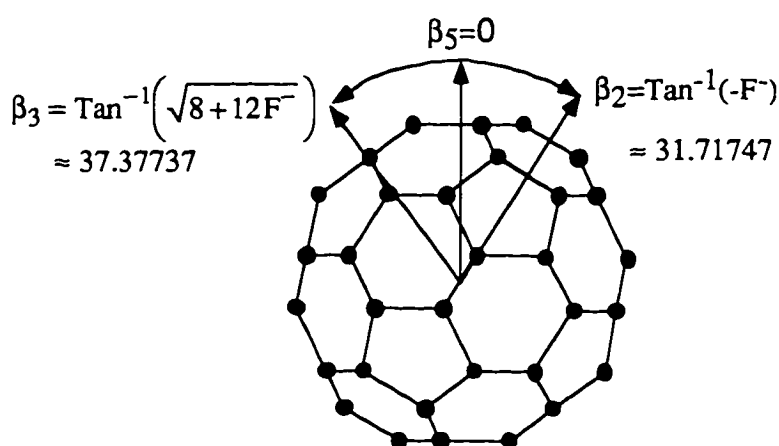


Figure 7.2 Polar angles β_n distending from the 5-fold axis to the nearest n-fold axis.

Equations 6.4 can again be utilized to calculate quantum-mechanical rotational eigenvalues, and equation 6.6 can be employed to semi-classically analyze motion in rotational phase space. One need only apply the appropriate polar angle β_n .

Symmetry Breaking on C_5 Axis

An analysis similar to that in chapter 6 is presented in figure 7.3 for the case where doping lowers the global rotational symmetry to that of D_5 . RE surfaces for four intermediate value of $\tau=1/5,2/5,3/5,4/5$ are plotted at the top. The extreme values of τ give RE surfaces identical to those in figure 6.1 and are omitted from the following illustrations. The original 12 equivalent icosahedral peaks are now split into 2 equivalent peaks that are of C_5 local symmetry and 10 equivalent peaks having C_v local symmetry. Whereas, the 20 equivalent valleys are perturbed into two sets of 10 equivalent peaks having C_v local symmetry. As τ goes from 0 to 1 less phase space is available for the 10-fold peaks and the level curves that they contain evolve into 2-fold C_5 symmetric trajectories.

At the bottom of figure 7.3, quantum-mechanical eigenvalues for $J=50$ are plotted. The degree of clustering is labeled at the left hand side. For small τ , each of the icosahedral high energy clusters contain corresponding 2-fold and 10-fold subcluster as predicted above. As τ increases the 10-fold clusters are seen to 'mix' into 2-fold clusters. In the low energy region, the two 10-fold subclusters corresponding to the icosahedral 20-fold clusters can be seen undergoing a similar evolution. The uppermost 2-fold and lowermost 10-fold subclusters persist for nearly the entire range of τ values.

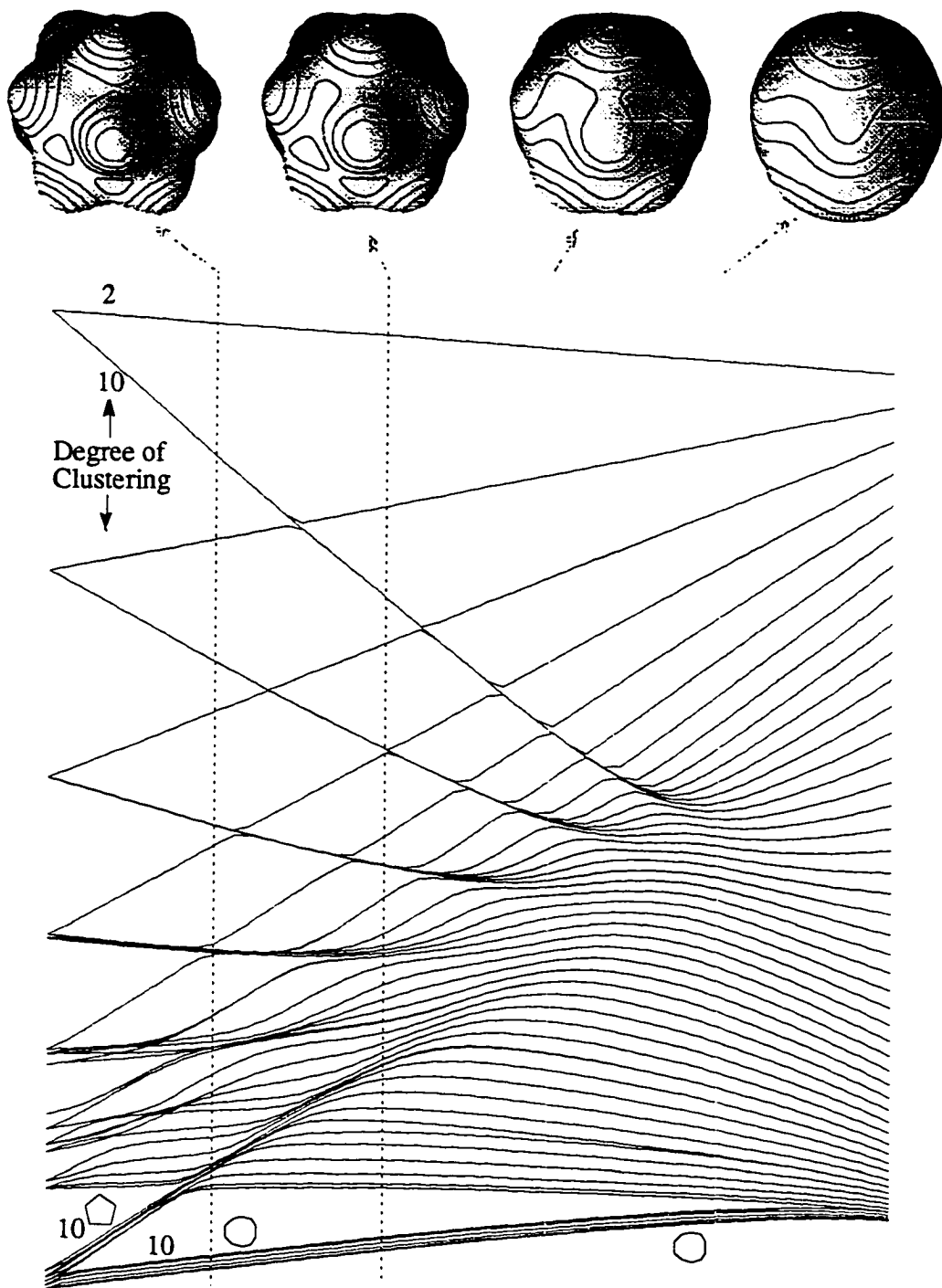


Figure 7.3 (a) Rotational energy surfaces for $\tau = 1/5, \dots, 4/5$. (b) Quantum mechanical energy levels for $|J|=50$. Both vary from pure semi-rigid icosahedral (left) to pure symmetric top centered at C_5 axes (right)

The superfine structure of the 2-fold clusters can be obtained by correlating the K_5 clusters with the global D_5 symmetry. The C_5 group is correlated to D_5 in table 7.1. The uppermost 2-fold cluster corresponds to an 0_5 cluster which from the 0_5 column of table 7.1 contains A_1 and A_2 species. The next lowest, a 4_5 2-fold cluster, contains an E_1 doublet, the 3_5 an E_2 doublet, the 2_5 an E_2 doublet and the 1_5 doublet contains an E_1 doublet. The pattern then would cycle till it reaches the separatrix region.

$D_5 \leftrightarrow C_5$	0_5	1_5	2_5	3_5	4_5
A_1	1
A_2	1
E_1	.	1	.	.	1
E_2	.	.	1	1	.

Table 7.1 Correlation table relating C_5 species to D_5 species

As τ increases the splitting between the 0_5 singlets goes to zero and all subclusters become symmetric top doublets except for one lone A_1 singlet that becomes an $R_2 \Sigma$ species.

The superfine structure of the 10-fold clusters can be approximated by using equations 5.11 and the ten-fold Hamiltonian in equation 7.1.

$$\mathbf{H}_{10\text{-fold}} = \begin{pmatrix}
 \text{H} & 1\text{-S} & \cdot & \cdot & 1\text{-S} & \text{S} & \cdot & \cdot & \cdot & \text{S} \\
 1\text{-S} & \text{H} & 1\text{-S} & \cdot & \cdot & \cdot & \text{S} & \text{S} & \cdot & \cdot \\
 \cdot & 1\text{-S} & \text{H} & 1\text{-S} & \cdot & \cdot & \cdot & \text{S} & \text{S} & \cdot \\
 \cdot & \cdot & 1\text{-S} & \text{H} & 1\text{-S} & \cdot & \cdot & \cdot & \text{S} & \text{S} \\
 1\text{-S} & \cdot & \cdot & 1\text{-S} & \text{H} & \cdot & \cdot & \cdot & \text{S} & \text{S} \\
 \text{S} & \text{S} & \cdot & \cdot & \cdot & \text{H} & 1\text{-S} & \cdot & \cdot & 1\text{-S} \\
 \cdot & \text{S} & \text{S} & \cdot & \cdot & 1\text{-S} & \text{H} & 1\text{-S} & \cdot & \cdot \\
 \cdot & \cdot & \text{S} & \text{S} & \cdot & \cdot & 1\text{-S} & \text{H} & 1\text{-S} & \cdot \\
 \cdot & \cdot & \cdot & \text{S} & \text{S} & \cdot & \cdot & 1\text{-S} & \text{H} & 1\text{-S} \\
 \text{S} & \cdot & \cdot & \cdot & \text{S} & 1\text{-S} & \cdot & \cdot & 1\text{-S} & \text{H}
 \end{pmatrix} \quad (7.1)$$

The cluster contains the species of the D_5 regular representation. In 7.1 the tunneling parameters are varied from pure pentagonal tunneling ($S=0$) to pure tunneling across the 2-fold axes ($S=1$). Figure 7.4 illustrates the various clustering found in figure 7.3b. The lowermost 10-fold cluster corresponds to S values close to 1 as would be expected from the collar-like arrangement of the low lying 10-fold congruent valleys in the RE surfaces of figure 7.3a. The higher low energy 10-fold cluster corresponds S values closer to zero and indicative the tunneling to found in two independent pentagonal potentials. The 10-fold high energy clusters have tunneling parameters to S closer to a half and are characterized by singlet species separated by one or two doublet species..

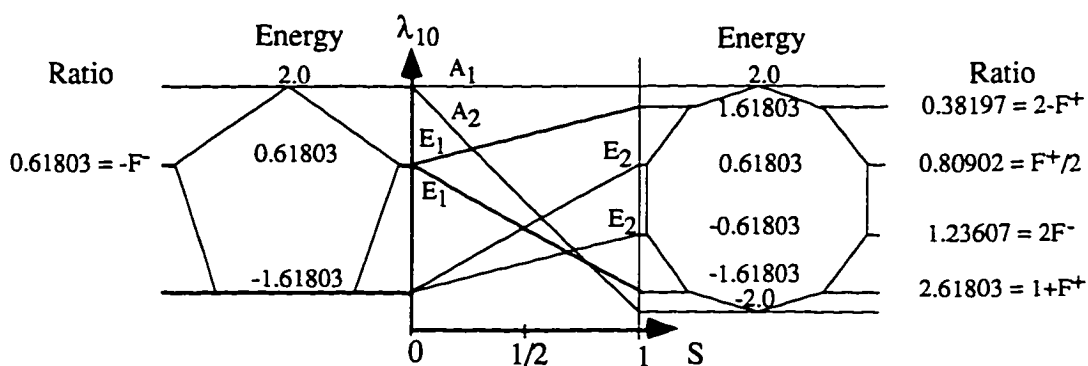


Figure 7.4 Superfine structure of the 10-fold Sub-clusters

Symmetry Breaking on C_2 Axis

The effect of structural symmetry breaking on a C_2 axis is similar to that of the C_v symmetry breaking of chapter 6, with one difference being the lack of 2-fold clusters. The overall pure rotational symmetry is D_2 which is isomorphic to $C_2 \otimes C_i$. Figure 7.5 illustrates the quantum-mechanical rotational energy levels with their associated RE surfaces.

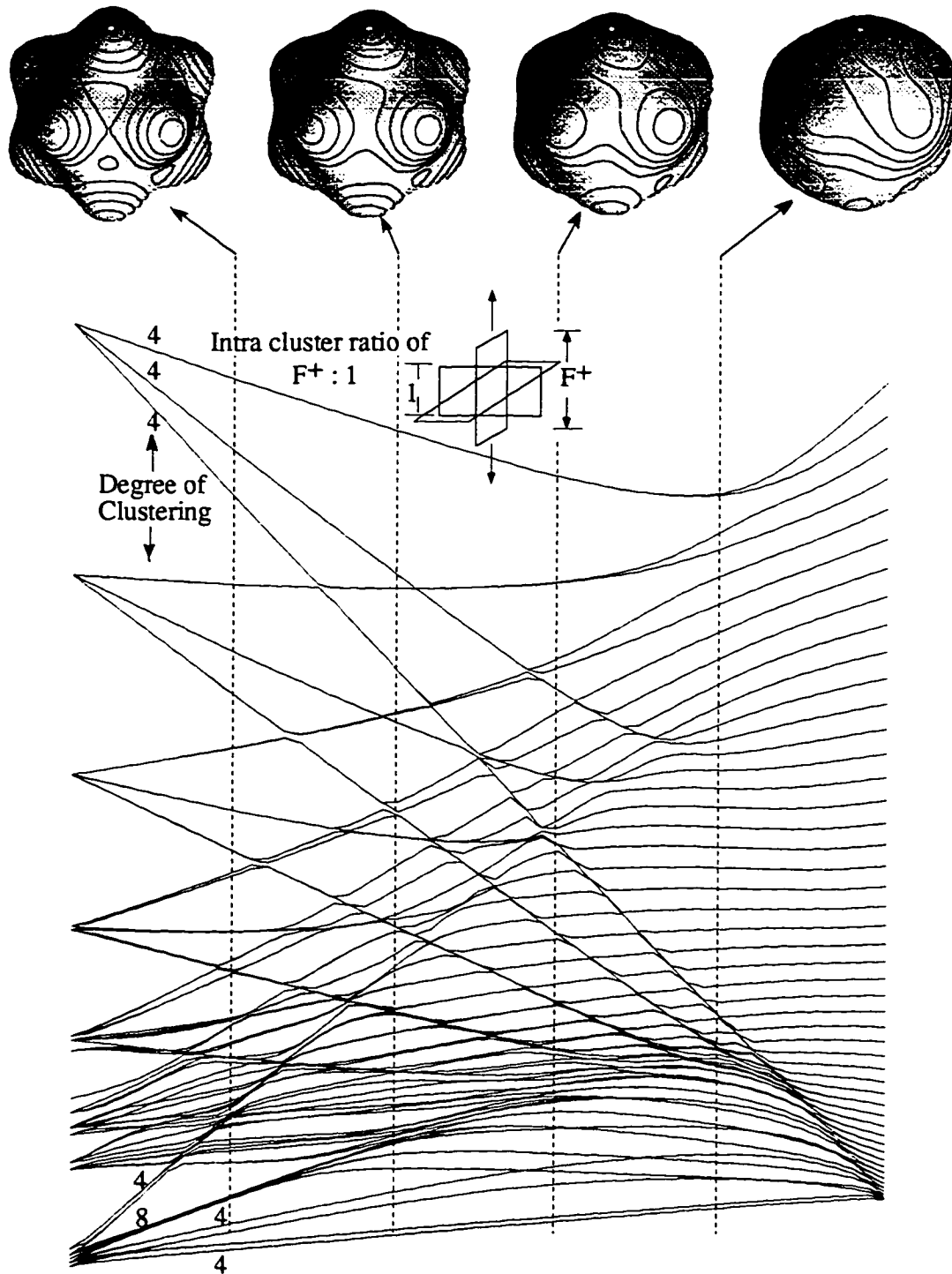


Figure 7.5 (a) Rotational energy surfaces for $\tau = 1/5, \dots, 4/5$. (b) Quantum mechanical energy levels for $|J|=50$. Both vary from pure semi-rigid icosahedral (left) to pure symmetric top centered at C_2 axes (right)

The $\tau=0$ clusters all break up into 4-fold subclusters as τ becomes non-zero. Again these 4-fold subclusters contain only rotational singlets until τ goes to 1. The two 4-fold valleys situated near the waist of the RE surfaces are affected the least by the symmetric top perturbation and corresponding subclusters remain close to each other for small values of τ . Another interesting feature is the separation of the subclusters originating from the same 12-fold cluster. Since the symmetric top perturbation is aligned with the golden rectangles mentioned in chapter 1 the splittings would be expected to follow the golden mean. This is indeed the case for a great deal of the smaller τ values, and this could be an important feature in the description of rotational spectra of molecules having C_2 type doping.

Chapter 8 Conclusions

Rotational level fine structure of the recently discovered C_{60} Buckyball has been investigated. The theory has been aimed at the prediction and understanding of the finer features that would be present in high resolution spectra of these cage molecules, ions (C_{60}^-) and derivatives formed by isotopic and elemental substitution ($^{13}C^{12}C_{59}$, NC_{59}). $^{13}C^{12}C_{59}$ could be the major contributor to fine structure in a high resolution infrared scan of C_{60} produced using naturally occurring carbon. The effects of Bose and Pauli exclusion on resultant spectra has been discussed and related to observed ultra-high resolution spectroscopy of SF_6 and SiF_4 .

Owing to the complexity of these Fullerenes and their related derivatives, advanced symmetry analysis, rotational energy surfaces, and computer graphics have been used to the study the effects of Coriolis coupling, rotational anisotropy, rotational axis tunneling, and nuclear spin-rotation interactions. The semi-classical rotational energy surface analysis was related to quantum mechanical energy levels in order to investigate classical-quantum correspondence and aid in visualization of the eigensolutions. These techniques were applied to the study of spontaneous and structural symmetry breaking.

Bibliography

Chapter 1

1. H.K. Kroto, J. R. Heath, S. C. O'brien, R. F. Curl, and R. E. Smalley, *Nature*, **318**, 162 (1985).
2. a) W.G. Harter and D.F. Weeks *Chem. Phys. Lett.*, **132**, 387 (1986).
b) D.F.,Weeks and W.G. Harter, *Chem. Phys. Lett.*, **144**, 366 (1988).
3. R.E. Stanton, M. D. Newton, *J. Phys. Chem.*, **92**, 2141 (1988).
4. J. Bordé and Ch. J. Bordé, *Chem. Phys.*, **71**, 417 (1982). b) W.G. Harter, E.W. Patterson, and F.J. daPaixao, *Revs. Mod. Phys.*, **50**, 37 (1978).
5. W. Kratschmer, K. Fostiropoulos, and D.R. Huffman, in Dusty Objects in the Universe, edited by E. Bussoletti and A.A. Vittone, Kluwer Dodrecht, (1990); C.I. Frum, R. Engleman Jr., H.G. Hedderich, P.F. Bernmath, L.D. Lamb and D.R. Huffman, *Chem. Phys. Lett.*, **170**, 167 (1990).
6. W. Kratschmer, L.D. Lamb, K. Fostiropoulos, and D.R. Huffman, *Nature*, **347**, 354 (1990).
7. D.S. Bethune, G. Meijer, W.C. Tang, and H.J. Rosen, *Chem. Phys. Lett.*, **174**, 219 (1990).
8. J.M. Hawkins, A. Meyer, T.A. Lewis, S.D. Loren, and F.J. Hollander, *Science*, **252**, 312 (1991).
9. S. Mayuma, L.R.Anderson and R.E. Smalley, *Rev. Sci.,Instrum.* **61**, 3686-3693 (1990).
10. S.Iijima, *Nature* **354**, 56-58 (1991).
11. P.A. Heiney et al., *Phys Rev Lett* **66** 2911(1991).
12. W.I.F. David et al.,*Nature* **353**, 147 (1991).
13. P.P. Schmidt, B. I. Dunlap, and C. T. White, *J. Phys. Chem.* **95**, 10 537 (1991).

14. L. Wang, M. J. Alford, Y. Chai, M. Diener, T. Guo, G. E. Scuseria and R. E. Smalley, *Chem. Phys. Lett.* (In press).
15. F. D Weiss, J. L. Elkind S. C. O'brien, R. F. Curl, and R. E. Smalley, *J. Am. Chem. Soc.* **110**, 3322 (1988).
16. R. E. Smalley, et. al. , *Science* **257**, 1661 (1992).
17. Y. Cai, L. T. Guo, C. Jin, R. E. Haufler, L. P. F. Chibante, J. Fure, L. Wang, M. J. Alford, and R. E. Smalley, *J. Phys. Chem.* **95**, 7568 (1991).
18. J. H. Weaver, Y. Chia, G. H. Kroll, C. Jin, T. R. Ohno, R. E. Haufler, T. Guo, J. M. Alford, J. Conceicao, A. Jain, G. Palmer, and R. E. Smalley, *Chem. Phys. Lett.* **190**, 460 (1992).
19. C. S. Yannonni, M. Hoinkls, M. S. de Vries, D. S. Bethune, J. R. Salem, M. S. Crowder, and R. D. Johnson, *Science* **256**, 1191 (1992).
20. R. D. Johnson, M. S. de Vries, D. S. Bethune, J. R. Salem, and C. S. Yannonni, *Nature* **355** 239 (1992).
21. C. Jin, T. Guo, Y. Chai, A. Lee, and R. E. Smalley, in *Proc. of the First Italian Workshop on Fullerenes: Status and Perspectives, Bologna, Italy, Feb. 6-7, 1992*, edited by C. Taliani, G. Ruani, R. Zamboni, (World Scientific, Singapore (1992), p. 21.
22. R.F. Curl and R.E. Smalley, *Scientific American* **265**, 54 (1990).
23. T. Guo, R. E. Smalley, and G. E. Scuseria, *J. Chem. Phys.*, **99** 1 (1993).
24. T. Guo, C. Jin, R.E. Smalley, *J. Phys. Chem*, **13** 4948 (1991).
25. T. Pradeep, V. Vijayakrishnan, A. K. Santra, and C.N. Rao, *J. Phys. Chem.*, **95** 10564 (1991).
26. W. Andreoni, F. Gygi, and M. Parrinello, *Chem. Phys. Lett.*, **190** 159 (1992).
27. B. C. Guo, K. P. Kerns, A. W. Castleman, *Science*, **255** 1411 (1992).
28. R. E. Smalley, et. al., *J. Phys. Chem.*, **94** 8634 (1990).

29. J. H. Holloway, E. G. Hope, R. Taylor, G. J. Langley, A. G. Avent, T. J. Dennis, J. P. Hare, H. W. Kroto, D. R. Walton, *J. Chem. Soc., Chem. Commun.* **966** (1991).
30. (a) J. M. Hawkins, A. Meyer, T. A. Lewis, S. Loren, F. J. Hollander, *Science*, **252** 312 (1991). (b) P. J. Fagen, J. C. Calabrese, B. Molone, *Science*, **252** 1160 (1991). (c) Y. Haung, and B. S. Freisser, *J. Am. Chem. Soc.*, **113** 8186 (1991). (d) L. M. Roth, Y. Huang, J. T. Schwedler, C. J. Cassady, D. Ben-Amotz, B. Kahr, B. S. Freiser, *J. Am. Chem. Soc.*, **113** 6298 (1991). (e) F. Chen, D. Singh, S. A. Jansen, *J. Phys. Chem.*, **97** (1993).
31. E. A. Rohlfing, D. M. Cox, and A. Kaldor, *J. Chem. Phys.*, **81**, 3322 (1984).
32. A. L. Balch, V. J. Catalano, J. W. Lee, M. M. Olmstead, and S. R. Parkin, *J. Am. Chem. Soc.*, **113**, 8953 (1991).
33. J.M. Hawkins, A Meyer, T.A. Lewis, S. Loren, F.J. Hollander, *Science*, **252** 312, 1991.
34. K. Tanigaki, I. Hirosawa, T. W. Ebbesen, J. Mizuki, Y. Shimakawa, Y. Kubo, J.S. Tsai, and S. Kuroshima, *Nature*, **356**, 419 (1992).
35. H. Kasatani, H. Terauchi, Y. Hamanaka, S. Nakashima, *Phys. Rev. B*, **47** 4022 (1993).
36. V. Blank, M. Popov, S. Buga, V. Davydov, V.N. Denison, A.N. Ivlev, B.N. Mavrin, V. Agafonov, R. Ceolin, H. Szwarc, A. Rassat, *Phys. Lett. A.*, **188**, 281 (1994).

Chapter 2

1. L. Saffaro, in *Proc. of the First Italian Workshop on Fullerenes: Status and Perspectives*, Bologna, Italy, Feb. 6-7, 1992, edited by C. Taliani, G. Ruani, R. Zamboni, (World Scientific, Singapore (1992), p. 55.

Chapter 3

1. Y. Deng, C.N. Yang, *Phys. Lett.A*, **170** 116, 1992.

2. P. Zhou, K. Wang, Y. Wang, P.C. Eklund, M.S. Dresselhaus, G. Dresselhaus, R.A. Jishi, *Phys. Rev. B*, **46**, 2595, 1992.
3. K.C. Kim, W.B. Person, D. Seitz, and B.J. Krohn, *J. Mol. Spectrosc.* **76**, 322 (1979).
4. D.E. Weeks and W.G. Harter, *Chem. Phys. Lett.*, **176**, 209 (1991).

Chapter 4

1. C.I. Frum, R. Engleman Jr., H.G. Hedderich, P.F. Bernmath, L.D. Lamb and D.R. Huffman, *Chem. Phys. Lett.*, **170**, 167 (1990).
2. O. Pfister, F. Guernet, G. Charton, Ch. Chardonnet, F. Herlemont and J. Legrand, *J. Opt. Soc. Am. B.*, **10** 1521, 1993.
3. W.G. Harter and D.E. Weeks, *Chem. Phys. Lett.*, **132**, 387 (1986).
4. W.G. Harter and D.E. Weeks, *J. Chem. Phys.*, **90**, 4727 (1989).
5. C.I. Frum, R. Engleman Jr., H.G. Hedderich, P.F. Bernmath, L.D. Lamb and D.F. Huffman, *Chem. Phys. Lett.*, **176**, 504 (1991).
6. D.E. Weeks and W.G. Harter, *Chem. Phys. Lett.*, **176**, 209 (1991).
7. D.E. Rutherford, *Substitutional Analysis*, (Edinburgh University, Edinburgh, 1947).
8. H. Weyl, *Theory of Groups and Quantum Mechanics* , (Dover, New York, 1931).
9. W.A. Goddard, *Phys. Rev.*, **157**, 73 (1967).
10. W.G. Harter, E.W. Patterson, and F.J. daPaixao, *Revs. Mod. Phys.*, **50**, 37 (1978).
11. a) W.G. Harter and C.W. Patterson, *Lecture Notes in Physics No. 49* (Springer Verlag, Berlin 1976); *Phys. Rev. A*, **13**, 1067 (1976).
b) W.G. Harter, *Phys. Rev. A*, **8**, 2819 (1973).

12. a) Ch. J. Borde, M. Ouhayouon, A. Vanlerberghe, C. Soloman, S. Avrillier, *Laser Spectroscopy IV*, edited by H. Walther and K.W. Rothe (Springer-Verlag, Berlin, 1975).
 b) J Borde, Ch. J. Borde, A. Vanlerberghe, C. Soloman, M. Ouhayouon and C.D. Cantrell, *Phys. Rev. Lett.*, **45**, 14 (1980).
13. a) O. Pfister, F. Guemet, G. Charton, Ch. Chardonnet, F. Herlemont and J. Legrand, *J. Opt. Soc. Am. B*, **10**, 1521 (1993).
 b) O. Pfister, *These: Etude experimentale et theorique des interactions hyperfines dans la bande de vibration ν_3 de la molecule $^{28}\text{SiF}_4$* . (University of North Paris, 1993).

Chapter 5

1. R.F. Curl and R.E. Smalley, *Science*, **242** 1139 (1988).
2. H. W. Kroto, *Nature*, **329**, No. 6139, 529 (1987).
3. L. A. Paquette, R. J. Ternasky, D. W. Balough, and G. Kentgas, *J. Am. Chem. Soc.*, **105**, 5446 (1983).
4. C. L. Beckel and James P. Vaughan, in *Boron-Rich Solids*, edited by D. Emin, T. Aselage, C.L. Beckel, I.A. Howard, and C. Wood (AIP Conf. Proc. No. 140) (AIP, New York, 1985); J.A. Wunderlich and W.N. Lipscomb, *J. Am. Chem. Soc.*, **82**,4427 (1960).
5. O. L. Chapman, and I. Amato, *Making Chicken Wire of Molecular Size*, *Science News*, **136** (1990).
6. H.W. Kroto, *Science*, **242**, 1139 (1988).
7. W.G. Harter, and D.E. Weeks, *Chem. Phys. Lett.*, **132**, 387 (1986).
8. W.G. Harter, and D.E. Weeks, *J. Chem. Phys.*, **90**, 4727 (1989).
9. W.G. Harter, *J. Math. Phys.* **10**, 739 (1969).
10. W.G. Harter and N. dos Santos, *Am. J. Phys.* **46**, 251 and 264 (1978).
11. A. Ceulemans and P. W. Fowler, *J. Chem. Phys.*, **93**, 1221 (1990).

12. K.C. Kim, W.B. Person, D. Seitz, and B.J. Krohn, *J. Mol. Spectrosc.* **76**, 322 (1979).
13. W.H. Press, B.P. Flannery, S.A. Teukolsky and W.T. Vetterling, *Numerical Recipes*, (Cambridge University Press, Cambridge, 1986).
14. L.C. Biedenharn and J.D. Louck, *Encyclopedia of Mathematics and its Applications*, **8. Angular Momentum in Quantum Physics**, ed. G. Rota (Addison Wesley, New York, 1981) p.46-55.

Chapter 6

1. W.G. Harter *Comp. Phys. Reports*, **8(6)** 321-394 (1988).

Chapter 7

1. C.C. Henderson, C.M. Rohlfing, P.A. Cahill, *Chem. Phys. Lett.*, **213** 383, 1993.
2. J. M. Hawkins, S. Loren, A. Meyer, and R. Nunlist, *J. Am. Chem. Soc.*, **113** 7770, 1991.
3. F. Chen, D. Singh, S.A. Jansen, *J. Phys. Chem.*, **97** 10958, 1993.

l	R ₁	R ₂	R ₃	R ₄	R ₅	R ₆	R ₁ ²	R ₂ ²	R ₃ ²	R ₄ ²	R ₅ ²	R ₆ ²	R ₁ ³	R ₂ ³	R ₃ ³	R ₄ ³	R ₅ ³	R ₆ ³	R ₁ ⁴	R ₂ ⁴	R ₃ ⁴	R ₄ ⁴	R ₅ ⁴	R ₆ ⁴	t ₁	t ₂	t ₃	t ₄	t ₅			
76	-R ₂ ²	-R ₁ ²	R ₁ ²	R ₂ ²	-R ₃ ²	7	12	R ₃ ²	11	-R ₁₀	16	-R ₂ ²	R ₂	-R ₂ ²	R ₆	113	R ₆ ²	R ₂ ²	7	16	R ₁₀	R ₂ ²	7	115	R ₁ ²	17	13	16	76			
77	-R ₂ ²	-R ₁ ²	-R ₂ ²	13	-R ₆	R ₂ ²	17	13	12	R ₂ ²	R ₂ ²	-76	R ₆ ²	-R ₆	R ₆	R ₂ ²	R ₂ ²	-115	17	16	16	16	112	-R ₆ ²	113	16	R ₂ ²	16	76			
78	16	-R ₂ ²	R ₆ ²	R ₂ ²	R ₂ ²	-76	R ₂ ²	16	13	-16	17	-R ₂ ²	R ₆ ²	-R ₆ ²	R ₁	R ₆	112	-R ₂ ²	116	-76	17	16	16	R ₁ ²	11	13	16	-115	-111	R ₆ ²		
79	-R ₂ ²	110	-R ₆ ²	R ₂ ²	-76	R ₆ ²	-76	16	-16	R ₂ ²	18	-116	R ₆ ²	-R ₂ ²	-R ₂ ²	R ₆	R ₂ ²	111	-76	-72	12	110	-72	-72	-72	11	16	11	-112	112		
100	17	-R ₂ ²	-R ₆ ²	16	R ₆ ²	R ₂ ²	R ₂ ²	-76	16	R ₂ ²	11	-11	R ₂ ²	-11	-R ₆	R ₂ ²	R ₁	R ₂ ²	13	-R ₂ ²	-76	113	16	16	12	17	16	-R ₆ ²	17			
101	-112	-76	-R ₁ ²	R ₁	-16	16	R ₆ ²	R ₂ ²	16	-111	-R ₆ ²	-76	-72	-R ₂ ²	-17	R ₂	-76	R ₂ ²	-R ₆	110	-R ₂ ²	-76	-76	-1	1	R ₃	110	11	-R ₂ ²			
102	-113	-R ₂ ²	-76	R ₆ ²	-R ₂ ²	R ₁	R ₆ ²	17	R ₂ ²	-112	16	-16	-72	110	-R ₂ ²	-76	-76	-R ₂ ²	-R ₂ ²	-R ₆	R ₂ ²	-76	-76	-76	-1	1	R ₃	16	16	-76		
103	-76	-116	-R ₂ ²	17	-76	R ₂ ²	R ₁	17	-R ₂ ²	R ₆ ²	-113	-113	-76	-76	-R ₂ ²	-R ₆	-R ₂ ²	-R ₆	-R ₂ ²	-R ₆	R ₂ ²	-76	-76	-76	-1	1	R ₃	-76	-76	-1	R ₁	
104	-R ₂ ²	115	16	R ₂ ²	-R ₂ ²	-76	-110	R ₆ ²	R ₂ ²	-76	-11	-11	-11	16	R ₂ ²	-16	-R ₃	R ₂ ²	R ₂ ²	16	-R ₂ ²	-76	10	-11	-76	-76	-76	-1	-76	-76	-1	R ₁
105	16	16	-R ₂ ²	111	-R ₆	11	R ₂ ²	R ₆ ²	-76	R ₂	115	R ₂ ²	R ₂ ²	16	-16	17	-R ₆	R ₁ ²	11	R ₂ ²	R ₂ ²	R ₁	-76	17	R ₂ ²	16	16	R ₁ ²	-1			
106	-76	-R ₂ ²	-76	17	-11	R ₂ ²	R ₃	110	R ₆	-R ₂ ²	R ₁	-76	-76	-113	-76	R ₂ ²	-110	-16	-R ₆	-R ₂ ²	-115	-R ₆ ²	-R ₂ ²	-76	R ₃	17	-76	16	-76	-1		
107	-12	-76	-13	R ₂ ²	-R ₂ ²	16	R ₂	R ₃	R ₁	-76	17	-R ₂ ²	-76	-76	-76	115	16	-R ₂ ²	R ₆ ²	-R ₆	R ₂ ²	-R ₂ ²	R ₂ ²	-112	17	-76	-R ₆	17	-76	-76		
108	-R ₂ ²	-76	-16	16	-76	R ₂ ²	-76	-R ₆	R ₂	-R ₃	R ₂ ²	-76	-11	-76	16	-76	-112	R ₂ ²	R ₁ ²	R ₆ ²	-R ₆	116	R ₁ ²	-115	-111	-76	-76	-76	-76	R ₆		
109	110	-R ₂ ²	16	-16	-R ₂ ²	19	R ₂ ²	12	R ₆	-76	R ₃	-76	-111	-R ₂ ²	-76	13	17	-76	-R ₂ ²	-113	-R ₁ ²	R ₂ ²	R ₇	R ₆ ²	17	16	-16	-76	116			
111	-R ₂ ²	-76	-76	12	-110	R ₂ ²	R ₂ ²	16	110	-11	16	-R ₂ ²	17	-112	-R ₁ ²	17	R ₆ ²	16	16	-76	-R ₆	116	R ₁	15	17	13	16	-76	-76	R ₆ ²		
112	-76	-R ₂ ²	-76	17	-R ₂ ²	13	17	R ₂ ²	16	-11	R ₁ ²	-76	-R ₆ ²	-76	-R ₂ ²	116	16	16	R ₂	-76	R ₆	-11	17	113	17	17	R ₂ ²	16	16	-76	-76	
113	-R ₂ ²	-76	-76	R ₂ ²	-16	16	R ₂ ²	16	17	-R ₂ ²	17	-13	-110	-R ₆ ²	R ₆ ²	16	-111	17	-R ₆	R ₁	-110	113	16	114	-115	-76	-R ₂ ²	17	16	-76	-76	
114	-76	-R ₂ ²	16	16	16	-R ₂ ²	16	R ₂ ²	16	-76	-76	-R ₂ ²	-115	-76	-R ₂ ²	17	17	-R ₆ ²	16	-112	-R ₆	-112	-R ₆	13	16	16	-R ₂ ²	-76	-111	-112	12	
115	-11	-11	-110	R ₂ ²	R ₂ ²	-76	16	-76	-76	-R ₂ ²	R ₂ ²	-110	-115	-76	-R ₂ ²	17	17	-R ₆ ²	16	-112	-R ₆	13	17	17	-R ₆	13	16	-R ₂ ²	-76	-111	-112	12
116	-76	-11	-110	R ₂ ²	R ₂ ²	-76	16	-76	-76	-R ₂ ²	R ₂ ²	-110	-115	-76	-R ₂ ²	17	17	-R ₆ ²	16	-112	-R ₆	13	17	17	-R ₆	13	16	-R ₂ ²	-76	-111	-112	12
117	-76	-76	-R ₂ ²	116	-76	R ₂ ²	17	17	112	-R ₁ ²	-R ₁ ²	-R ₁ ²	-R ₁ ²	-R ₆	16	-11	-76	17	R ₆ ²	R ₃	17	-11	16	-76	R ₂ ²	17	R ₂	17	-76	-R ₂ ²		
118	-16	-76	R ₂ ²	-76	R ₂ ²	-111	-115	-76	-76	-11	-R ₂ ²	-76	-11	-R ₂ ²	17	-76	-11	-R ₂ ²	17	-76	-11	-R ₂ ²	17	-76	-11	-76	-R ₂ ²	-76	-11	-76	-76	
119	-115	-R ₂ ²	-R ₂ ²	112	17	-11	16	R ₂ ²	R ₂ ²	115	-76	16	-76	-76	-113	R ₁	-R ₁ ²	12	110	110	-114	R ₂	-R ₂ ²	13	R ₃	16	11	16	-76	-76	-76	
120	-76	-76	-113	17	17	-R ₁ ²	17	16	111	-76	R ₂ ²	-R ₂ ²	R ₆	16	-114	R ₆ ²	-76	17	R ₃	11	115	-R ₂ ²	-76	16	R ₂ ²	R ₁	16	12	12	-76		
121	-76	-R ₂ ²	-114	R ₆ ²	-76	17	17	17	112	-R ₁ ²	16	-13	-R ₂ ²	110	-115	-110	-76	R ₂	R ₆ ²	17	111	-76	-76	-76	16	R ₆ ²	R ₁	17	-76	-76		
122	-R ₂ ²	-76	115	-11	-R ₂ ²	17	R ₆ ²	17	113	-76	-76	-76	-76	R ₆	111	-11	-76	-R ₂ ²	16	R ₁	112	-76	17	-R ₁ ²	-76	-110	R ₆ ²	R ₂	-76	-76		
123	16	-76	-111	-R ₂ ²	-76	R ₂ ²	110	-76	-114	R ₂ ²	-76	16	-R ₆ ²	-112	16	16	-R ₆ ²	-113	17	R ₆	17	110	11	110	11	110	R ₆ ²	R ₂	-76	-76		

	r_6	r_7	r_8	r_9	r_{10}	r_{11}	r_{12}	r_{13}	r_{14}	r_{15}	r_{16}	r_{17}	r_{18}	r_{19}	r_{20}	r_{21}	r_{22}	r_{23}	r_{24}	r_{25}	r_{26}	r_{27}	r_{28}	r_{29}	r_{30}	r_{31}	r_{32}	r_{33}	r_{34}	r_{35}	r_{36}	r_{37}	r_{38}	r_{39}	r_{40}
r_6	r_6^2	r_7^2	r_8^2	r_9^2	r_{10}^2	r_{11}^2	r_{12}^2	r_{13}^2	r_{14}^2	r_{15}^2	r_{16}^2	r_{17}^2	r_{18}^2	r_{19}^2	r_{20}^2	r_6	r_7	r_8	r_9	r_{10}	r_{11}	r_{12}	r_{13}	r_{14}	r_{15}	r_{16}	r_{17}	r_{18}	r_{19}	r_{20}					
r_7	$r_6 r_7$	r_7^2	r_8^2	r_9^2	r_{10}^2	r_{11}^2	r_{12}^2	r_{13}^2	r_{14}^2	r_{15}^2	r_{16}^2	r_{17}^2	r_{18}^2	r_{19}^2	r_{20}^2	r_7	r_8	r_9	r_{10}	r_{11}	r_{12}	r_{13}	r_{14}	r_{15}	r_{16}	r_{17}	r_{18}	r_{19}	r_{20}						
r_8	$r_6 r_8$	$r_7 r_8$	r_8^2	r_9^2	r_{10}^2	r_{11}^2	r_{12}^2	r_{13}^2	r_{14}^2	r_{15}^2	r_{16}^2	r_{17}^2	r_{18}^2	r_{19}^2	r_{20}^2	r_8	r_9	r_{10}	r_{11}	r_{12}	r_{13}	r_{14}	r_{15}	r_{16}	r_{17}	r_{18}	r_{19}	r_{20}							
r_9	$r_6 r_9$	$r_7 r_9$	$r_8 r_9$	r_9^2	r_{10}^2	r_{11}^2	r_{12}^2	r_{13}^2	r_{14}^2	r_{15}^2	r_{16}^2	r_{17}^2	r_{18}^2	r_{19}^2	r_{20}^2	r_9	r_{10}	r_{11}	r_{12}	r_{13}	r_{14}	r_{15}	r_{16}	r_{17}	r_{18}	r_{19}	r_{20}								
r_{10}	$r_6 r_{10}$	$r_7 r_{10}$	$r_8 r_{10}$	$r_9 r_{10}$	r_{10}^2	r_{11}^2	r_{12}^2	r_{13}^2	r_{14}^2	r_{15}^2	r_{16}^2	r_{17}^2	r_{18}^2	r_{19}^2	r_{20}^2	r_{10}	r_{11}	r_{12}	r_{13}	r_{14}	r_{15}	r_{16}	r_{17}	r_{18}	r_{19}	r_{20}									
r_{11}	$r_6 r_{11}$	$r_7 r_{11}$	$r_8 r_{11}$	$r_9 r_{11}$	$r_{10} r_{11}$	r_{11}^2	r_{12}^2	r_{13}^2	r_{14}^2	r_{15}^2	r_{16}^2	r_{17}^2	r_{18}^2	r_{19}^2	r_{20}^2	r_{11}	r_{12}	r_{13}	r_{14}	r_{15}	r_{16}	r_{17}	r_{18}	r_{19}	r_{20}										
r_{12}	$r_6 r_{12}$	$r_7 r_{12}$	$r_8 r_{12}$	$r_9 r_{12}$	$r_{10} r_{12}$	$r_{11} r_{12}$	r_{12}^2	r_{13}^2	r_{14}^2	r_{15}^2	r_{16}^2	r_{17}^2	r_{18}^2	r_{19}^2	r_{20}^2	r_{12}	r_{13}	r_{14}	r_{15}	r_{16}	r_{17}	r_{18}	r_{19}	r_{20}											
r_{13}	$r_6 r_{13}$	$r_7 r_{13}$	$r_8 r_{13}$	$r_9 r_{13}$	$r_{10} r_{13}$	$r_{11} r_{13}$	$r_{12} r_{13}$	r_{13}^2	r_{14}^2	r_{15}^2	r_{16}^2	r_{17}^2	r_{18}^2	r_{19}^2	r_{20}^2	r_{13}	r_{14}	r_{15}	r_{16}	r_{17}	r_{18}	r_{19}	r_{20}												
r_{14}	$r_6 r_{14}$	$r_7 r_{14}$	$r_8 r_{14}$	$r_9 r_{14}$	$r_{10} r_{14}$	$r_{11} r_{14}$	$r_{12} r_{14}$	$r_{13} r_{14}$	r_{14}^2	r_{15}^2	r_{16}^2	r_{17}^2	r_{18}^2	r_{19}^2	r_{20}^2	r_{14}	r_{15}	r_{16}	r_{17}	r_{18}	r_{19}	r_{20}													
r_{15}	$r_6 r_{15}$	$r_7 r_{15}$	$r_8 r_{15}$	$r_9 r_{15}$	$r_{10} r_{15}$	$r_{11} r_{15}$	$r_{12} r_{15}$	$r_{13} r_{15}$	$r_{14} r_{15}$	r_{15}^2	r_{16}^2	r_{17}^2	r_{18}^2	r_{19}^2	r_{20}^2	r_{15}	r_{16}	r_{17}	r_{18}	r_{19}	r_{20}														
r_{16}	$r_6 r_{16}$	$r_7 r_{16}$	$r_8 r_{16}$	$r_9 r_{16}$	$r_{10} r_{16}$	$r_{11} r_{16}$	$r_{12} r_{16}$	$r_{13} r_{16}$	$r_{14} r_{16}$	$r_{15} r_{16}$	r_{16}^2	r_{17}^2	r_{18}^2	r_{19}^2	r_{20}^2	r_{16}	r_{17}	r_{18}	r_{19}	r_{20}															
r_{17}	$r_6 r_{17}$	$r_7 r_{17}$	$r_8 r_{17}$	$r_9 r_{17}$	$r_{10} r_{17}$	$r_{11} r_{17}$	$r_{12} r_{17}$	$r_{13} r_{17}$	$r_{14} r_{17}$	$r_{15} r_{17}$	$r_{16} r_{17}$	r_{17}^2	r_{18}^2	r_{19}^2	r_{20}^2	r_{17}	r_{18}	r_{19}	r_{20}																
r_{18}	$r_6 r_{18}$	$r_7 r_{18}$	$r_8 r_{18}$	$r_9 r_{18}$	$r_{10} r_{18}$	$r_{11} r_{18}$	$r_{12} r_{18}$	$r_{13} r_{18}$	$r_{14} r_{18}$	$r_{15} r_{18}$	$r_{16} r_{18}$	$r_{17} r_{18}$	r_{18}^2	r_{19}^2	r_{20}^2	r_{18}	r_{19}	r_{20}																	
r_{19}	$r_6 r_{19}$	$r_7 r_{19}$	$r_8 r_{19}$	$r_9 r_{19}$	$r_{10} r_{19}$	$r_{11} r_{19}$	$r_{12} r_{19}$	$r_{13} r_{19}$	$r_{14} r_{19}$	$r_{15} r_{19}$	$r_{16} r_{19}$	$r_{17} r_{19}$	$r_{18} r_{19}$	r_{19}^2	r_{20}^2	r_{19}	r_{20}																		
r_{20}	$r_6 r_{20}$	$r_7 r_{20}$	$r_8 r_{20}$	$r_9 r_{20}$	$r_{10} r_{20}$	$r_{11} r_{20}$	$r_{12} r_{20}$	$r_{13} r_{20}$	$r_{14} r_{20}$	$r_{15} r_{20}$	$r_{16} r_{20}$	$r_{17} r_{20}$	$r_{18} r_{20}$	$r_{19} r_{20}$	r_{20}^2	r_{20}																			

Appendix B Irreducible Representations, Characters, and Correlations

To begin the analysis one must be able to produce the irreducible representations of each rotation operator for every icosahedral symmetry species α . One way to determine these irreps is by subduction from the SU(2) supergroup (or algebra). The standard formula for these irreps in any J total angular momentum basis given the Euler angles (α, β, γ) of the rotational operator.

$$D_{mn}^j(\mathbf{R}(\alpha, \beta, \gamma)) = \sum_k (-1)^k \frac{\sqrt{(j+m)! (j-m)! (j+n)! (j-n)!}}{(j+m-k)! k! (j-n-k)! (j-n+k)!} e^{-i(m\alpha+n\gamma)} \times (\cos(\beta/2))^{2j+m-n-2k} (\sin(\beta/2))^{n-m+2k} \quad (\text{B.1})$$

The SU(2) representation is irreducible and unitary.

$$D_{mn}^j(\mathbf{R}^{-1}(\alpha, \beta, \gamma)) = D_{nm}^{j*}(\mathbf{R}(\alpha, \beta, \gamma)) \quad (\text{B.2})$$

The frequency of occurrences of an icosahedral symmetry species α , arising via subduction from the J representation, can be found using standard character analysis.

$$f^\alpha = \frac{1}{|G|} \sum_{C_g} \chi_g^{\alpha*} \circ C_g \text{Trace}(D_{mn}^j(g)) \quad (\text{B.3})$$

Here the irreducible characters are,

$$\chi_g^\alpha = \text{Trace}(D_{mn}^\alpha(g))$$

and g is a representative of each commutation class, and *C_g is the number of operators in that class. The $SU(2)$ characters for the icosahedral classes depend only on their angle (ω) of rotation for each class element and upon the total angular momentum j .

$$\chi_{C_g}^\alpha = \text{Trace}\left(D_{mn}^j(R(0,0,\omega))\right) = \frac{\sin((j+1/2)\omega)}{\sin(\omega/2)} \quad (\text{B.4})$$

The correlations found using Eqs.(B.3),(B.4) are presented in Table 5.4. One notices, that the $SU(2)$ characters for $j=1/2,3/2$, and $5/2$ correlate with the icosahedral characters $E_{1/2},G$, and I respectively. This also implies that the representations also map in a similar manner. The remaining doubly degenerate $E_{7/2}$ is seen to correlate with the $D^{7/2}$ irrep only when taken as a direct sum with the I species, and therefore must be determined by a different method.

This method involves finding the corresponding $E_{7/2}$ projection operators ($P^{E_{7/2}_i}$), and using the relation,

$$P_i^\alpha P_j^\beta = D_{ij}^\alpha(g) P_{ij}^\alpha \delta_{\alpha\beta} \quad (\text{B.5})$$

One starts by choosing an Abelian subgroup, for example C_5 , and a proper chain of subgroups connecting it with Y , $Y \subset D_5 \subset C_5$ for example. The complete set of all-commuting projection operators is found for each group in the chain using,

$$P^\alpha = \frac{1}{|G|} \sum_{C_g} \chi_{C_g}^{\alpha*} C_g \quad (\text{B.6})$$

with C_g being the sum of elements in the class that contains g . Since the P^α are complete in each group algebra, we have the following relation.

$$\sum_{\alpha} P^{\alpha} = 1 \quad (\text{B.7})$$

If α denotes the icosahedral species, δ denotes the D_5 species, and σ the C_5 labels, then the non-zero terms in the product,

$$\left(\sum_{\alpha} P^{\alpha} \right) \left(\sum_{\delta} P^{\delta} \right) \left(\sum_{\sigma} P^{\sigma} \right) = 1 \quad (\text{B.8})$$

give the idempotent projection operators in Eq.(B.5). Two of these will be the $E_{7/2}$ projectors, which will be labeled as $P_1^{E_{7/2}}$ and $P_2^{E_{7/2}}$. The method used earlier (equations (B.3)) can be used to find correlation Tables 5.5. These results indicate the useful projection product in the expansion of (B.8) which deliver the $P^{E_{7/2}}$ idempotents. From Table 5.5, the $E_{7/2}$ row correlates with the $A_{3 \bmod 10}$ and $A_{7 \bmod 10}$ C_5 symmetry species, which in turn correlate with the D_5 species E_2 ending with the $P^{E_{7/2}}$ icosahedral all-commuting projector. This leads to,

$$\begin{aligned} P_1^{E_{7/2}} &= P^{E_{7/2}} P^{E_2} P^{A_{3 \bmod 10}} \\ P_2^{E_{7/2}} &= P^{E_{7/2}} P^{E_2} P^{A_{7 \bmod 10}} \end{aligned} \quad (\text{B.9})$$

Products of the normalized projection operators in (B.9) (Normalized operators are denoted with a hat.) give the idempotents and nilpotents,

$$\hat{P}_i^{E_{7/2}} \hat{P}_j^{E_{7/2}} = \hat{P}_{ij}^{E_{7/2}} \quad (\text{B.10})$$

The representation matrix is determined by,

$$\langle \hat{P}_{ij}^\alpha | g | \hat{P}_{kl}^\beta \rangle = D_{ik}^\alpha \delta^{\alpha\beta} \delta_{jl} \quad (\text{B.11})$$

From equation B.11 it follows that,

$$g | \hat{P}_{kl}^\alpha \rangle = \sum_i D_{ik}^\alpha | \hat{P}_{il}^\alpha \rangle \quad (\text{B.12})$$

and one need only to make the appropriate choice for indices to determine the components of $D^\alpha(g)$. For example, to determine the $D_{12}^{7/2}(g)$ component, set $k=2$ and $l=1$ to arrive at,

$$g | \hat{P}_{21}^{7/2} \rangle = D_{12}^{7/2}(g) | \hat{P}_{11}^{7/2} \rangle + D_{22}^{7/2}(g) | \hat{P}_{21}^{7/2} \rangle \quad (\text{B.13})$$

The desired matrix component is found to be,

$$\langle \hat{P}_{11}^{7/2} | g | \hat{P}_{21}^{7/2} \rangle = D_{12}^{7/2}(g) \quad (\text{B.14})$$

Notice that the action of g as an operator mixes only those projected states that share the same local symmetry, which is denoted by the second subindex.

Coupling Bose-Y species.

Y	A	T ₁	T ₃	G	H
A ⊗ A	1+
A ⊗ T ₁	.	1+	.	.	.
A ⊗ T ₃	.	.	1+	.	.
A ⊗ G	.	.	.	1+	.
A ⊗ H	1+
T ₁ ⊗ T ₁	1+	1-	.	.	1+
T ₁ ⊗ T ₃	.	.	.	1+	1+
T ₁ ⊗ G	.	.	1+	1-	1+
T ₁ ⊗ H	.	1+	1+	1+	1-
T ₃ ⊗ T ₃	1+	.	1-	.	1+
T ₃ ⊗ G	.	1-	.	1+	1+
T ₃ ⊗ H	.	1+	1+	1+	1+
G ⊗ G	1+	1-	1-	1+	1+
G ⊗ H	.	1+	1-	1+	2++
H ⊗ H	1+	1-	1-	2+-	2++

Coupling Bose-Fermi Y species.

	E _{1/2}	E _{7/2}	G	I
A ⊗ E _{1/2}	1	.	.	.
A ⊗ E _{7/2}	.	1	.	.
A ⊗ G ^h	.	.	1	.
A ⊗ I	.	.	.	1
T ₁ ⊗ E _{1/2}	.	1	1	.
T ₁ ⊗ E _{7/2}	.	.	.	1
T ₁ ⊗ G ^h	1	.	1	1
T ₁ ⊗ I	.	1	1	2
T ₃ ⊗ E _{1/2}	.	.	.	1
T ₃ ⊗ E _{7/2}	.	1	1	.
T ₃ ⊗ G ^h	.	1	1	1
T ₃ ⊗ I	1	.	1	2
G ⁱ ⊗ E _{1/2}	.	1	.	1
G ⁱ ⊗ E _{7/2}	1	.	.	1
G ⁱ ⊗ G ^h	.	.	1	2
G ⁱ ⊗ I	1	1	2	2
H ⊗ E _{1/2}	.	.	1	1
H ⊗ E _{7/2}	.	.	1	1
H ⊗ G ^h	1	1	1	2
H ⊗ I	1	1	2	3

Coupling Fermi-Fermi Y species.

Y ^(d)	A	T ₁	T ₃	G	H
E _{1/2} ⊗ E _{1/2}	1-	1+	.	.	.
E _{1/2} ⊗ E _{7/2}	.	.	.	1	.
E _{1/2} ⊗ G	.	1	.	.	1
E _{1/2} ⊗ I	.	.	1	1	1
E _{7/2} ⊗ E _{7/2}	1	.	1	.	.
E _{7/2} ⊗ G	.	.	1	.	1
E _{7/2} ⊗ I	.	1	.	1	1
G ⊗ G	1-	1+	1+	1+	1-
G ⊗ I	.	1	1	2	2
I ⊗ I	1-	2+	2+	2+-	3+--

Appendix D S₆₀ characters for icosahedral operators

$[\mu_1, \mu_2]$ $\chi_{\alpha_1, \alpha_2}$	Γ, Γ {160}, {230}	R, IR {5 ¹² }, {10 ⁶ }	R^2, IR^2 {5 ¹² }, {10 ⁶ }	r, Ir {320}, {6 ¹⁰ }	i, Ii {230}, {14, 228}
[60, 0]	1 1	1 1	1 1	1 1	1 1
[59, 1]	59 -1	-1 -1	-1 -1	-1 -1	-1 3
[58, 2]	1710 30	0 0	0 0	0 0	30 30
[57, 3]	32450 -30	0 0	0 0	20 0	-30 82
[56, 4]	453415 435	0 0	0 0	-20 0	435 431
[55, 5]	4973877 -435	12 0	12 0	0 0	-435 1077
[54, 6]	44602348 4060	-12 0	-12 0	190 10	4060 3948
[53, 7]	336143060 -4060	0 0	0 0	-190 -10	-4060 9044
[52, 8]	2172413925 27405	0 0	0 0	0 0	27405 25893
[51, 9]	12224521815 -27405	0 0	0 0	1140 0	-27405 54495
[50, 10]	60610884906 142506	66 6	66 6	-1140 0	142506 129402
[49, 11]	267306097734 -142506	-66 -6	-66 -6	0 0	-142506 250614

{48,12}	1056658719675 593775	0 0	0 0	0 0	4845 45	593775 511875
{47,13}	3767504582625 -593775	0 0	0 0	0 0	-4845 -45	-593775 913185
{46,14}	12179035222200 2035800	0 0	0 0	0 0	0 0	2035800 1642680
{45,15}	35848190542920 -2035800	220 0	220 0	220 0	15504 0	-2035800 2700360
{44,16}	96414286661805 5852925	-220 0	-220 0	-220 0	-15504 0	5852925 4345965
{43,17}	237613302827775 -5852925	0 0	0 0	0 0	0 0	-5852925 6579495
{42,18}	537807887058750 14307150	0 0	0 0	0 0	38760 120	14307150 9570990
{41,19}	111972632212850 -14307150	0 0	0 0	0 0	-38760 -120	-14307150 13320450
{40,20}	2147042307851595 30045015	495 15	495 15	495 15	0 0	30045015 17612595
{39,21}	3792621219538305 -30045015	-495 -15	-495 -15	-495 -15	77520 0	-30045015 22447425
{38,22}	6169814424129300 54627300	0 0	0 0	0 0	-77520 0	54627300 26999700
{37,23}	9231052271395500 -54627300	0 0	0 0	0 0	0 0	-54627300 31269420
{36,24}	12667055061303825 86493225	0 0	0 0	0 0	125970 210	86493225 34000785
{35,25}	15863050492155867 -86493225	792 0	792 0	792 0	-125970 -210	-86493225 35193795

111

{34,26}	17970728529575178	-792	-792	0	0	119759850
	119759850	0	0	0	0	33863130
{33,27}	18118635760271270	0	0	167960	167960	-119759850
	-119759850	0	0	0	0	30008790
{32,28}	15715143261459775	0	0	-167960	-167960	145422675
	145422675	0	0	0	0	23735655
{31,29}	10729649537134605	0	0	0	0	-145422675
	-145422675	0	0	0	0	15043725
{30,30}	3814986502092304	924	924	184756	184756	155117520
	155117520	20	20	252	252	5348880

112

Appendix E. Y_H-S₆₀ correlation frequencies

I Par	Ag/Au	T1g/T1u	T3g/T3u	Gg/Gu	Hg/Hu
30 g	1	0	0	0	0
u	0	0	0	0	0
29 g	0	1	1	2	3
u	0	2	2	2	2
28 g	22	36	36	58	80
u	14	42	42	56	70
27 g	280	804	804	1084	1354
u	260	826	826	1086	1336
26 g	3887	11238	11238	15125	19022
u	3772	11324	11324	15096	18878
25 g	41528	124257	124257	165779	207307
u	41266	124548	124548	165808	207074

24	g	372752	1114158	1114158	1114158	1486916	1859568
	u	371694	1114942	1114942	1114942	1486642	1858246
23	g	2801748	8402852	8402852	8402852	11204600	14006448
	u	2799558	8405316	8405316	8405316	11204874	14004522
22	g	18110340	54304371	54304371	54304371	72414711	90525051
	u	18103410	54309474	54309474	54309474	72412864	90516294
21	g	101874363	305608974	305608974	305608974	407483337	509357130
	u	101861196	305623968	305623968	305623968	407485164	509345790
20	g	505125708	1515241704	1515241704	1515241704	2020367376	2525493654
	u	505090980	1515266928	1515266928	1515266928	2020357878	2525449428
19	g	2227563126	6682635360	6682635360	6682635360	8910198522	11137761648
	u	2227502850	6682705140	6682705140	6682705140	8910208020	11137710870
18	g	8805633300	26416344630	26416344630	26416344630	35221977930	44027608785
	u	8805495420	26416442910	26416442910	26416442910	35221938330	44027431350
17	g	31395905685	94187559795	94187559795	94187559795	125583465480	156979373610
	u	31395687300	94187817780	94187817780	94187817780	125583505080	156979194780
16	g	101492436960	304475471640	304475471640	304475471640	405967908600	507460345560
	u	101491992360	304475780520	304475780520	304475780520	405967772880	507459765240
15	g	298734989924	896204629630	896204629630	896204629630	1194939619444	1493674601616
	u	298734348764	896205406510	896205406510	896205406510	1194939755164	1493674096176
14	g	803453709856	2410356037985	2410356037985	2410356037985	3213809747951	4017263465559
	u	803452525816	2410356831830	2410356831830	2410356831830	3213809357756	4017261891324
13	g	1980110898945	5940332333550	5940332333550	5940332333550	7920443232495	9900554131440
	u	1980109351620	5940334271070	5940334271070	5940334271070	7920443622690	9900552974310
12	g	4481735502630	13445194549380	13445194549380	13445194549380	17926930052010	22408665535200
	u	4481732871390	13445196226770	13445196226770	13445196226770	17926929098160	22408661950230

11	g	9331438352730	27994315570980	27994315570980	27994315570980	37325753923710	46657192295880
	u	9331435261110	27994319616450	27994319616450	27994319616450	37325754877560	46657190157990
10	g	17892025439775	53676052490265	53676052490265	53676052490265	71568077929785	89460103369560
	u	17892020535870	53676055391160	53676055391160	53676055391160	71568075926790	89460096462660
9	g	31605175642230	94815530686980	94815530686980	94815530686980	126420706329465	158025881932935
	u	31605170531130	94815537801090	94815537801090	94815537801090	126420708332460	158025878824830
8	g	51415130846760	154245351765540	154245351765540	154245351765540	205660482612300	257075613497820
	u	51415123186380	154245355784100	154245355784100	154245355784100	205660478970480	257075602195620
7	g	76925432220000	230776308338940	230776308338940	230776308338940	307701740558940	384627172778940
	u	76925425313100	230776318887660	230776318887660	230776318887660	307701744200760	384627169513860
6	g	105558807981090	316676363633175	316676363633175	316676363633175	422235171614265	527793979532265
	u	105558798039270	316676367808710	316676367808710	316676367808710	422235165847980	527793963824370
5	g	132192080280555	396576266554074	396576266554074	396576266554074	528768346834233	660960427177878
	u	132192072923730	396576279677184	396576279677184	396576279677184	528768352600518	6609604255587128
4	g	149756091280506	449268197030424	449268197030424	449268197030424	599024288311326	748780379591832
	u	149756080818726	449268199508214	449268199508214	449268199508214	599024280327336	748780361146062
3	g	150988619146706	452965902231668	452965902231668	452965902231668	603954521378374	754943140441100
	u	150988613640506	452965915721858	452965915721858	452965915721858	603954529362364	754943142918890
2	g	130959549507485	392878564027270	392878564027270	392878564027270	523838113534755	654797663126220
	u	130959541149860	392878562690050	392878562690050	392878562690050	523838103839910	654797645073750
1	g	89413728633564	268241251090167	268241251090167	268241251090167	357654979723731	447068708357295
	u	89413727296344	268241262122232	268241262122232	268241262122232	357654989418576	447068716714920
0	g	31791575566072	95374646372040	95374646372040	95374646372040	127166221937640	158957797411208
	u	31791571643468	95374639953380	95374639953380	95374639953380	127166211596396	158957783147612

